DEPOSITION AND ASSEMBLY OF MAGNESIUM HYDROXIDE NANOSTRUCTURES ON ZEOLITE 4A SURFACES

A Dissertation
Presented to
The Academic Faculty

by

Pei Yoong Koh

In Partial Fulfillment
of the Requirements for the Degree
Doctor of Philosophy in the
School of Chemical & Biomolecular Engineering

Georgia Institute of Technology
December 2010

COPYRIGHT ©2010 BY PEI YOONG KOH

DEPOSITION AND ASSEMBLY OF MAGNESIUM HYDROXIDE NANOSTRUCTURES ON ZEOLITE 4A SURFACES

Approved by:

Dr. Amyn S. Teja, Advisor
School of Chemical & Biomolecular Engineering
Georgia Institute of Technology

Dr. Sankar Nair
School of Chemical & Biomolecular Engineering
Georgia Institute of Technology

Dr. Yulin Deng
School of Chemical & Biomolecular Engineering
Georgia Institute of Technology

Dr. Rina Tannenbaum
School of Materials Science & Engineering
Georgia Institute of Technology

Dr. William J. Koros
School of Chemical & Biomolecular Engineering
Georgia Institute of Technology

Date Approved: November 11, 2010

To my family

ACKNOWLEDGEMENTS

I would first like to express my sincerest appreciation to my research advisor, Dr Amyn Teja. He has provided unwavering support and constant guidance throughout my entire graduate career at Georgia Tech, and I am much grateful for his mentorship. I could not hope for a better academic advisor than Professor Amyn Teja. Not only does he try to push me to think beyond my boundary, he has also encouraged me to explore my interest outside the lab. I still remember vividly the things he said when I asked him about my minor. His response was graduate school is a place for you to grow and develop your skills (research is still the most important, of course) and I should just explore my interest. I truly appreciate his advice and consider myself particularly fortunate to have been working under his tutelage. He is not merely a supervisor, but also a wonderful teacher and mentor.

I am thankful to all four members of my thesis committee who have taken time to read and evaluate this thesis and my defense. Professor Yulin Deng, Professor Sankar Nair, and Professor Rina Tannenbaum have been on my committee since my proposal. Professor Bill Koros joined the committee prior to my 4th year review. I am much grateful for his courtesy and for use of his equipment.

The whole of Dr Teja group has been a pleasure to work with, and the friendships forged will remain with me for life. I would like to thank all of the past and present members of the group for their support. In particular, I am grateful to my mentors Dr James Falabella and Dr Chunbao Xu for kick starting my research endeavor, Dr Michael Beck for his jolly attitude that made everyday work life a pleasurable one, and Dr

Anupama Kasturirangan for her friendship. I would also like to thank Yanhui Yuan and Pramod Warrier for their discussions and inputs to this work. I am also thankful to Nelson Green for his friendship, Firman Kurniawansyah and Jing Yan for their help in some of the experiments. Jing Yan has been a very diligent undergraduate assistant of mine.

I have made many wonderful friends at Georgia Tech and I will forever treasure these friendships. Special thanks go to Dr Apichit Svang-Ariyaskul, Dr Quinta Nwanosike-Warren, and Dr Jason Ward for their encouragement and for listening to my rants and putting up with my occasional tantrums. I also thank Dr Oguz Karvan and Bo Xu for their valuable assistance and meaningful discussions. The number of individuals who deserved to be acknowledged, are too numerous to list, so I will provide only a short list. I thank Hady Riyanto, Jimmy Ho, Benjamin Jonen, Romain Cledat, Prashant Kumar, Yanto Yanto, Hua-Wei Chu, Wei-Ming Yeh, Andres Hernandez Moreno, and Chien-Chiang Chen, for their friendship and help.

Finally, I have been very fortunate to have the unconditional love and support of my family throughout my graduate career. I am incredibly thankful to my parents, Moi Tee Koh and Hon Nge Kuam, for their financial support and constant faith in me. I would also like to thank all of my brothers Pek Hao Koh, Pei Jia Koh, and Pei Wee Koh for their love and encouragement.

TABLE OF CONTENTS

LIST OF TABLES

Page

LIST OF FIGURES

SUMMARY

A method was developed to precipitate and assemble magnesium hydroxide nanostructures on zeolite 4A surfaces at mild conditions. The effects of process variables such as precursor concentration, type of base added, and synthesis time on the composition, size, and morphology of the resulting $Mg(OH)_2$ / zeolite 4A nanocomposites were investigated. It was determined that the presence of a weak base such as ammonium hydroxide is essential to the control of the morphology of the magnesium hydroxide ($Mg(OH)_2$) nanostructures.

Properties of the $Mg(OH)_2$ / zeolite 4A nanocomposites such as surface area, pore volume and composition were characterized via BET and TGA. $Mg(OH)_2$ / zeolite 4A nanocomposites and bare zeolite 4A were dispersed in Ultem® polymer to form a mixed matrix films and their thermal and mechanical properties were investigated. It was found that the addition of bare zeolites to the polymer led to a decrease in the mechanical properties of the polymer composite. However, some of the adverse effects could be mitigated if the polymer is loaded with $Mg(OH)_2$ / zeolite 4A nanocomposites.

Isotherms for the adsorption of $Mg(OH)_2$ petals on zeolite 4A were measured in order to determine optimum conditions for the formation of nanocomposites at ambient conditions. The loading of the $Mg(OH)_2$ was determined from the adsorption isotherms. It was also found that the adsorption of $Mg(OH)_2$ on zeolite A yields H-type isotherms and involves 3 mechanisms: ion exchange, surface adsorption of Mg^{2+} ions, and surface precipitation of $Mg(OH)_2$. H-type isotherms indicate that there may be very strong specific interactions between $Mg(OH)_2$ and zeolite 4A. In the absence of a base such as ammonium hydroxide, the predominant processes are ion exchange and surface

adsorption of Mg^{2+} ions. In the presence of ammonium hydroxide, $Mg(OH)_2$ crystals are precipitated on the surface of zeolite 4A at moderate Mg^{2+} ions concentration. The loading of $Mg(OH)_2$ increases with increasing Mg^{2+} ions concentration.

A detailed examination of the interactions between $Mg(OH)_2$ and functional groups on the zeolite surface was conducted. Solid-state ^{29}Si, ^{27}Al, and ^{1}H NMR spectra were coupled with FTIR measurements, pH and adsorption studies, and thermogravimetric analyses to determine the interactions of $Mg(OH)_2$ with surface functional groups and to characterize structural changes in the resulting zeolite after $Mg(OH)_2$ deposition. It was discovered that acid – base interactions between the weakly basic $Mg(OH)_2$ and the acidic bridging hydroxyl protons on zeolite surface represent the dominant mechanism for the growth of $Mg(OH)_2$ nanostructures on the zeolite surface. This suggests that precipitation combined with self-assembly on specific sites of zeolite may be used to make functional hydroxide / zeolite or oxide / zeolite composites for applications in catalysis, gas sensing, and membranes.

CHAPTER 1

INTRODUCTION

Nanoscale metal oxides are technologically important materials because of their superior optical, magnetic, electrical, and catalytic properties [1-3]. In the chemical industry, nanoscale metal oxides are the functional components of catalysts used in processes to convert hydrocarbons to other chemicals [4]. They are also used as electrode materials in electrochemical processes [5]. Nanoscale metal oxides are also excellent chemical sensors as their electrical conductivity is very sensitive to the composition of surrounding gases [3]. Significant advances have also been made in the integration of these oxides into functional devices. For example, piezoelectric nanogenerators based on zinc oxide nanowrie arrays have recently been fabricated by Wang et al. [6]. The performance of these devices depends on the size, shape, and morphology of the particles used in making the devices [7], and their long term stability at high temperatures [3]. Therefore, methods for controlling the size, shape, morphology, and stability of nanoscale metal oxides are of practical interest.

Teja and co-workers [1, 5, 8-12] have investigated the synthesis of several nanoscale metal oxides using supercritical hydrothermal synthesis. Their studies included the development of approaches to control the particle size and agglomeration and showed that the polydispersity, size, and crystallinity of iron oxide nanoparticles can be effectively controlled with PVA. In another study, they showed that agglomeration of iron oxide nanoparticles can be minimized by depositing them in activated carbon [13]. However, they did not investigate the interactions of these oxides with the carbon supports. Since controlled fabrication of functional devices will undoubtedly involve

supporting materials [14], a detailed understanding of growth mechanisms, and interactions of the nanostructures with supports, as well as identification of the optimal processing parameters is essential.

The goals of this work were (1) develop a method for the fabrication of metal oxide nanostructures on surfaces; (2) determine optimum conditions for the deposition of magnesium hydroxide nanostructures on zeolite 4A; and (3) develop an understanding of metal oxide – surface interactions in order to control the deposition and assembly of specific nanostructures. Magnesium hydroxide and zeolite 4A were chosen for study because of their potential applications in catalysis, adsorbents, and CO_2 capture and sequestration, and because zeolite 4A offers several sites for acid-base interactions with magnesium hydroxide. Due to the basic and acidic nature of the magnesium hydroxide and zeolite 4A surface functional groups, it was hypothesized that acid – base interactions between the weakly basic magnesium hydroxide and the acidic bridging hydroxyl protons on the zeolite surface could be employed for the control of the growth of magnesium hydroxide nanostructures on the zeolite surfaces. Background information on the synthesis and unique properties of zeolites are detailed in Chapter 2.

In Chapter 3, an investigation of the deposition – precipitation method for the fabrication of magnesium hydroxide / zeolite 4A nanocomposite is described. The effects of the processing parameters such as concentration of precursor, chemical nature of base, and synthesis time on the nanocomposite characteristics are investigated. The properties of the resultant magnesium hydroxide / zeolite 4A nanocomposite and its effects on the mechanical properties of Ultem® polymer are detailed in chapter 4.

In Chapter 5, adsorption isotherms are determined to provide a macroscopic understanding of the deposition of magnesium hydroxide on zeolite surfaces. These isotherms are coupled with pH studies to identify optimum processing conditions for the fabrication of the nanocomposites and to gain insights into the effect of the local environment on growth and deposition of the nanostructures.

In Chapter 6, microscopy and spectroscopy are used to provide a microscopic understanding of the interactions between magnesium hydroxide and zeolite surface functional groups. The structural changes of the magnesium hydroxide / zeolite nanocomposite are extensively characterized and examined. Adsorption studies are also carried out on silica and alumina to deduce the roles of silanol and aluminol sites on the adsorption of magnesium hydroxide. The results of these experiments are used to postulate the deposition mechanism and to validate the hypothesis of this work.

These investigations provide a detailed understanding of the site specific interactions and structural changes of a basic metal hydroxide such as $Mg(OH)_2$ in zeolite 4A. The understanding of the zeolitic guest – hosts relationship and self assembly of metal oxides/ hydroxides nanostructures on zeolite will widen the existing application fields and open new fields for zeolite application in semiconductor, biochemistry, medicine, and chemical sensors.

References

1. Xu, C., *Continuous and batch hydrothermal synthesis of metal oxide nanoparticles and metal oxide-activated carbon nanocomposites*. 2006, Georgia Institute of Technology: United States -- Georgia. p. 258.

2. Kung, H.H., *Transition metal oxides : surface chemistry and catalysis*. Studies in surface science and catalysis ;. 1989, Amsterdam, The Netherlands, ;: Elsevier ;.

3. Comini, E. and G. Sberveglieri, *Metal oxide nanowires as chemical sensors.* Materials Today. **13**(7-8): p. 36-44.

4. *Zeolites for cleaner technologies*. Catalytic science series ;, ed. M. Guisnet and J.-P. Gilson. 2002, London :: Imperial College Press.

5. Lee, J. and A.S. Teja, *Synthesis of $LiFePO_4$ micro and nanoparticles in supercritical water.* Materials Letters, 2006. **60**(17-18): p. 2105-2109.

6. Wang, Z.L. and J. Song, *Piezoelectric Nanogenerators Based on Zinc Oxide Nanowire Arrays.* Science, 2006. **312**(5771): p. 242-246.

7. Zheng, N. and G.D. Stucky, *A General Synthetic Strategy for Oxide-Supported Metal Nanoparticle Catalysts.* Journal of the American Chemical Society, 2006. **128**(44): p. 14278-14280.

8. Xu, C. and A.S. Teja, *Continuous hydrothermal synthesis of iron oxide and PVA-protected iron oxide nanoparticles.* The Journal of Supercritical Fluids, 2008. **44**(1): p. 85-91.

9. Hao, Y.L. and A.S. Teja, *Continuous hydrothermal crystallization of □-Fe_2O_3 and Co_3O_4 nanoparticles.* Journal of Materials Research, 2003. **18**(2): p. 415-422.

10. Lee, J. and A.S. Teja, *Characteristics of lithium iron phosphate ($LiFePO_4$) particles synthesized in subcritical and supercritical water.* Journal of Supercritical Fluids, 2005. **35**(1): p. 83-90.

11. Cote, L.J., A.S. Teja, A.P. Wilkinson, and Z.J. Zhang, *Continuous hydrothermal synthesis and crystallization of magnetic oxide nanoparticles.* Journal of Materials Research, 2002. **17**(9): p. 2410-2416.

12. Cote, L.J., A.S. Teja, A.P. Wilkinson, and Z.J. Zhang, *Continuous hydrothermal synthesis of $CoFe_2O_4$ nanoparticles.* Fluid Phase Equilibria, 2003. **210**(2): p. 307-317.

13. Kastner, J.R., R. Ganagavaram, P. Kolar, A. Teja, and C.B. Xu, *Catalytic ozonation of propanal using wood fly ash and metal oxide nanoparticle impregnated carbon.* Environmental Science & Technology, 2008. **42**(2): p. 556-562.

14. Mathur, S., H. Shen, and N. Donia, *Chemical Nanotechnology: From Molecules to Applications.* ECS Transactions, 2006. **3**(9): p. 3-13.

CHAPTER 2

LITERATURE REVIEW

2-1 Introduction

$Mg(OH)_2$ or brucite belongs to the family of divalent metal hydroxides $M(OH)_2$, with M = Mg, Ca, Ni, Co, Fe, Mn or Cd, which are isostructural with the layered compound CdI_2 (space group *P3ml)*. The crystal structure of brucite is shown in Fig. 2.1, and consists of a hexagonal close-packed array of OH^- ions, in which alternate layers of octahedral holes are occupied by Mg^{2+} ions. The hydroxyl groups (OH), which are directed along the threefold axes, are bonded to three M cations. In interlayer spacings, they are surrounded by three other (OH) groups belonging to an adjacent layer [2]. Thus there is a layered structure of $\cdots HO^- Mg^{2+} OH^- OH^- Mg^{2+} OH^- \cdots$ which can easily be cleaved between the similarly-charged OH^- layers [3]. It has been reported that such a layered crystal structure offers an advantage for platelet-like crystallization of $Mg(OH)_2$ [4].

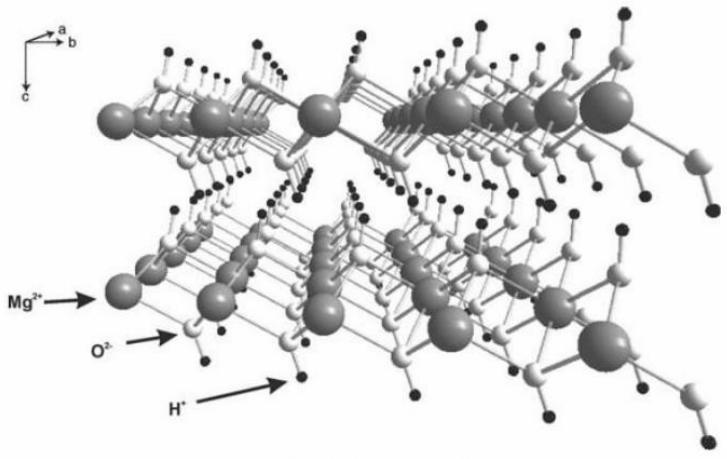

Fig. 2.1 Crystal structure of brucite. Adapted from [5].

Magnesium hydroxide ($Mg(OH)_2$) is also a nontoxic, noncorrosive, thermally stable, and environment friendly flame retardant which undergoes endothermic dehydration under fire conditions and suppressing fumes [6]. Its nanoneedles and nanolamellas are good candidates for functional polymeric composites, fiber hybrid materials, and as reinforcing agents or halogen-free flame-retardants [7, 8]. In addition, magnesium hydroxide is also used as a neutralizer in the treatment of acid wastewater and gases rich in sulfuric oxides [9]. It also finds use as an antacid excipient in pharmaceuticals [10], and in mixed matrix membranes for natural gas separation [11-13]. Magnesium hydroxide is a precursor for the preparation of magnesium oxide and retains its crystallite size and morphological features after decomposition to MgO [6]. Thus magnesium hydroxide nanorods can be used as precursors for the synthesis of magnesium oxide nanorods, which have novel mechanical, catalytic and electronic properties [14, 15]. Finally, it has recently been demonstrated that magnesium hydroxide can play a key role in the mineral sequestration of CO_2 [15].

Magnesium hydroxide nanostructures have been be prepared by several methods including hydrothermal processing [7, 16, 17], ultrasonication [6], microwave-assisted synthesis [18], pulse laser induced reaction [14], coprecipitation [19], and sol-gel processing [20]. It has been reported that physical synthesis methods such as ultrasonication, microwave-assisted synthesis, and pulse laser induced reaction are characterized by relatively low yields, large size distribution, and polydispersity [19]. On the other hand, Klabunde et al. [21] were able to prepare ultrahigh surface area $Mg(OH)_2$ particles of ~5 nm via a sol gel technique followed by a hypercritical drying process. However, the need to synthesize and handle costly and hazardous metal-organic

precursors in the sol-gel procedure is disadvantages as pointed out by Qian et al. [16]. The hydrothermal method offers control of the size, shape, and structure of $Mg(OH)_2$ [16] and has been used to prepare rod-like, tube-like, and plate-like $Mg(OH)_2$ nanocrystallites [7, 16, 17].

As discussed earlier, magnesium hydroxide is often used as an intermediate for the preparation of magnesium oxide (MgO) [22], which has been used as solid base catalyst for a variety of organic transformations [23]. For example, MgO is an active catalyst for double bond isomerization and displays excellent activity for isomerization of 1-butene and 1,4-pentadiene, allylamine, and 2-propenyl ethers [23, 24]. Furthermore, MgO has also demonstrated marked increase in activity and selectivity to diacetone alcohol during aldol condensations [25]. In addition, MgO and $Mg(OH)_2$ have also been used in the carbon-oxygen bond formation reactions such as cyanoethylation of methanol [26, 27]. The reactivity of these catalysts was related to the acidity of the alcohol and the basic strength of the catalyst [23]. It has been shown that the activity of MgO catalyst is hardly affected by exposure to air and is tolerant to water and carbon dioxide [23]. This is why solid MgO catalyst can be used in a practical process [27].

The activity of MgO nanoparticles in catalysis is limited by its tendency to agglomerate [28] which reduces the total surface area available for catalytic activity. To overcome these limitations, MgO if often incorporated into zeolites to create strong basic zeolites [29]. Dumitriu et al. [30] has shown that MgO supported on HZSM-5 displayed high catalytic activity and selectivity in the synthesis of acrolein. This enhancement was attributed to the spatial limitations of the zeolitic structure, and to cooperative effects of the basic centers of MgO and the acidic sites of HZSM-5. However, although zeolites

loaded with MgO display strong basic properties, the basic sites on fine MgO nanoparticles are not as strong as those of bulk MgO. The ionicity of the Mg – O bond is reduced in fine MgO particles when compared to bulk MgO, and therefore the basic strength of the O^{2-} ion is reduced [24]. The dependence of the particle size on the strength of basic sites has been studied by Itoh el al. [31] who concluded that the larger MgO hexagonal platelets exhibit stronger basicity than smaller MgO particles.

2-2 Zeolites as supports for metal oxides

Zeolites are crystalline aluminosilicates with a 3- dimensional, open anion framework consisting of oxygen-sharing SiO_4 and AlO_4^- tetrahedra [32-34]. Each silicon ion has its +4 charge balanced by four tetrahedral oxygens, and the silica tetrahedra are therefore electrically neutral. Each alumina tetrahedron has a residual charge of -1 since the trivalent aluminum is bonded to four oxygen anions. Therefore, each alumina tetrahedron requires a +1 charge from a cation in the structure to maintain electrical neutrality [33]. These cations are usually sodium ions that are present when the zeolite is synthesized [35]. The zeolite framework structure contains interconnected voids that can be filled with adsorbed molecules or cations which in turn govern the zeolite pore size. Zeolite micropore channels have very well-defined diameters that depend on the number of tetrahedra in a ring. The silica and alumina tetrahedra are geometrically arranged and combined to form the building blocks of the framework zeolite crystal structures. The general structural formula of a zeolite is: $M_{x/n}(AlO_2)_x(SiO_2)_y$ where n is the valence of cation M which balances the negative charge associated with the framework aluminum ions, (x + y) is the total number of tetrahedra per unit cell and y/x is the atomic Si/Al ratio that varies from a minimal value of 1 [36]. The structures of aluminosilicate zeolites

obey the Löwenstein Rule [36], which states that when two tetrahedra are joined by one oxygen bridge, the center of only one of them can be occupied by aluminum; the other center must be occupied by silicon or by another small ion of electrovalence 4 or more [37]. In addition, whenever two aluminum ions are neighbors to the same oxygen anion, at least one of them must have a coordination number larger than 4 towards oxygen [37].

The zeolite used in this study is known as zeolite A. Zeolite A exhibits the LTA (Linde type A) structure [38] which is shown schematically in Fig. 2.2 without cations. The structural formula of a fully hydrated LTA is $|Na_{12}^{+}(H_2O)_{27}|_8[Al_{12}Si_{12}O_{48}]_8$ [36]. The aluminosilicate framework of zeolite A can be described in terms of two types of polyhedra; one being a simple cubic arrangement of eight polyhedra (the double 4-rings); the other being a truncated octahedron of 24 tetrahedra or *β*- cage. In LTA, sodalite cages are joined via double 4-rings, creating an *α*- cage in the center of the unit cell. Alternatively, the framework can be described as a primitive cubic arrangement of α-cages joined through single 8- rings. Zeolite A has a three-dimensional pore system and molecules can diffuse in all three directions in space by moving across the 8-ring windows of about 0.45 nm diameter that connect the cavities. The size of the pore openings depends on the size of the respective cations residing in the zeolites. Normally, zeolite A is synthesized in the Na-form which gives it a pore opening of about 0.4 nm. The sodium cations can be exchanged with other cations, thereby tuning the size of the pore openings.

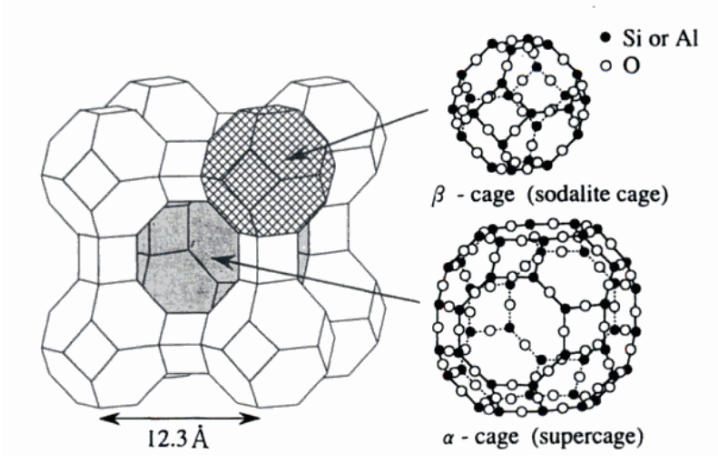

Fig. 2.2 Framework structure of zeolite LTA. The β- cages are connected at the 4-membered rings in a simple cubic structure. Open and closed circles represent Si, Al and O atoms, respectively. Adapted from [39].

In a typical zeolite, the -1 net negative charge introduced by the alumina tetrahedron is balanced by a cation. The presence of cations in the zeolite creates acid sites if protons act as counterions. These acid sites are associated with bridging hydroxyl groups attached to framework oxygens linking tetrahedral Si and Al atoms: (Al(OH)Si). These acid sites are strong Brönsted acids and the oxobridges connecting the Si and Al atoms exhibit Lewis base properties [34]. However, the Brönsted acid sites are converted to Lewis acid sites when the proton concentration drops below the aluminum concentration [35]. The maximum number of protonic sites is equal to the number of framework aluminum atoms, but the actual number could be smaller due to cation exchange, dehydroxylation and dealumination during activation at high temperatures [34]. The number and density of protonic sites can therefore be adjusted either during synthesis or during post synthesis treatment of the zeolite. In addition to the bridging hydroxyl protons, there are structural hydroxyls like silanol (Si-OH) and aluminol (Al-OH) groups located on the external surface of the zeolite [40]. These structural hydroxyl groups show an ampholytic behavior and can act as an acid or a base – depending on the

solution pH. Therefore, depending on the solution pH, positively or negatively charged local sites may exist on the external surface of zeolites [40]. Since all of these different types of OH groups can influence the catalytic and adsorptive properties of zeolites, a detailed study is essential for deeper understanding of the behavior of zeolites.

Zeolites are widely used in a variety of industrial applications. One of the most prominent applications is in catalysts for organic reactions because the pores of zeolites are similar in size to small organic molecules. Zeolite pores have also shown the ability to recognize, discriminate, and organize molecules with high precision [41]. Furthermore, the catalytic properties of the zeolites can be easily controlled by a variety of synthetic and post-synthetic methods. By choosing the appropriate organic template and synthesis conditions, the pore size and pore shape (dimensionality, intersections, cages) may be directly influenced [32]. Moreover, the acidity of the zeolite may be controlled through various methods such as Si/Al ratio, ion-exchange, and calcinations conditions [23]. Zeolites may also be used as shape-selective supports for active components. Their high thermal stability allows them to be used at high temperatures that often result in higher yields and easier heat recovery. All of these characteristics, particularly the control of structure and acidity, make zeolites well suited as catalysts or catalyst supports for organic reactions.

Zeolites are inherently acidic due to the the negative charge of the framework [41, 42]. When all of the cations present inside the zeolite are exchanged with H^+, many Brönsted acid sites are formed [33]. However, the acidity of the zeolites can be neutralized by specific cations for ion-exchange and by manipulating the Si/Al ratio of the zeolite framework. Wide variation of acid-base properties can be achieved by ion-

exchange and ion-addition, while relatively small change in acid-base properties is yielded by changing the Si/Al ratio [24]. The basicity of the zeolites can be enhanced by introducing alkaline oxides and alkaline earth oxides [43].

By inclusion of nanoscaled metal oxide or hydroxide guests inside the defined void spaces and/ or on the surface of the zeolite, new nanocomposites have been obtained with tunable catalytic, optical, magnetic or electrical properties [44]. For example, Dutta et al. [45] showed that RuO_2/ zeolite composites are efficient in catalyzing the reduction of water to hydrogen. Moreover, SnO_2/ zeolite NaY composites have also displayed excellent detecting sensitivity to hydrogen gas [46]. Also, Cao et al. [47-49] have fabricated an asymmetric supercapacitor using $Co(OH)_2$ / USY zeolite composites and the hybrid electrochemical capacitor exhibited higher energy and power characteristics. To date, zeolites have been shown to be excellent hosts for the synthesis of nanosized particles [45, 50-54]. However, guest – host interactions between zeolites and metal oxides / hydroxides have not been widely investigated and most studies have focused on the interactions between organic molecules and zeolites [43, 55-60]. The properties of zeolite – metal oxides / hydroxides nanocomposites depend on the shape, size, location, and coordination of the metal oxides / hydroxides [43, 44, 61, 62]. For example, it has been shown that the control of dispersed state of metal oxides and porosity of the zeolite is important to improve catalytic activities [52]. Therefore, it is important to understand guest – host interactions between zeolites and metal oxides / hydroxides and the role of such interactions play in determining the properties of the nanocomposites.

2-3 Preparation methods for zeolite host-guest composites

Many of the useful attributes of zeolite nanocomposites depend on the preparation method [43, 63-65], and these methods play a key role in determining the particle size, shape, size distribution, and surface chemistry. The preparation method also determines structural defects and the distribution of such defects in the particles. Many synthesis routes have therefore been developed to achieve proper control of particle size, polydispersity, shape, crystallinity, and functionality [64, 66-73]. The most commonly used methods such as chemical vapor deposition (CVD), sol-gel synthesis, halide/ Grignard reaction, ion exchange/ ion impregnation, solvothermal, hydrothermal, and deposition-precipitation are reviewed in the following section.

2-3-1 *Chemical vapor deposition* (*CVD*)

The chemical vapor deposition method for preparing nanomaterials depend on thermal decomposition (pyrolysis), reduction, hydrolysis, disproportionation, oxidation, or other reactions to precipitate solid products from the gas phase [74]. In the CVD process, a carrier gas stream with precursors is delivered continuously by a gas delivery system to a reaction chamber maintained under vacuum and temperatures greater than 900°C [69, 75]. The CVD reactions take place in the heated reaction chamber and the products combine to form clusters or nanoparticles. Growth and agglomeration of the particles are mitigated via rapid expansion of the two-phase gas stream at the outlet of the reaction chamber (Fig. 2.3). Subsequent heat treatment of the synthesized nanopowders in various high-purity gas streams allows compositional and structural modifications, including particle purification and crystallization, as well as transformation to a desirable

size, composition, and morphology [69, 74]. The CVD process has been employed to deposit single metal or bimetallic oxide catalysts on various zeolite matrices such as borosilicate, ZSM-5, β-zeolite, mordenite, silicalite, and Y-zeolite [76-85].

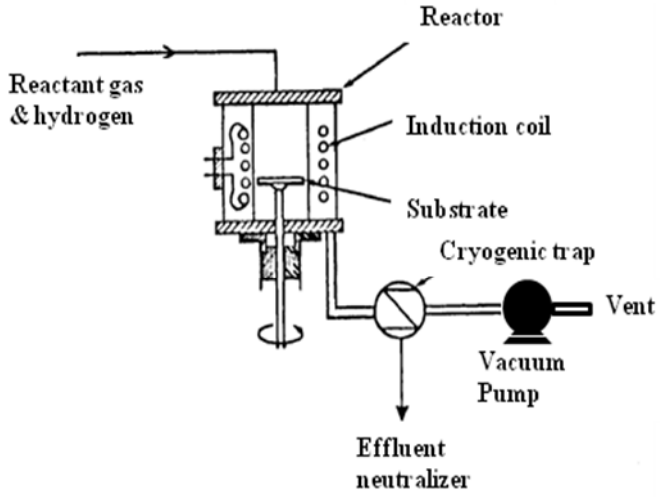

Fig. 2.3 Schematic diagram of a CVD apparatus (adapted from ref [1]).

The use of metallo-organics as precursors (in the MOCVD process) allows reactions to take place at somewhat lower temperatures (300-800 °C) and at pressures varying from less than 1 Torr to ambient [74]. Platinum based aluminosilicate catalysts have been prepared by Davis et al. by impregnating platinum acetylacetonates in zeolites under vacuum in a sealed tube at 418 K [86]. In addition, other noble metals such as gold [87, 88], palladium [89-91], rhodium [92-94], and ruthenium [95, 96] supported on silica, titania, zeolite and activated carbon have been prepared using organometallic complexes of these metals. Compared to conventional liquid phase methods such as wet impregnation or coprecipitation, the absence of any solvent favors diffusion of the precursor inside the pores and precludes the drying step during which redistribution of the active phase can occur [97]. In addition, the partial embedding of nanoparticles in the

bulk of the support can also be avoided [97]. The use of organometallic complexes as metal precursors provides an efficient way to produce deposits at relatively low temperatures. However, although the chemical vapor deposition methods are able to deliver high quality products, the yields are usually low and scale-up of the equipment is challenging. Variables such as oxygen concentration, gas phase impurities, and the heating time must be controlled precisely to obtain pure products [1].

2-3-2 *Sol-Gel methods*

Sol-gel methods generally refer to the hydrolysis and condensation of metal alkoxides or alkoxide precursors, leading to dispersions of oxide particles in a "sol". The "sol" is then dried or "gelled" by solvent removal or by chemical reaction. The solvent is generally water, but the precursors can also be hydrolyzed by an acid or base. Basic catalysis induces the formation of a colloidal gel, whereas acid catalysis yields a polymeric form of the gel [98]. The rates of hydrolysis and condensation are important parameters that affect the properties of the final products. Smaller particle sizes are obtained at slower and more controlled hydrolysis rates. The particle size also depends on the solution composition, pH, and temperature [69]. In the case of nanocomposites derived from gels, structural parameters and material porosity are determined by the rate of hydrolysis and condensation of the gel precursors and also by other oxidation-reduction reactions that occur during the gelling and subsequent heat treatment stages [69].

Iron oxide - silica aerogel composites have been prepared by the sol-gel method [99-101] and found to be 2-3 orders of magnitude more reactive than conventional iron

oxide [102]. The increase in reactivity was attributed to the large surface area of iron oxide nanoparticles supported on the silica aerogel [103, 104]. The sol-gel method has also been used to synthesize titanium – silicon binary oxide catalysts [105], transparent iron-doped titanium oxide thin films [106], ferroelectromagnetic bismuth iron oxide films [107], mixed iron oxides [108-113], and iron oxide-alumina nanocomposites [114].

Disadvantages of the sol-gel methods include contamination from byproducts of reactions, and the need for post-treatment of the products [1].

2-3-3 *Halide / Grignard reaction*

The halide/ Grignard reaction route pioneered by Shu and Hussain [12, 13] has been used to modify the external surface of zeolite 4A by deposition of magnesium hydroxide nanostructures on the zeolite surface. This treatment was shown to enhance adhesion when treated zeolite particles were dispersed in a polymer [12, 115]. In a typical halide / Grignard reaction, the zeolite to be treated is first dried under vacuum at 423 K for 8-12 h, dispersed in anhydrous toluene and thionyl chloride solution, purged with dry nitrogen gas and ultrasonicated in a bath for at least 4 h (up to 24 h). The mixture is then heated at 373-383 K to remove the solvent and the remaining dry cake redispersed in anhydrous toluene in an ultrasonic bath with a slow dry nitrogen purge. Methyl magnesium bromide is then added to the dispersed zeolite, followed by an additional 4 h of ultrasonication. Finally, the mixture is placed in an ice bath and quenched with anhydrous 2-propanol. Methyl magnesium bromide reacts with 2-propanol and generates methane and solid precipitates containing $MgBr_2$ and $Mg(OH)_2$.

In reactions involving Grignard reagents, it is important to ensure that no water is present since this would cause the reagents to decompose rapidly. Furthermore, it is also highly recommended to use fresh reagents when performing sieve treatments because the chemicals degrade quickly over time [115]. The halide/ Grignard reaction is time consuming, complex, and may result in dealumination of the zeolite [13]. Also, the reagents are extremely flammable and corrosive.

2-3-4 *Ion exchange and ion impregnation*

Metal oxide/ hydroxide nanostructures have been prepared in the pores or exterior of zeolites by ion exchange or ion impregnation methods followed by in situ post-treatment [46, 50, 116-127]. The ion exchange process consists of replacing an ion in an electrostatic interaction with the surface of a support by another ion species [128]. The support containing ions A is added to an excess solution containing ions B. Ions B gradually penetrate into the pore space of the support, while ions A pass into the solution until equilibrium is established between the solid and solution. Ion impregnation is similar in concept to ion exchange, except there is no exchange of ions between the support and the solution containing the precursor of the active phase [128]. In both ion exchange and impregnation methods, subsequent calcination is required to convert the metal cations into metal oxides.

Ion exchange and ion impregnation are the simplest supported zeolite preparation procedures and provide minimal liquid waste generation and easy control of metal loading when the solubility of the precursor compound is high [129]. They are therefore widely used. However, these methods do not result in the best distribution of metal

oxides on zeolites, and often do not provide adequate control of particle shape, size, and size distribution [118]. Furthermore, ion exchange in the liquid phase can be limited by steric constraints due to the formation of bulky hydration shells of the exchangeable cations and the calcination step may result in undesirable changes, such as modification of the pore structure and mechanical properties [130]. Multiple impregnation steps are necessary when the solubility of the precursor is limited and zeolite composite with high loadings of the active compound is to be made [130, 131]. Furthermore, the concentration profile of the impregnated compound depends on the mass transfer conditions within the pores during impregnation and drying [130].

2-3-5 *Solvothermal methods*

Solvothermal methods are relatively mild method for the fabrication of nanoscale metal oxides. They involve dissolving inorganic and/ or organometallic precursors in a suitable solvent and conducting the reactions in autoclaves normally at temperatures above the boiling point of the solvent [132]. The solvothermal methods differ slightly from hydrothermal methods in that a non-aqueous solvent is typically used [133]. Various metal oxides [134-136] and nanocomposites [11, 137, 138] have been prepared by solvothermal reactions. It has been shown that most of the solvothermal products are nano- or microparticles with well-defined morphologies, narrow size distribution, and monodisperse [139]. When the solvent molecules or additives are preferentially adsorbed on a certain surface of the products, growth of the surface is prohibited and therefore products with unique morphologies such nanorods, wires, tubes, and sheets may be formed by the solvothermal reactions [133]. For example, whisker-like $Mg(OH)_2$ nanostructures have been deposited on a pure-silica zeolite by Bae et al.[11].

2-3-6 *Hydrothermal methods*

Hydrothermal methods rely on the ability of water at varying pressures and temperatures to hydrolyze and dehydrate metal salts, and the very low solubility of the resulting metal oxides in water at these conditions to generate supersaturation [1, 69]. Often, elevated temperatures favor high dehydration rates, as does the high diffusivity of reactants in water at these conditions [140, 141]. Very high supersaturations can be achieved in this process because of the very low solubility of metal hydroxides and oxides, so that very fine crystals are obtained [98, 140, 142, 143]. Parameters such as pressure, temperature, reaction time, and the precursor – product system can be tuned to maintain high nucleation rates and to control growth [144, 145]. The process is environmentally benign and versatile, since it does not generally involve any organic solvents or post-treatments such as calcination [146]. As a result, high pressure hydrothermal processes have been widely investigated for the synthesis of metal oxides [67, 147-150] as powders, nanoparticles and single crystals [69, 151].

The hydrothermal synthesis of nanomaterials such as iron oxides can also be performed in situ within porous structures. Xu and Teja [71, 152] have successfully deposited hematite in the pores of activated carbon pellets using supercritical water. The hematite nanoparticles were 16-36 nm in diameter and were uniformly distributed throughout the pellets. Moreover, transition metal oxides such as titanium [153, 154] and chromium oxides [155, 156] photocatalysts can be designed within the cavities and frameworks of various zeolites and mesoporous molecular sieves by hydrothermal synthesis [157].

2-3-7 *Deposition – precipitation*

The deposition – precipitation method is similar to the hydrothermal method in which the metal oxides/ hydroxides are precipitated out of the aqueous solution by lowering their solubilities. However, this method is usually non-thermal driven and typically carried out at ambient conditions. The essence of this method is that small crystallites of metal hydroxide or carbonate precipitate from solution, preferably by heterogenous nucleation at the interface between the liquid and support [158]. This method consists of the conversion of a highly soluble metal precursor into another substance of lower solubility, which specifically precipitates onto a support and not in solution [159]. The conversion into the low soluble compound (above the saturation curve S in Fig. 2.4), and then into the precipitate (above the supersaturation curve SS in Fig. 2.4), is usually achieved by raising the pH of the solution.

To perform the precipitation exclusively on the surface of the support, two conditions must be fulfilled [159]:

1. Interaction between the soluble metal precursor and the surface of the support is required. In such a case, the supersaturation curve SS in Fig. 2.4 is shifted towards lower concentrations in the presence of the support (curve $SS_{support}$ in Fig. 2.4). Thus, when the concentration of the precursor increases, this supersaturation curve (curve $SS_{support}$) is encountered before the supersaturation curve (curve SS) .

2. The concentration of the precursor must be maintained between the concentrations of the saturation (curve S) and the supersaturation curves (curve SS) to avoid precipitation in solution.

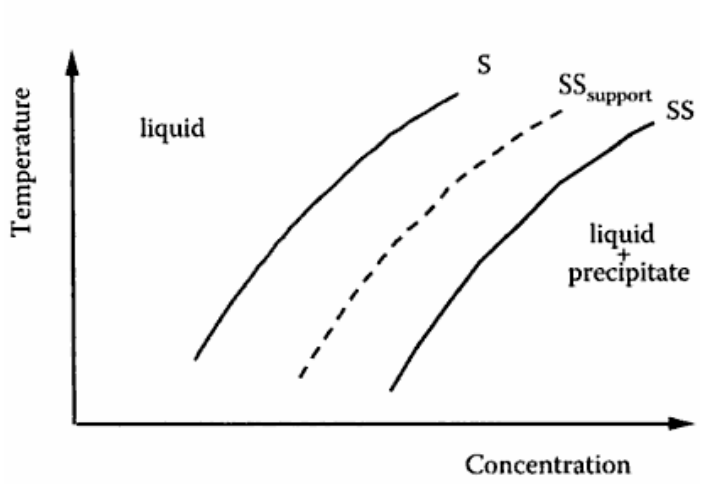

Fig. 2.4 Schematic phase diagram for a precipitate in equilibrium with its solution and in the presence of the solid support; (S) solubility curve; ($SS_{support}$) supersaturation curve in the presence of the support (precipitation on the support); (SS) supersaturation curve in liquid (precipitation in liquid). Adapted from [159].

According to Hermans and Geus [159], interaction with the support decreases the nucleation barrier as long as nucleation at the surface of the support can proceed at a concentration between the solubility and the supersaturation curve. Therefore, at concentrations between those of the supersaturation curves, $SS_{support}$ and SS, the compound exclusively precipitates onto the support surface.

Typically, hydroxides and carbonates are the preferred precipitated intermediates using the deposition - precipitation method for the following reasons [160]:

(1) Solubility of certain salts of alkaline earth metal and transition metals are very low. Consequently, very high supersaturations can be achieved, leading to very small particle sizes.

(2) Hydroxides and carbonates are easily decomposed by heat to oxides of high area without leaving potential catalyst poisons (for example, the sulfur left after sulfate calcinations).

(3) Minimum safety and environmental problems resulting from the calcinations of hydroxides and carbonates.

A number of zeolite supported nanomaterials such as gold [161-163], nickel [164], and cobalt hydroxides [48, 49] have been prepared using this method. In addition, this method has also been used to prepare Ni [165], titania [166], copper oxides [167], gold [168] on other matrices such as silica, ceria, and titania. In principle, the deposition-precipitation method enables the deposition of a controlled amount of metal precursor up to high loading, and the interaction between the metal precursor and the support leads to the formation of highly dispersed active phase after thermal treatment [131, 159].

2-4 References

1. Teja, A.S. and P.-Y. Koh, *Synthesis, properties, and applications of magnetic iron oxide nanoparticles.* Progress in Crystal Growth and Characterization of Materials. **55**(1-2): p. 22-45.

2. Desgranges, L., G. Calvarin, and G. Chevrier, *Interlayer interactions in $M(OH)_2$: A neutron diffraction study of $Mg(OH)_2$.* Acta Crystallographica Section B-Structural Science, 1996. **52**: p. 82-86.

3. Wiberg, E., N. Wiberg, and A.F. Holleman, *Inorganic chemistry*. 2001, San Diego, Calif. : Berlin: Academic Press, W. de Gruyter.

4. Zou, G.L., R. Liu, and W.X. Chen, *Highly textural lamellar mesostructured magnesium hydroxide via a cathodic electrodeposition process.* Materials Letters, 2007. **61**(10): p. 1990-1993.

5. Shand, M.A., W. John, Sons, and I. Wiley, *The chemistry and technology of magnesia*. 2006, Hoboken, N.J.: John Wiley & Sons.

6. Alavi, M.A. and A. Morsali, *Syntheses and characterization of $Mg(OH)_2$ and MgO nanostructures by ultrasonic method.* Ultrasonics Sonochemistry. **17**(2): p. 441-446.

7. Henrist, C., J.P. Mathieu, C. Vogels, A. Rulmont, and R. Cloots, *Morphological study of magnesium hydroxide nanoparticles precipitated in dilute aqueous solution.* Journal of Crystal Growth, 2003. **249**(1-2): p. 321-330.

8. Lv, J., L. Qiu, and B. Qu, *Controlled growth of three morphological structures of magnesium hydroxide nanoparticles by wet precipitation method.* Journal of Crystal Growth, 2004. **267**(3-4): p. 676-684.

9. Booster, J.L., A. Van Sandwijk, and M.A. Reuter, *Conversion of magnesium fluoride to magnesium hydroxide.* Minerals Engineering, 2003. **16**(3): p. 273-281.

10. Kang, J. and S.P. Schwendeman, *Comparison of the effects of Mg(OH)2 and sucrose on the stability of bovine serum albumin encapsulated in injectable poly(,-lactide-co-glycolide) implants.* Biomaterials, 2002. **23**(1): p. 239-245.

11. Bae, T.H., J.Q. Liu, J.S. Lee, W.J. Koros, C.W. Jones, and S. Nair, *Facile high-yield solvothermal deposition of inorganic nanostructures on zeolite crystals for mixed matrix membrane fabrication.* Journal of the American Chemical Society, 2009. **131**(41): p. 14662-14663.

12. Shu, S., S. Husain, and W.J. Koros, *A general strategy for adhesion enhancement in polymeric composites by formation of nanostructured particle surfaces.* The Journal of Physical Chemistry C, 2007. **111**(2): p. 652-657.

13. Shu, S., S. Husain, and W.J. Koros, *Formation of nanostructured zeolite particle surfaces via a halide/Grignard route.* Chemistry of Materials, 2007. **19**(16): p. 4000-4006.

14. Liang, C., T. Sasaki, Y. Shimizu, and N. Koshizaki, *Pulsed-laser ablation of Mg in liquids: surfactant-directing nanoparticle assembly for magnesium hydroxide nanostructures.* Chemical Physics Letters, 2004. **389**(1-3): p. 58-63.

15. McKelvy, M.J., R. Sharma, A.V.G. Chizmeshya, R.W. Carpenter, and K. Streib, *Magnesium hydroxide dehydroxylation: In situ nanoscale observations of lamellar nucleation and growth.* Chemistry of Materials, 2001. **13**(3): p. 921-926.

16. Ding, Y., G. Zhang, H. Wu, B. Hai, L. Wang, and Y. Qian, *Nanoscale magnesium hydroxide and magnesium oxide powders: Control over size, shape, and structure via hydrothermal synthesis.* Chem. Mater., 2001. **13**(2): p. 435-440.

17. Jiang, W.J., X. Hua, Q.F. Han, X.J. Yang, L.D. Lu, and X. Wang, *Preparation of lamellar magnesium hydroxide nanoparticles via precipitation method.* Powder Technology, 2009. **191**(3): p. 227-230.

18. Wu, H., M. Shao, J. Gu, and X. Wei, *Microwave-assisted synthesis of fibre-like Mg(OH)2 nanoparticles in aqueous solution at room temperature.* Materials Letters, 2004. **58**(16): p. 2166-2169.

19. Chen, D., L. Zhu, H. Zhang, K. Xu, and M. Chen, *Magnesium hydroxide nanoparticles with controlled morphologies via wet coprecipitation.* Materials Chemistry and Physics, 2008. **109**(2-3): p. 224-229.

20. Baird, T., P.S. Braterman, H.D. Cochrane, and G. Spoors, *Magnesium hydroxide precipitation as studied by gel growth methods.* Journal of Crystal Growth, 1988. **91**(4): p. 610-616.

21. Utamapanya, S., K.J. Klabunde, and J.R. Schlup, *Nanoscale metal oxide particles/clusters as chemical reagents. Synthesis and properties of ultrahigh surface area magnesium hydroxide and magnesium oxide.* Chemistry of Materials, 1991. **3**(1): p. 175-181.

22. Aramendia, M.A., J.A. Benitez, V. Borau, C. Jimenez, J.M. Marinas, J.R. Ruiz, and F. Urbano, *Characterization of various magnesium oxides by XRD and H-1 MAS NMR spectroscopy.* Journal of Solid State Chemistry, 1999. **144**(1): p. 25-29.

23. Corma, A., S. Iborra, C.G. Bruce, and K. Helmut, *Optimization of Alkaline Earth Metal Oxide and Hydroxide Catalysts for Base-Catalyzed Reactions*, in *Advances in Catalysis*. 2006, Academic Press. p. 239-302.

24. Hattori, H., *Heterogeneous basic catalysis.* Chemical Reviews, 1995. **95**(3): p. 537-558.

25. Hattori, H., *Catalysis by basic metal oxides.* Materials Chemistry and Physics. **18**(5-6): p. 533-552.

26. Kabashima, H., H. Tsuji, and H. Hattori, *Michael addition of methyl crotonate over solid base catalysts.* Applied Catalysis A: General, 1997. **165**: p. 319-325.

27. Kabashima, H. and H. Hattori, *Cyanoethylation of methanol catalyzed by alkaline earth oxides and alumina-supported K catalysts.* Applied Catalysis A-General, 1997. **161**(1-2): p. L33-L35.

28. Zhu, J.H., Y. Wang, Y. Chun, Z. Xing, and Q.H. Xu, *MgO/KL: strong basic zeolite prepared by microwave radiation.* Materials Letters, 1998. **35**(3-4): p. 177-182.

29. Hattori, H., *Solid base catalysts: generation of basic sites and application to organic synthesis.* Applied Catalysis A: General, 2001. **222**(1-2): p. 247-259.

30. Dumitriu, E., V. Hulea, N. Bilba, G. Carja, and A. Azzouz, *Synthesis of acrolein by vapor-phase condensation of formaldehyde and acetaldehyde over oxides loaded zeolites.* Journal of Molecular Catalysis, 1993. **79**(1-3): p. 175-185.

31. Itoh, H., S. Utamapanya, J.V. Stark, K.J. Klabunde, and J.R. Schlup, *Nanoscale metal oxide particles as chemical reagents. Intrinsic effects of particle size on hydroxyl content and on reactivity and acid/base properties of ultrafine magnesium oxide.* Chem. Mater., 1993. **5**(1): p. 71-77.

32. Bhatia, S., *Zeolite catalysis : Principles and applications*. 1990, Boca Raton, Fla. :: CRC Press.

33. Breck, D.W., *Zeolite molecular sieves: Structure, chemistry, and use.* . 1973, New York: John Wiley & Sons.

34. *Zeolites for cleaner technologies*. Catalytic science series ;, ed. M. Guisnet and J.-P. Gilson. 2002, London :: Imperial College Press.

35. Cheetham, A.K., *Solid state chemistry : Compounds*. Oxford science publications, ed. A.K. Cheetham and P. Day. 1992, Oxford [England] :: Clarendon Press ;.

36. *Chemistry of zeolites and related porous materials : Synthesis and structure*, ed. R. Xu. 2007, Singapore ;: John Wiley & Sons (Asia).

37. Szostak, R., *Molecular sieves*. 1997, London: Blackie Academic & Professional.

38. *Surface and nanomolecular catalysis*, ed. R. Richards. 2006, Boca Raton, FL :: CRC/Taylor & Francis.

39. Ogawa, T., *Optical properties of low-dimensional materials*. 1995, Singapore [u.a.: World Scientific Publ.

40. Roehl, K.E., ed. *Long-term performance of permeable reactive barriers*. Trace metals and other contaminates in the environment, ed. J.O. Nriagu. Vol. 7. 2005, Elsevier: Amsterdam; London. 326.

41. Dartt, C.B. and M.E. Davis, *Applications of zeolites to fine chemicals synthesis.* Catalysis Today, 1994. **19**(1): p. 151-186.

42. Makarova, M.A., V.L. Zholobenko, K.M. Alghefaili, N.E. Thompson, J. Dewing, and J. Dwyer, *Bronsted acid sites in zeolites - FTIR study of molecular-hydrogen as a probe for acidity testing.* Journal of the Chemical Society-Faraday Transactions, 1994. **90**(7): p. 1047-1054.

43. Bein, T., *Zeolitic host-guest interactions and building blocks for the self-assembly of complex materials.* MRS Bulletin, 2005. **30**(10): p. 713-720.

44. Simon, U. and M.E. Franke, *Electrical properties of nanoscaled host/guest compounds.* Microporous and Mesoporous Materials, 2000. **41**(1-3): p. 1-36.

45. Dutta, P.K. and A.S. Vaidyalingam, *Zeolite-supported ruthenium oxide catalysts for photochemical reduction of water to hydrogen.* Microporous and Mesoporous Materials, 2003. **62**(1-2): p. 107-120.

46. Xu, X., J. Wang, and Y. Long, *Nano-tin dioxide/NaY zeolite composite material: Preparation, morphology, adsorption and hydrogen sensitivity.* Microporous and Mesoporous Materials, 2005. **83**(1-3): p. 60-66.

47. Liang, Y.-Y., H.-L. Li, and X.-G. Zhang, *A novel asymmetric capacitor based on $Co(OH)_2$/USY composite and activated carbon electrodes.* Materials Science and Engineering: A, 2008. **473**(1-2): p. 317-322.

48. Liang, Y.Y., L. Cao, L.B. Kong, and H.L. Li, *Synthesis of $Co(OH)_2$/USY composite and its application for electrochemical supercapacitors.* Journal of Power Sources, 2004. **136**(1): p. 197-200.

49. Cao, L., F. Xu, Y.Y. Liang, and H.L. Li, *Preparation of the novel nanocomposite $Co(OH)_2$/ ultra-stable Y zeolite and its application as a supercapacitor with high energy density.* Advanced Materials, 2004. **16**(20): p. 1853-+.

50. Kovacheva, P., A. Predoeva, K. Arishtirova, and S. Vassilev, *Oxidative methylation of toluene with methane using X zeolite catalyst modified with alkali earth oxides.* Applied Catalysis A: General, 2002. **223**(1-2): p. 121-128.

51. Mao, D., W. Yang, J. Xia, B. Zhang, Q. Song, and Q. Chen, *Highly effective hybrid catalyst for the direct synthesis of dimethyl ether from syngas with magnesium oxide-modified HZSM-5 as a dehydration component.* Journal of Catalysis, 2005. **230**(1): p. 140-149.

52. Chen, H., A. Matsumoto, N. Nishimiya, and K. Tsutsumi, *Preparation and characterization of TiO_2 incorporated Y-zeolite.* Colloids and Surfaces A: Physicochemical and Engineering Aspects, 1999. **157**(1-3): p. 295-305.

53. Yuranov, I., A. Renken, and L. Kiwi-Minsker, *Zeolite/sintered metal fibers composites as effective structured catalysts.* Applied Catalysis A: General, 2005. **281**(1-2): p. 55-60.

54. Das, S.K. and P.K. Dutta, *Synthesis and characterization of a ruthenium oxide-zeolite Y catalyst for photochemical oxidation of water to dioxygen.* Microporous and Mesoporous Materials, 1998. **22**(1-3): p. 475-483.

55. Ramamurthy, V., *Photochemical and photophysical studies within zeolites.* Chimia, 1992. **46**(9): p. 359-376.

56. Ramamurthy, V. and J.V. Caspar, *Photophysical studies of organic-molecules included within zeolites.* Molecular Crystals and Liquid Crystals, 1992. **211**: p. 211-226.

57. Ramamurthy, V., D.F. Eaton, and J.V. Caspar, *Photochemical and photophysical studies of organic-molecules included within zeolites.* Accounts of Chemical Research, 1992. **25**(7): p. 299-307.

58. Ramamurthy, V., J. Shailaja, L.S. Kaanumalle, R.B. Sunoj, and J. Chandrasekhar, *Controlling chemistry with cations: Photochemistry within zeolites.* Chemical Communications, 2003(16): p. 1987-1999.

59. Ramamurthy, V. and N.J. Turro, *Photochemistry of organic-molecules within zeolites - role of cations.* Journal of Inclusion Phenomena and Molecular Recognition in Chemistry, 1995. **21**(1-4): p. 239-282.

60. Mori, K., K. Kagohara, and H. Yamashita, *Synthesis of Tris(2,2'-bipyridine)iron(II) complexes in zeolite Y cages: Influence of exchanged alkali metal cations on physicochemical properties and catalytic activity.* The Journal of Physical Chemistry C, 2008. **112**(7): p. 2593-2600.

61. Ozin, G.A. and S. Ozkar, *Zeolates: a coordination chemistry view of metal-ligand bonding in zeolite guest-host inclusion compounds.* Chemistry of Materials, 1992. **4**(3): p. 511-521.

62. Grubert, G., M. Wark, N.I. Jaeger, G. Schulz-Ekloff, and O.P. Tkachenko, *Reduction kinetics of zeolite-hosted mono- and polynuclear titanium oxide species followed by UV/Vis diffuse reflectance spectroscopy: Influence of location and coordination.* The Journal of Physical Chemistry B, 1998. **102**(10): p. 1665-1671.

63. Jeong, U., X.W. Teng, Y. Wang, H. Yang, and Y.N. Xia, *Superparamagnetic colloids: Controlled synthesis and niche applications.* Advanced Materials, 2007. **19**(1): p. 33-60.

64. Tartaj, P., M.D. Morales, S. Veintemillas-Verdaguer, T. Gonzalez-Carreno, and C.J. Serna, *The preparation of magnetic nanoparticles for applications in biomedicine.* Journal of Physics D-Applied Physics, 2003. **36**(13): p. R182-R197.

65. Weitkamp, J., *Zeolites and catalysis.* Solid State Ionics, 2000. **131**(1-2): p. 175-188.

66. Hyeon, T., *Chemical synthesis of magnetic nanoparticles.* Chemical Communications, 2003(8): p. 927-934.

67. Lian, S.Y., E. Wang, Z.H. Kang, Y.P. Bai, L. Gao, M. Jiang, C.W. Hu, and L. Xu, *Synthesis of magnetite nanorods and porous hematite nanorods.* Solid State Communications, 2004. **129**(8): p. 485-490.

68. Pregelj, M., P. Umek, B. Drolc, B. Jancar, Z. Jaglicic, R. Dominko, and D. Arcon, *Synthesis, structure, and magnetic properties of iron-oxide nanowires.* Journal of Materials Research, 2006. **21**(11): p. 2955-2962.

69. Tavakoli, A., M. Sohrabi, and A. Kargari, *A review of methods for synthesis of nanostructured metals with emphasis on iron compounds.* Chemical Papers, 2007. **61**(3): p. 151-170.

70. Teja, A.S. and L.J. Holm, *Production of magnetic oxide nanoparticles*, in *Supercritical fluid technology in materials science and engineering: Synthesis, properties, and applications*, Y.-P. Sun, Editor. 2002, Elsevier. p. 327-349.

71. Xu, C. and A.S. Teja, *Supercritical water synthesis and deposition of iron oxide (α-Fe_2O_3) nanoparticles in activated carbon.* Journal of Supercritical Fluids, 2006. **39**(1): p. 135-141.

72. Zheng, Y.H., Y. Cheng, F. Bao, and Y.S. Wang, *Synthesis and magnetic properties of Fe_3O_4 nanoparticles.* Materials Research Bulletin, 2006. **41**(3): p. 525-529.

73. Zhu, H.L., D.R. Yang, and L.M. Zhu, *Hydrothermal growth and characterization of magnetite (Fe_3O_4) thin films.* Surface & Coatings Technology, 2007. **201**(12): p. 5870-5874.

74. Pierson, H.O., *Handbook of chemical vapor deposition: Principles, technology, and applications* 1999: William Andrew Inc.

75. Chang, W., G. Skandan, S.C. Danforth, B.H. Kear, and H. Hahn, *Chemical vapor processing and applications for nanostructured ceramic powders and whiskers.* Nanostructured Materials, 1994. **4**(5): p. 507-520.

76. Yoo, J.S., *Selective gas-phase oxidation at oxide nanoparticles on microporous materials.* Catalysis Today, 1998. **41**(4): p. 409-432.

77. Ito, T., H. Kanai, T. Nakai, and S. Imamura, *State of titanium in Ti-containing silica and silicalite catalysts in relation to their oxidation activity.* Reaction Kinetics and Catalysis Letters, 1994. **52**(2): p. 421-428.

78. Dossi, C., R. Psaro, A. Bartsch, A. Fusi, L. Sordelli, R. Ugo, M. Bellatreccia, R. Zanoni, and G. Vlaic, *Chemical-vapor-deposition of platinum hexafluoroacetylacetonate inside KL zeolite - A new route to nonacidic platinum-in-zeolite catalysts.* Journal of Catalysis, 1994. **145**(2): p. 377-383.

79. Dossi, C., R. Psaro, A. Bartsch, E. Brivio, A. Galasco, and P. Losi, *Organometallics-chemical vapor-deposition - A new technique for the preparation of nonacidic, zeolite-supported Pd and Pt catalysts.* Catalysis Today, 1993. **17**(3): p. 527-535.

80. Kwak, B.S. and W.M.H. Sachtler, *Effect of Ga/proton balance in Ga/HZSM-5 catalysts on C_3 conversion to aromatics.* Journal of Catalysis, 1994. **145**(2): p. 456-463.

81. Okamoto, Y., T. Imanaka, K. Asakura, and Y. Iwasawa, *Structure and electronic state of molybdenum subcarbonyl species encaged in zeolite.* The Journal of Physical Chemistry, 1991. **95**(9): p. 3700-3705.

82. Okamoto, Y., A. Maezawa, H. Kane, I. Mitsushima, and T. Imanaka, *Thermal stabilities of hexacarbonyl and subcarbonyls of molybdenum encapsulated in NaY and NaX zeolites.* Journal of the Chemical Society-Faraday Transactions I, 1988. **84**: p. 851-863.

83. Brenner, A. and R.L. Burwell, *Reversibility in the formation of stoichiometric surface molybdenum carbonyls on alumina.* Journal of the American Chemical Society, 1975. **97**(9): p. 2565-2566.

84. Battiston, A.A., J.H. Bitter, F.M.F. de Groot, A.R. Overweg, O. Stephan, J.A. van Bokhoven, P.J. Kooyman, C. van der Spek, G. Vanko, and D.C. Koningsberger, *Evolution of Fe species during the synthesis of over-exchanged Fe/ZSM5 obtained by chemical vapor deposition of $FeCl_3$.* Journal of Catalysis, 2003. **213**(2): p. 251-271.

85. Seidel, A., F. Rittner, and B. Boddenberg, *Chemical vapor deposition of zinc in zeolite HY.* Journal of Physical Chemistry B, 1998. **102**(37): p. 7176-7182.

86. Hong, S.B., E. Mielczarski, and M.E. Davis, *Aromatization of n-hexane by platinum-containing molecular sieves I. Catalyst preparation by the vapor phase impregnation method.* Journal of Catalysis, 1992. **134**(1): p. 349-358.

87. Bond, G.C. and D.T. Thompson, *Catalysis by gold.* Catalysis Reviews: Science and Engineering, 1999. **41**(3): p. 319 - 388.

88. Okumura, M., K. Tanaka, A. Ueda, and M. Haruta, *The reactivities of dimethylgold(III) β-diketone on the surface of TiO_2 : A novel preparation method for Au catalysts.* Solid State Ionics, 1997. **95**(1-2): p. 143-149.

89. Dossi, C., R. Psaro, A. Bartsch, E. Brivio, A. Galasco, and P. Losi, *Organometallics-chemical vapor deposition: A new technique for the preparation of non-acidic, zeolitesupported Pd and Pt catalysts.* Catalysis Today, 1993. **17**(3): p. 527-535.

90. Dossi, C., R. Psaro, R. Ugo, Z.C. Zhang, and W.M.H. Sachtler, *Non-acidic Pd/Y zeolite catalysts from organopalladium precursors: Preparation and catalytic activity in MCP reforming.* Journal of Catalysis, 1994. **149**(1): p. 92-99.

91. Sordelli, L., G. Martra, R. Psaro, C. Dossi, and S. Coluccia, *Intrazeolite Pd clusters: Particle location.* Topics in Catalysis, 1999. **8**(3): p. 237-242.

92. Serp, P., R. Feurer, R. Morancho, and P. Kalck, *A versatile one-step method for the preparation of highly dispersed metal supported catalysts.* Journal of Molecular Catalysis A: Chemical, 1995. **101**(2): p. L107-L110.

93. Serp, P., R. Feurer, R. Morancho, and P. Kalck, *One-step preparation of highly dispersed supported rhodium catalysts by low-temperature organometallic chemical-vapor-deposition.* Journal of Catalysis, 1995. **157**(2): p. 294-300.

94. Serp, P., L. Chateau, R. Feurer, A. Kiennemann, and P. Kalck, *Rhodium-catalyzed hydrocarbonylation of acetic acid into higher acids.* Journal of Molecular Catalysis A: Chemical, 1998. **136**(3): p. 269-278.

95. Miura, H., *Preparation of supported bimetallic catalysts by means of selective deposition using mobile metal compounds as precursors.* Catalysis Today, 1996. **28**(3): p. 215-221.

96. Miura, H., H. Taguchi, K. Sugiyama, T. Matsuda, and R.D. Gonzalez, *The control of metal precursor mobilities as a variable in the preparation of supported Pt-Ru bimetallic clusters: The use of ruthenocene.* Journal of Catalysis, 1990. **124**(1): p. 194-203.

97. Serp, P., P. Kalck, and R. Feurer, *Chemical vapor deposition methods for the controlled preparation of supported catalytic materials.* Chemical Reviews, 2002. **102**(9): p. 3085-3128.

98. Lam, U.T., R. Mammucari, K. Suzuki, and N.R. Foster, *Processing of iron oxide nanoparticles by supercritical fluids.* Industrial & Engineering Chemistry Research, 2008. **47**(3): p. 599-614.

99. Tadic, M., D. Markovic, V. Spasojevic, V. Kusigerski, M. Remskar, J. Pirnat, and Z. Jaglicic, *Synthesis and magnetic properties of concentrated α-Fe_2O_3 nanoparticles in a silica matrix.* Journal of Alloys and Compounds, 2007. **441**(1-2): p. 291-296.

100. Xu, Z.Z., C.C. Wang, W.L. Yang, and S.K. Fu, *Synthesis of superparamagnetic Fe_3O_4/SiO_2 composite particles via sol-gel process based on inverse miniemulsion.* Journal of Materials Science, 2005. **40**(17): p. 4667-4669.

101. Deng, Y.H., C.C. Wang, J.H. Hu, W.L. Yang, and S.K. Fu, *Investigation of formation of silica-coated magnetite nanoparticles via sol-gel approach.* Colloids and Surfaces A-Physicochemical and Engineering Aspects, 2005. **262**(1-3): p. 87-93.

102. Lam, U.T., R. Mammucari, K. Suzuki, and N.R. Foster, *Processing of iron oxide nanoparticles by supercritical fluids.* Industrial & Engineering Chemistry Research 2008. **47**(3): p. 599-614.

103. Wang, C.T. and R.J. Willey, *Oxidation of methanol over iron oxide based aerogels in supercritical CO_2.* Journal of Non-Crystalline Solids, 1998. **225**(1): p. 173-177.

104. Wang, C.-T. and S.-H. Ro, *Nanocluster iron oxide-silica aerogel catalysts for methanol partial oxidation.* Applied Catalysis A: General, 2005. **285**(1-2): p. 196-204.

105. Yamashita, H., S. Kawasaki, Y. Ichihashi, M. Harada, M. Takeuchi, M. Anpo, G. Stewart, M.A. Fox, C. Louis, and M. Che, *Characterization of titanium-silicon binary oxide catalysts prepared by the sol-gel method and their photocatalytic reactivity for the liquid-phase oxidation of 1-octanol.* The Journal of Physical Chemistry B, 1998. **102**(30): p. 5870-5875.

106. Hwang, K.S., Y.S. Jeon, K.O. Jeon, and B.H. Kim, *Transparent (1-x)TiO_2-xFe_2O_3 (x=0, 5, 10, 15 and 20 mol %) thin films prepared by sol-gel process.* Optica Applicata, 2005. **35**(2): p. 191-199.

107. Liu, H.R., Z.L. Liu, Q. Liu, and K.L. Yao, *Ferroelectric properties of $BiFeO_3$ films grown by sol-gel process.* Thin Solid Films, 2006. **500**(1-2): p. 105-109.

108. Ismail, A.A., *Synthesis and characterization of Y_2O_3/Fe_2O_3/TiO_2 nanoparticles by sol-gel method.* Applied Catalysis B: Environmental, 2005. **58**(1-2): p. 115-121.

109. Lakeman, C.D.E. and D.A. Payne, *Sol-gel processing of electrical and magnetic ceramics.* Materials Chemistry and Physics, 1994. **38**(4): p. 305-324.

110. An, S.Y., I.B. Shim, and C.S. Kim, *Synthesis and magnetic properties of $LiFe_5O_8$ powders by a sol-gel process.* Journal of Magnetism and Magnetic Materials, 2005. **290**: p. 1551-1554.

111. Willey, R.J., S.A. Oliver, G. Oliveri, and G. Busca, *Chemistry and structure of mixed magnesium ferric-oxide aerogels.* Journal of Materials Research, 1993. **8**(6): p. 1418-1427.

112. Yamaguchi, K., T. Fujii, S. Kuranouchi, Y. Yamanobe, and A. Ueno, *Magnetic-properties of iron-boron-oxide and iron-phosphor-oxide glasses prepared by sol-gel method.* IEEE Transactions on Magnetics, 1989. **25**(5): p. 3321-3323.

113. Zhang, R.J., J.J. Huang, H.T. Zhao, Z.Q. Sun, and Y. Wang, *Sol-gel auto-combustion synthesis of zinc ferrite for moderate temperature desulfurization.* Energy & Fuels, 2007. **21**(5): p. 2682-2687.

114. Liu, M., H. Li, L. Xiao, W. Yu, Y. Lu, and Z. Zhao, *XRD and Mössbauer spectroscopy investigation of Fe_2O_3-Al_2O_3 nano-composite.* Journal of Magnetism and Magnetic Materials, 2005. **294**(3): p. 294-297.

115. Shu, S., *Engineering the performance of mixed matrix membranes for gas separations*. 2007, Georgia Institute of Technology: United States -- Georgia. p. 251.

116. Warnken, M., K. Lazar, and M. Wark, *Redox behaviour of SnO_2 nanoparticles encapsulated in the pores of zeolites towards reductive gas atmospheres studied by in situ*

diffuse reflectance UV/Vis and Mossbauer spectroscopy. Physical Chemistry Chemical Physics, 2001. **3**(10): p. 1870-1876.

117. Salama, T.M., I.O. Ali, and H.A. Gumaa, *Synthesis and characterization of Cu(I)-salen complex immobilized aluminosilicate MCM-41.* Microporous and Mesoporous Materials, 2008. **113**(1-3): p. 90-98.

118. Coughlan, B. and M.A. Keane, *The effects of the environment on the growth of nickel metal particles supported on a range of Y zeolites prepared by ion exchange and impregnation.* Zeolites, 1991. **11**(1): p. 2-11.

119. Yamashita, H., Y. Ichihashi, M. Anpo, M. Hashimoto, C. Louis, and M. Che, *Photocatalytic decomposition of NO at 275 K on titanium oxides included within Y-Zeolite cavities: The structure and role of the active sites.* The Journal of Physical Chemistry, 1996. **100**(40): p. 16041-16044.

120. Kazansky, V.B., V.Y. Borovkov, A.I. Serikh, R.A. van Santen, and B.G. Anderson, *Nature of the sites of dissociative adsorption of dihydrogen and light paraffins in ZnHZSM-5 zeolite prepared by incipient wetness impregnation.* Catalysis Letters, 2000. **66**(1): p. 39-47.

121. Lihitkar, N.B., M.K. Abyaneh, V. Samuel, R. Pasricha, S.W. Gosavi, and S.K. Kulkarni, *Titania nanoparticles synthesis in mesoporous molecular sieve MCM-41.* Journal of Colloid and Interface Science, 2007. **314**(1): p. 310-316.

122. Nam, S.-S., H. Kim, G. Kishan, M.-J. Choi, and K.-W. Lee, *Catalytic conversion of carbon dioxide into hydrocarbons over iron supported on alkali ion-exchanged Y-zeolite catalysts.* Applied Catalysis A: General, 1999. **179**(1-2): p. 155-163.

123. Ismagilov, Z.R., S.A. Yashnik, V.F. Anufrienko, T.V. Larina, N.T. Vasenin, N.N. Bulgakov, S.V. Vosel, and L.T. Tsykoza, *Linear nanoscale clusters of CuO in Cu-ZSM-5 catalysts.* Applied Surface Science, 2004. **226**(1-3): p. 88-93.

124. Guo, X.W., X.S. Wang, J.P. Shen, L. Sun, and C.S. Song, *Methylation of 4-methylbiphenyl with methanol over metal oxide-modified HZSM-5 zeolite catalysts.* Chinese Journal of Catalysis, 2003. **24**(5): p. 333-337.

125. Li, W., L. Luo, H. Yamashita, J.A. Labinger, and M.E. Davis, *Synthesis and characterization of zeolite beta containing oxide clusters of antimony and vanadium.* Microporous and Mesoporous Materials, 2000. **37**(1-2): p. 57-65.

126. Gies, H., S. Grabowski, M. Bandyopadhyay, W. Grunert, O.P. Tkachenko, K.V. Klementiev, and A. Birkner, *Synthesis and characterization of silica MCM-48 as carrier of size-confined nanocrystalline metal oxides particles inside the pore system.* Microporous and Mesoporous Materials, 2003. **60**(1-3): p. 31-42.

127. Anpo, M., H. Yamashita, Y. Ichihashi, Y. Fujii, and M. Honda, *Photocatalytic reduction of CO_2 with H_2O on titanium oxides anchored within micropores of zeolites: Effects of the structure of the active sites and the addition of Pt.* The Journal of Physical Chemistry B, 1997. **101**(14): p. 2632-2636.

128. Campanati, M., G. Fornasari, and A. Vaccari, *Fundamentals in the preparation of heterogeneous catalysts.* Catalysis Today, 2003. **77**(4): p. 299-314.

129. *Metal oxides : Chemistry and applications*. Chemical industries ;, ed. J.L.G. Fierro. 2006, Boca Raton, FL :: CRC Taylor & Francis.

130. Kinger, G., A. Lugstein, R. Swagera, M. Ebel, A. Jentys, and H. Vinek, *Comparison of impregnation, liquid- and solid-state ion exchange procedures for the incorporation of nickel in HMFI, HMOR and HBEA: Activity and selectivity in n-nonane hydroconversion.* Microporous and Mesoporous Materials, 2000. **39**(1-2): p. 307-317.

131. Xu, C., *Continuous and batch hydrothermal synthesis of metal oxide nanoparticles and metal oxide-activated carbon nanocomposites*. 2006, Georgia Institute of Technology: United States -- Georgia. p. 258.

132. *Nanowires and nanobelts : materials, properties, and devices*, ed. Z.L. Wang. 2003, Boston :: Kluwer Academic Publishers.

133. *Chemical processing of ceramics*. 2nd ed. / ed. Materials engineering ;, ed. B.I. Lee and S. Komarneni. 2005, Boca Raton :: Taylor & Francis.

134. Fan, W., S. Sun, X. Song, W. Zhang, H. Yu, X. Tan, and G. Cao, *Controlled synthesis of single-crystalline $Mg(OH)_2$ nanotubes and nanorods via a solvothermal process.* Journal of Solid State Chemistry, 2004. **177**(7): p. 2329-2338.

135. Chaianansutcharit, S., O. Mekasuwandumrong, and P. Praserthdam, *Synthesis of Fe_2O_3 nanoparticles in different reaction media.* Ceramics International, 2007. **33**(4): p. 697-699.

136. Dubois, T. and G. Demazeau, *Preparation of Fe_3O_4 fine particles through a solvothermal process.* Materials Letters, 1994. **19**(1-2): p. 38-47.

137. Tian, D., W. Yan, Z. Wang, Y. Wang, Z. Li, J. Yu, and R. Xu, *Core-Shell composite of Ti-/Cr-AFI molecular sieve via solvothermal epitaxial growth.* Crystal Growth & Design, 2009. **9**(3): p. 1411-1414.

138. Kominami, H., K. Yukishita, T. Kimura, M. Matsubara, K. Hashimoto, Y. Kera, and B. Ohtani, *Direct solvothermal formation of nanocrystalline TiO_2 on porous SiO_2 adsorbent and photocatalytic removal of nitrogen oxides in air over TiO_2–SiO_2 composites.* Topics in Catalysis, 2008. **47**(3): p. 155-161.

139. Chen, S.-J., X.-T. Chen, Z. Xue, L.-H. Li, and X.-Z. You, *Solvothermal preparation of Cu_2O crystalline particles.* Journal of Crystal Growth, 2002. **246**(1-2): p. 169-175.

140. Hao, Y.L. and A.S. Teja, *Continuous hydrothermal crystallization of α-Fe_2O_3 and Co_3O_4 nanoparticles.* Journal of Materials Research, 2003. **18**(2): p. 415-422.

141. Eckert, C.A., B.L. Knutson, and P.G. Debenedetti, *Supercritical fluids as solvents for chemical and materials processing.* Nature, 1996. **383**(6598): p. 313-318.

142. Sue, K., M. Suzuki, K. Arai, T. Ohashi, H. Ura, K. Matsui, Y. Hakuta, H. Hayashi, M. Watanabe, and T. Hiaki, *Size-controlled synthesis of metal oxide nanoparticles with a flow-through supercritical water method.* Green Chemistry, 2006. **8**(7): p. 634-638.

143. Cabanas, A., J.A. Darr, E. Lester, and M. Poliakoff, *Continuous hydrothermal synthesis of inorganic materials in a near-critical water flow reactor; the one-step synthesis of*

nano-particulate $Ce_{1-x}Zr_xO_2$ (x=0-1) solid solutions. Journal of Materials Chemistry, 2001. **11**(2): p. 561-568.

144. Burda, C., X. Chen, R. Narayanan, and M.A. El-Sayed, *Chemistry and properties of nanocrystals of different shapes.* Chemical Reviews, 2005. **105**(4): p. 1025-1102.

145. Shaw, R.W., T.B. Brill, A.A. Clifford, C.A. Eckert, and E.U. Franck, *Supercritical water - A medium for chemistry.* Chemical & Engineering News, 1991. **69**(51): p. 26-39.

146. Sue, K., K. Kimura, and K. Arai, *Hydrothermal synthesis of ZnO nanocrystals using microreactor.* Materials Letters, 2004. **58**(25): p. 3229-3231.

147. Dou, Q.S., H. Zhang, J.B. Wu, and D.R. Yang, *Synthesis and characterization of Fe_2O_3 and FeOOH nanostructures prepared by ethylene glycol assisted hydrothermal process.* Journal of Inorganic Materials, 2007. **22**(2): p. 213-218.

148. Giri, S., S. Samanta, S. Maji, S. Ganguli, and A. Bhaumik, *Magnetic properties of α-Fe_2O_3 nanoparticle synthesized by a new hydrothermal method.* Journal of Magnetism and Magnetic Materials, 2005. **285**(1-2): p. 296-302.

149. Sorescu, M., L. Diamandescu, and D. Tarabasanu-Mihaila, *α-Fe_2O_3-In_2O_3 mixed oxide nanoparticles synthesized under hydrothermal supercritical conditions.* Journal of Physics and Chemistry of Solids, 2004. **65**(10): p. 1719-1725.

150. Wang, X., X.Y. Chen, L.S. Gao, H.G. Zheng, M.R. Ji, C.M. Tang, T. Shen, and Z.D. Zhang, *Synthesis of β-FeOOH and α-Fe_2O_3 nanorods and electrochemical properties of β-FeOOH.* Journal of Materials Chemistry, 2004. **14**(5): p. 905-907.

151. Yoshimura, M. and S. Somiya, *Hydrothermal synthesis of crystallized nano-particles of rare earth-doped zirconia and hafnia.* Materials Chemistry and Physics, 1999. **61**(1): p. 1-8.

152. Xu, C., *Continuous and batch hydrothermal synthesis of metal oxide nanoparticles and metal oxide-activated carbon nanocomposites. PhD Thesis*. 2006, Georgia Institute of Technology: United States -- Georgia.

153. Zhang, J., M. Minagawa, T. Ayusawa, S. Natarajan, H. Yamashita, M. Matsuoka, and M. Anpo, *In Situ Investigation of the Photocatalytic Decomposition of NO on the Ti-HMS under Flow and Closed Reaction Systems.* The Journal of Physical Chemistry B, 2000. **104**(48): p. 11501-11505.

154. Ikeue, K., H. Yamashita, M. Anpo, and T. Takewaki, *Photocatalytic reduction of CO_2 with H_2O on Ti-β zeolite photocatalysts:Effect of the hydrophobic and hydrophilic properties.* The Journal of Physical Chemistry B, 2001. **105**(35): p. 8350-8355.

155. Yamashita, H., K. Yoshizawa, M. Ariyuki, S. Higashimoto, M. Che, and M. Anpo, *Photocatalytic reactions on chromium containing mesoporous silica molecular sieves (Cr-HMS) under visible light irradiation: Decomposition of NO and partial oxidation of propane.* Chemical Communications, 2001(5): p. 435-436.

156. Yamashita, H., K. Yoshizawa, M. Ariyuki, S. Higashimoto, and M. Anpo, *Photocatalytic ethylene polymerization over chromium containing mesoporous molecular sieves*, in *Nanoporous Materials Iii*, A. Sayari and M. Jaroniec, Editors. 2002. p. 495-502.

157. Yamashita, H. and M. Anpo, *Local structures and photocatalytic reactivities of the titanium oxide and chromium oxide species incorporated within micro- and mesoporous zeolite materials: XAFS and photoluminescence studies.* Current Opinion in Solid State and Materials Science, 2003. **7**(6): p. 471-481.

158. Chorkendorff, I., *Concepts of modern catalysis and kinetics*, ed. J.W. Niemantsverdriet. 2003, Weinheim [Germany] :: Wiley-VCH.

159. Regalbuto, J., ed. *Catalyst preparation : Science and engineering*. 2007, CRC Press/Taylor & Francis: Boca Raton.

160. Perego, C. and P. Villa, *Catalyst preparation methods.* Catalysis Today, 1997. **34**(3-4): p. 281-305.

161. Li, G., J. Edwards, A.F. Carley, and G.J. Hutchings, *Direct synthesis of hydrogen peroxide from H_2 and O_2 and in situ oxidation using zeolite-supported catalysts.* Catalysis Communications, 2007. **8**(3): p. 247-250.

162. Okumura, K., K. Yoshino, K. Kato, and M. Niwa, *Quick XAFS Studies on the Y-Type Zeolite Supported Au Catalysts for CO-O_2 Reaction.* The Journal of Physical Chemistry B, 2005. **109**(25): p. 12380-12386.

163. Bandyopadhyay, M., O. Korsak, M.W.E. van den Berg, W. Grunert, A. Birkner, W. Li, F. Schuth, and H. Gies, *Gold nano-particles stabilized in mesoporous MCM-48 as active CO-oxidation catalyst.* Microporous and Mesoporous Materials, 2006. **89**(1-3): p. 158-163.

164. Nares, R., J. Ramirez, A. Gutierrez-Alejandre, C. Louis, and T. Klimova, *Ni/HB-zeolite catalysts prepared by deposition- precipitation.* The Journal of Physical Chemistry B, 2002. **106**(51): p. 13287-13293.

165. Burattin, P., M. Che, and C. Louis, *Ni/SiO_2 materials prepared by deposition-precipitation: Influence of the reduction conditions and mechanism of formation of metal particles.* The Journal of Physical Chemistry B, 2000. **104**(45): p. 10482-10489.

166. Stangland, E.E., B. Taylor, R.P. Andres, and W.N. Delgass, *Direct vapor phase propylene epoxidation over deposition-precipitation gold-titania catalysts in the presence of H_2/O_2: Effects of support, neutralizing agent, and pretreatment.* The Journal of Physical Chemistry B, 2004. **109**(6): p. 2321-2330.

167. Gurbani, A., J.L. Ayastuy, M.P. Gonzalez-Marcos, J.E. Herrero, J.M. Guil, and M.A. Gutierrrez-Ortiz, *Comparative study of CuO-CeO_2 catalysts prepared by wet impregnation and deposition-precipitation.* International Journal of Hydrogen Energy, 2009. **34**(1): p. 547-553.

168. Yu, W.Y., C.P. Yang, J.N. Lin, C.N. Kuo, and B.Z. Wan, *Preparation of Au/TiO_2 for catalytic preferential oxidation of CO under a hydrogen rich atmosphere at around room temperature.* Chemical Communications, 2005(3): p. 354-356.

CHAPTER 3

SYNTHESIS AND CHARACTERIZATION OF $Mg(OH)_2$/ ZEOLITE 4A NANOCOMPOSITES

3-1 Introduction

This chapter describes a simple deposition-precipitation method to assemble magnesium hydroxide nanostructures on zeolite 4A at ambient conditions. The deposition – precipitation method is similar to the hydrothermal method in which the metal hydroxides/ oxides are precipitated from their metal precursors by tuning their solubility. However, solubility change occurs by the addition of alkali and not by heat addition. In the deposition – precipitation process, small crystallites of metal hydroxide are precipitated by heterogeneous nucleation at the zeolite surface where they interact with the surface and assemble into nanostructures [1]. A well-dispersed and homogeneous active phase is reached when the OH^- groups of the support (for example, the silanols of silica) interact directly with the ions present in the solution, thereby also determining the nature of the formed phase [2-4]. In principle, the deposition- precipitation method enables the deposition of a controlled amount of metal precursor up to high loading [5, 6].

Previously, Teja and co-workers [7-13] investigated the precipitation of metal oxides and mixed oxides such as Fe_2O_3, Co_3O_4, $LiFePO_4$, and $CoFe_2O_4$ via hydrothermal synthesis at sub- supercritical water conditions and found that the solubilities and morphologies of these materials can be tuned by varying the concentration of the precursors, temperature, and pH of the reaction medium. It was found that in general, the

solubility behavior of metals is dependent on the speciation of the metal ions in solution at different pH and hydrolysis of the metal ions [14]. In addition, metal ions that exhibit high positive charge and low ionic radii will result in increased metal-coordinated water interactions with easier proton release and strong tendency to hydrolyze [14]. In some cases, hydrolysis results in the formation of hydroxide networks, which are less soluble than the cations [14].

In the present study, the effects of synthesis parameters such as temperature, reagent concentration, nature of the base, and synthesis time on the size, morphology, and composition of the resulting zeolite nanocomposite were investigated. Based on the studies conducted by Teja and co-workers [7-11, 13, 15], it is hypothesized that the precipitation of $Mg(OH)_2$ would be more favorable with increasing magnesium precursor concentration and temperature because of the increase in the saturation level of magnesium ions in the solution. The nature of the precipitant and its alkalinity are expected to affect the morphology of $Mg(OH)_2$ since $Mg(OH)_2$ can only be precipitated under basic conditions. The use of a strong base should result in rapid nucleation and in the formation of tiny $Mg(OH)_2$ particles. A longer synthesis time would be favorable for self-assembly and crystal growth of the precipitated particles.

The magnesium source in the present study was magnesium chloride. Henrist et al. [16] have reported that there is no morphological difference when other precursors such as magnesium nitrate are used as the magnesium source. However, in the case of magnesium sulphate, agglomerated particles were obtained and these agglomerates were difficult to separate [16]. Thus magnesium chloride was chosen as the magnesium precursor in the present work. A weak base such as ammonium hydroxide and a strong

base such as sodium hydroxide were used as precipitants in order to investigate the effects of the nature of the base on the formation of $Mg(OH)_2$. According to Wulfsberg [17], the predominant magnesium species at low pH is hydrated magnesium ions, whereas at high pH magnesium exists predominantly as $Mg(OH)_2$. Therefore, the formation of magnesium hydroxide is more favorable at basic conditions.

3-2 Literature review

The comprehensive understanding and efficient control of the crystal morphology is of practical important, since various macroscopic properties and practical applications of the crystal materials strongly depend on their morphology and size [18, 19]. In general, the morphology of the crystal is in large extent depends on the intrinsic structure of the crystal, pH, and supersaturation level [19]. Some of the more popularly accepted crystallization theory to predict the crystal habit are the Bravais, Friedel, Donnay, and Harker (BFDH) law [20, 21], the periodic bond chain theory introduced by Hartman and Perdok [21-23], and the diffusion-reaction theory [24].

The BFDH model assumes that the linear growth rate, R_{hkl}, of a given crystal face is inversely proportional to the corresponding interplanar distance, d_{hkl}, after taking into account the extinction conditions of the crystal space group [19, 25]. In other words, the slowest growing faces, and hence most prominent, are those in which the interatomic spacing is the greatest. The BFDH law only makes use of the framework of the crystal lattice and gives no consideration to the atom or bond type or partial charge. Although the BFDH model gives in principle a satisfying description of the morphology of crystals, the drawback of this law is its purely mathematical character [26]. Neither the real crystal

structure, nor the concept of chemical bond, thermodynamics and statistical mechanics of interfaces, and crystal growth mechanisms are taken into account [26].

The BFDH model was refined by Hartman and Perdok by relating the crystal morphology to its internal structure on an energy basis [25]. They identified that chains of strong intermolecular bonds known as periodic bond chains (PBC) govern the crystal morphology [26]. According to the number of PBC inside a slice of thickness, d_{hkl}, the c onlyrystal faces can be classified as (i) F-faces (flat), two or more PBC, (ii) S-faces (stepped), one PBC, or (iii) K-faces (kinked), zero PBC [26].The F-faces have low growth rates due to the existence of a limited number of kink sites, and they grow by lateral extension of the growth layers, whereas the growth of S-faces only needs a unidimensional nucleation is faster than that of F-faces. Finally, the growth rate of the K-faces is the highest because the K-faces have a higher number of kink sites [25]. The growth rate of each faces is related to the attachment energy and small attachment energy translates into low growth velocity [19, 25]. Subsequently, the F-faces with the lowest attachment energy will tend to appear in the crystal morphology more frequently than the S- and K-faces which have higher attachment energy and growth rates [19]. Although the PBC theory predicted some crystal morphology successfully, its main drawback is that it does not account for the environmental factors of crystal growth such as supersaturation [27].

Among the crystal growth theories in the literature, only the diffusion-reaction theory considers the bulk diffusion of the crystallizing species [24]. The diffusion-reaction theory leads to the two-step crystal growth model. In the diffusion step, the building blocks diffuse through a boundary layer between the crystal surface and the bulk

solution to arrive at the crystal face, whereas in the reaction step, the building blocks on the crystal surface integrate into the crystal lattice [27]. These steps can be expressed mathematically as [24]:

$G = K_d(\sigma - \sigma_i)$ bulk diffusion

$G = K_r \sigma_i^r$ surface reaction

where G is the crystal growth rate, σ is the overall supersaturation, σ_i is the interfacial supersaturation, K_d is the mass transfer coefficient, and K_r is the reaction constant. The surface reaction represents one or a combination of the growth steps occurring at the crystal-solution interface, including adsorption, surface diffusion, dehydration, and intergration [24]. Although the diffusion-reaction theory is popularly accepted, it is not easy to use in practice because little is known about the boundary layer [27].

It can be observed from the above discussion that crystallization is a very complex process and there is no single theory to accurately describe it. Therefore in this work some of the concepts from the theories described above will be used to understand the formation of magnesium hydroxide.

3-3 Experimental

3-3-1 *Materials*

Magnesium chloride ($MgCl_2.6H_2O$, ACS reagent), ammonium hydroxide (NH_4OH, 14.8 normality, ACS reagent), ammonium chloride (NH_4Cl, ACS reagent), and sodium hydroxide (NaOH, ACS reagent) were purchased from Fischer Scientific (NJ, USA). ADVERA 401P hydrated sodium zeolite 4A with a characteristic 3 – 6 μm cubic

form was purchased from PQ Corporation (PA, USA). Silicon oxide and aluminum oxide particles were purchased from Nanomaterials & Amorphous Materials Inc. (TX, USA) and Electron Microscopy Sciences (PA, USA) respectively. The average primary particle size was 3 μm as reported by the vendors. Deionized water was made in the lab and all materials were used without further purification. Cellulose nitrate membrane filters of pore size 0.2 μm were purchased from Whatman (NJ, USA).

3-3-2 *Procedure*

Magnesium chloride solution of known concentration was prepared by adding deionized water to a known mass of $MgCl_2.6H_2O$ salt to make 20 mL of solution. 60 mL of NH_4OH solution (same concentration as $MgCl_2.6H_2O$) was prepared by diluting appropriate amount of the concentrated NH_4OH (14.8 normality). Experiments were then carried out as follows: (1) 0.2 g of zeolite 4A were added to 20 mL of the magnesium chloride solution of known concentration in a beaker, (2) 60 mL of ammonium hydroxide / NaOH / DI water solution were titrated into the above mixture while stirring, (3) the mixture was allowed to sit at ambient conditions for a specified time, after which its pH of the solution was measured. The experiment was also carried out at 673 K and 623 K in a 250 mL stainless steel autoclave (Parr Instrument Co., IL, USA, Model 4576) equipped with a magnetic stirrer. Conditions of all experiments are summarized in Table 3.1. At the conclusion of each experiment, the zeolite particles were collected via vacuum filtration through a cellulose nitrate membrane filter of pore size 0.2 μm. The collected particles were washed with an excess amount of deionized water and dried overnight in a vacuum oven at 323 K

3-3-3 *Characterization techniques*

A small sample of the dried particles from each experiment was examined by scanning electron microscopy (SEM), Fourier Transform Infrared (FT-IR), and powder X-ray diffraction (XRD). The SEM consisted of a LEO 1530 FEG field-emission instrument (Carl Zeiss SMT Inc., Germany) equipped with an energy dispersive X-ray spectroscopy (EDS) detector. Fourier Transform Infra Red (FT-IR) analysis was used for identification of the final products using a Bruker IFS 66v/S spectrometer (Bruker Corporation, USA). The sample was finely ground and diluted to 3 wt % with KBr powder before being pressed into a translucent pellet with a hand press. All IR measurements were carried out at room temperature under vacuum using a repetition of 50 scans at a resolution of 4 cm^{-1} in the absorbance mode. Powder X-ray diffraction (XRD) patterns were obtained on a Phillips X'pert diffractometer (PANalytical Inc, USA) equipped with X'celerator using Cu Kα radiation.

Table 3-1 Summary of experimental conditions for the preparation of magnesium hydroxide – zeolite 4A nanocomposites. Equimolar magnesium chloride and ammonium hydroxide solutions were added in a 1: 3 volume ratio

Expt. No	Conc. of $MgCl_2$ (M)	Conc. of base (M)	Temperature	Synthesis time	pH
A1	0.01 M	0.01 M NH_4OH	298 K	24 h	10.81 ± 0.30
A2	0.04 M	0.04 M NH_4OH	298 K	24 h	10.17 ± 0.28
A3	0.07 M	0.07 M NH_4OH	298 K	24 h	10.15 ± 0.25
A4	0.1 M	0.1 M NH_4OH	298 K	24 h	10.06 ± 0.22
A5	0.01 M	0.01 M NH_4OH	298 K	48 h	10.73 ± 0.28
A6	0.04 M	0.04 M NH_4OH	298 K	48 h	10.01 ± 0.26
A7	0.07 M	0.07 M NH_4OH	298 K	48 h	9.96 ± 0.24
A8	0.1 M	0.1 M NH_4OH	298 K	48 h	9.92 ± 0.21
A9	0.01 M	0.01 M NH_4OH	298 K	72 h	10.36 ± 0.32
A10	0.04 M	0.04 M NH_4OH	298 K	72 h	9.89 ± 0.33
A11	0.07 M	0.07 M NH_4OH	298 K	72 h	9.82 ± 0.27
A12	0.1 M	0.1 M NH_4OH	298 K	72 h	9.80 ± 0.23
B1	0.01 M	DI water	298 K	72 h	9.25 ± 0.22
B2	0.04 M	DI water	298 K	72 h	8.27 ± 0.21
B3	0.07 M	DI water	298 K	72 h	8.20 ± 0.16
B4	0.1 M	DI water	298 K	72 h	8.12 ± 0.20
C1	0.04 M	0.04 M NaOH	298 K	72 h	11.25 ± 0.3
D1	0.05 M	0.05 M NH_4OH	673 K	2 h	-
D2	0.05 M	0.05 M NH_4OH	623 K	2 h	-

3-4 Results

3-4-1 *Identification and characterization of surface nanostructures*

3-4-1-1 ***Scanning Electron Microscopy (SEM)***

Figure 3.1 displays the surface morphology of zeolites obtained at different magnesium ion concentrations and pH at a synthesis time of 72 h. Petal-like structures were obtained at pH between 9-11 whereas tiny particles were obtained at pH > 11. No deposition was observed at high concentration of Mg^{2+} ions and low pH. However, nanostructures were deposited on the zeolite at high pH even though the concentration of Mg^{2+} ions was low. At high pH, the amount of deposited material increased with increasing concentration of Mg^{2+} ions. The effects of magnesium ion concentration and basicity on the size, shape, and morphology of the surface nanostructures are discussed in detail in the following section.

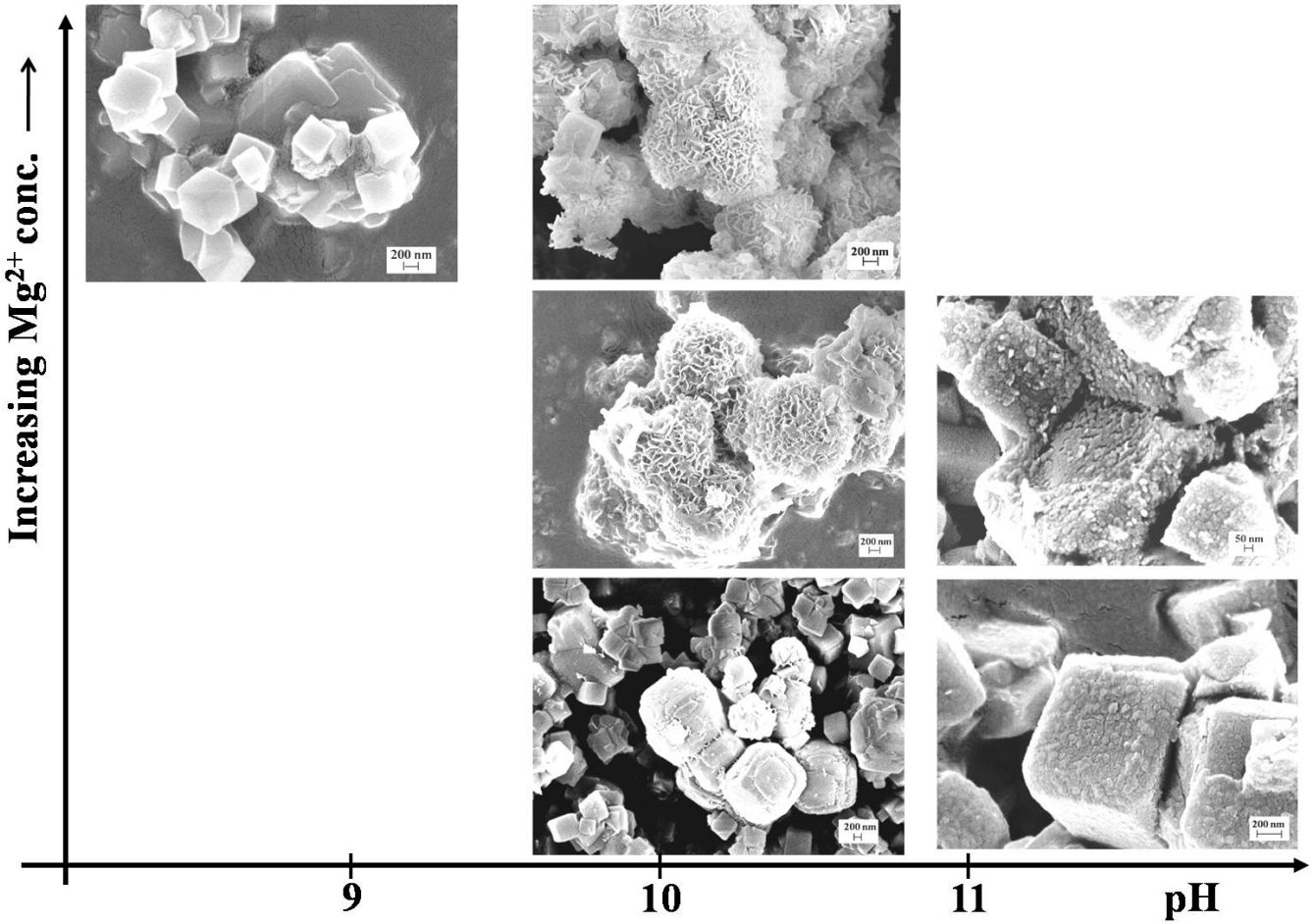

Fig. 3.1 Change in the morphology and deposition of surface nanostructures with respect to pH and magnesium ion concentration.

3-4-1-2 ***Energy Dispersive X-ray Spectroscopy (EDS)***

Energy dispersive X-ray spectroscopy was used to determine the elemental composition of the surface material deposited on the zeolite surface. The EDS used was connected to the LEO 1530 thermally-assisted field emission scanning electron microscope (Carl Zeiss SMT Inc., Germany). Figure 3.2 shows the EDS spectra of selected zeolite nanocomposites obtained from experiments A10 and A12. The EDS spectra show characteristics peaks from magnesium and oxygen in addition to the peaks for sodium, silicon, and aluminum, suggesting the presence of $Mg(OH)_2$ in the samples.

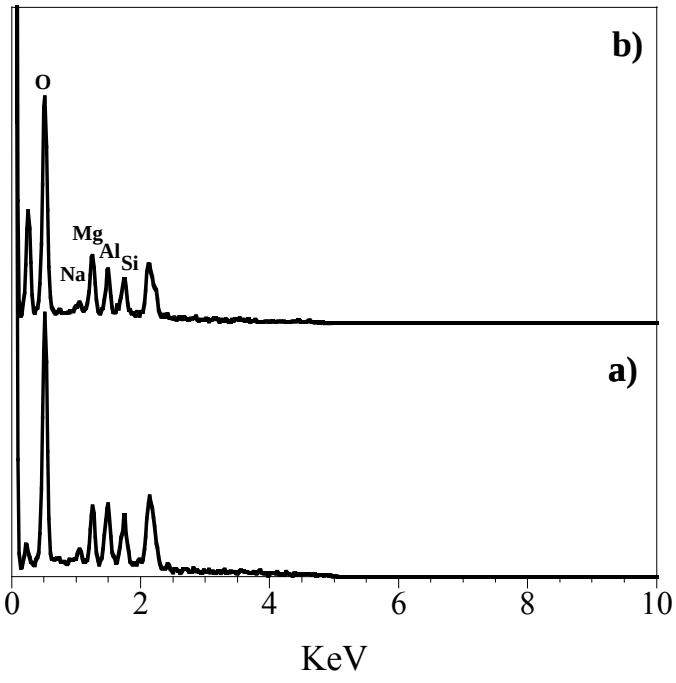

Fig. 3.2 EDS spectra of treated zeolites obtained from experiments (a) A10, (b) A12.

3-4-1-3 *X-ray Diffraction* (XRD)

Powder X-ray diffraction was used to identify the surface nanostructures and examine the crystallinity of the nanocomposites. Figure 3.3 displays the XRD patterns of virgin zeolite 4A, commercial $Mg(OH)_2$ powder, and selected zeolite nanocomposites. It can be seen that the zeolite nanocomposites maintained their crystallinity after treatment. Furthermore, the position of the new peaks resulting from the surface nanostructures are well matched with tabulated $Mg(OH)_2$ peaks. This confirms the presence of $Mg(OH)_2$ on the zeolite. The peaks were relatively weak and broad due to the high crystallinity of the large zeolite and the small size of the $Mg(OH)_2$ domains

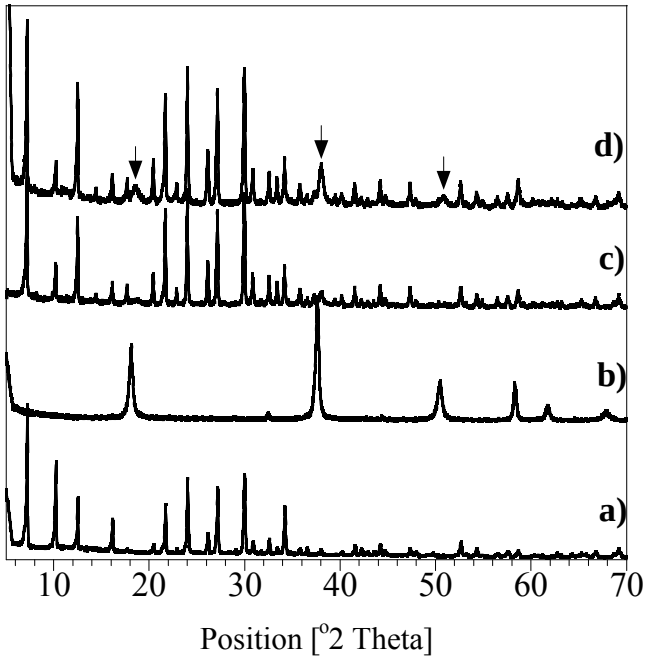

Fig. 3.3 XRD patterns of (a) virgin zeolite 4A, (b) commercial $Mg(OH)_2$ powder, (c, d) treated zeolites obtained from experiments A10 and A12, respectively. The zeolite structure and crystallinity remained intact after treatment. The peaks from nanocrystals created after treatment were well matched with tabulated $Mg(OH)_2$ peaks.

3-4-1-4 ***Fourier Transform Infrared (FTIR)***

Fourier Transform Infrared analysis was used for additional confirmation of $Mg(OH)_2$ in the nanocomposite. Figure 3.4 shows the FTIR spectra of virgin zeolite 4A, commercial $Mg(OH)_2$ powder, and zeolite nanocomposite samples obtained from experiment A10 and A12. The spectra of the zeolite nanocomposites can be matched with the spectrum of the virgin zeolite, with additional peaks detected at ~1400 cm^{-1} and 3400 cm^{-1}. These peaks can be attributed to the bending and stretching vibrations of the –OH bond in the crystal structure of $Mg(OH)_2$ [28, 29]. This result further confirms the presence of $Mg(OH)_2$ in the nanocomposite.

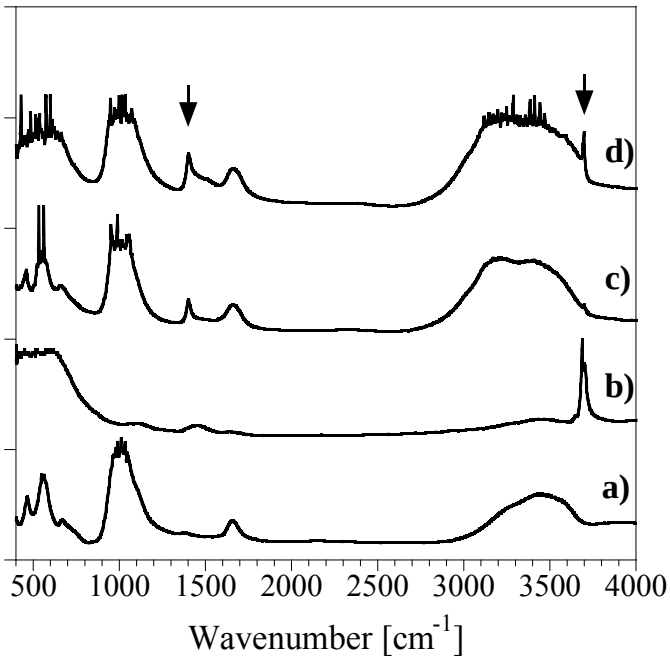

Fig. 3.4 FTIR spectra of (a) zeolite 4A, (b) magnesium hydroxide, and (c, d) treated zeolites obtained from A10 and A12 respectively. Peaks detected at ~ 1400 cm^{-1} and 3400 cm^{-1} in the treated zeolite 4A can be attributed to the bending and stretching vibration of the –OH bond in the crystal structure of $Mg(OH)_2$.

3-4-2 *Preliminary study of effect of temperature*

The experiments were carried out at high temperatures (623 K and 673 K) to investigate the effect of temperature on nanocomposite. SEM images of virgin zeolite 4A and magnesium hydroxide / zeolite 4A nanocomposites obtained from experiment D1 and D2 are shown in Fig. 3.5. As can be seen from this figure, virgin zeolite 4A (Fig 3.5a) morphology is cubic whereas the treated zeolites (Fig. 3.5b) were deformed and lost their cubic shape. Parts of the treated zeolites were covered with deposited nanostructures. However, coverage was not complete.

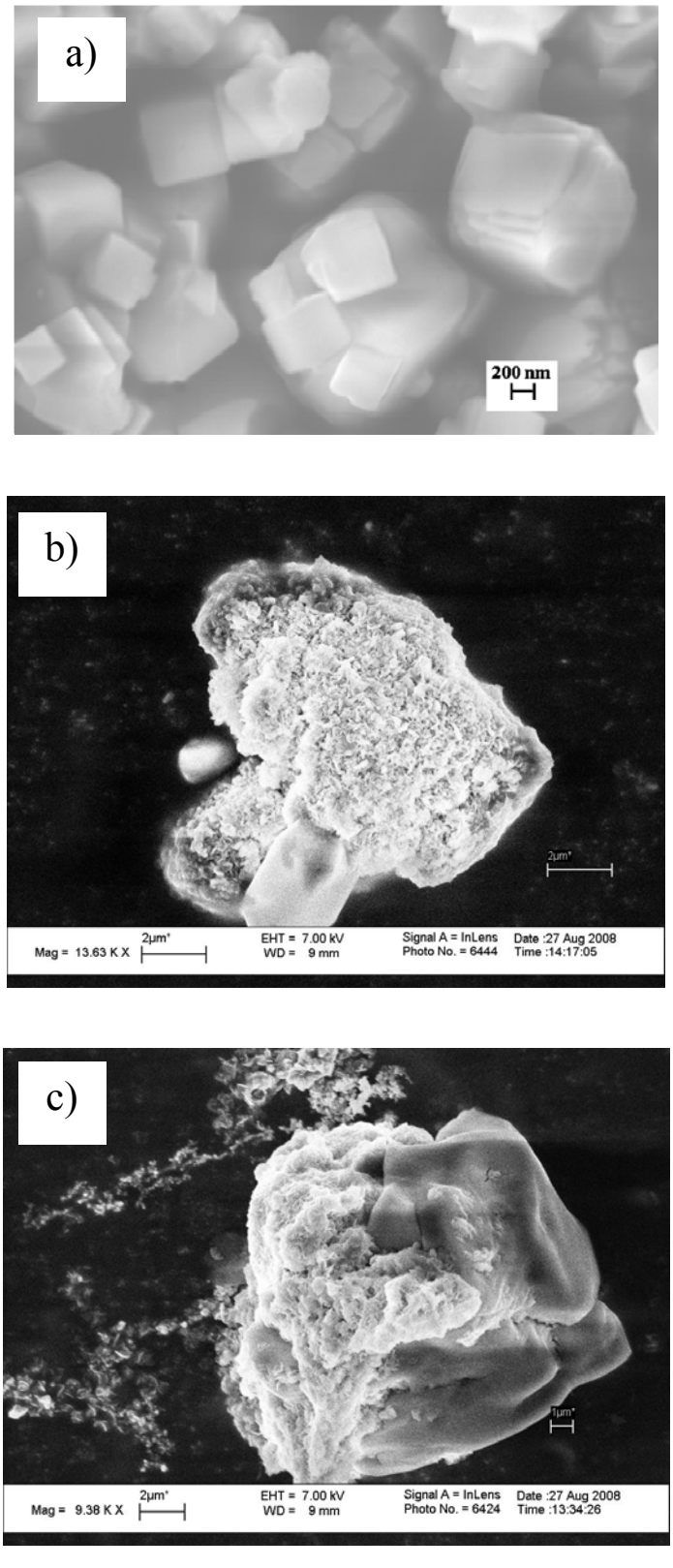

Fig. 3.5 SEM images of a) virgin zeolite 4A, treated zeolites obtained from experiments b) D1, c) D2.

3-4-3 *Influence of magnesium chloride concentration*

Four experiments (A9, A10, A11, A12) were performed to investigate the effects of magnesium chloride concentration on the formation of magnesium hydroxide nanopetals on zeolite 4A. The magnesium chloride concentrations in these experiments were 0.01 M, 0.04 M, 0.07 M, and 0.1 M respectively. From Table 3.1, it can be observed that the pH of the zeolite solution decreased as the concentration of magnesium chloride increased. Representative SEM images of the magnesium hydroxide / zeolite 4A nanocomposites are shown in Fig. 3.6. As can be seen from these images, the average size of the magnesium hydroxide nanopetals deposited on the surface increased as the concentration of magnesium chloride increased. Furthermore, the loading of $Mg(OH)_2$ in the nanocomposite apparently increased with increasing magnesium chloride concentration (discussed further in Chapter 4). However, the $Mg(OH)_2$ nanopetals showed a tendency towards intergrowth at high magnesium chloride concentration, while at lower concentration, single and well-defined platelets were obtained. These results show that the composition of magnesium hydroxide in the nanocomposite can be controlled by varying the concentration of magnesium chloride.

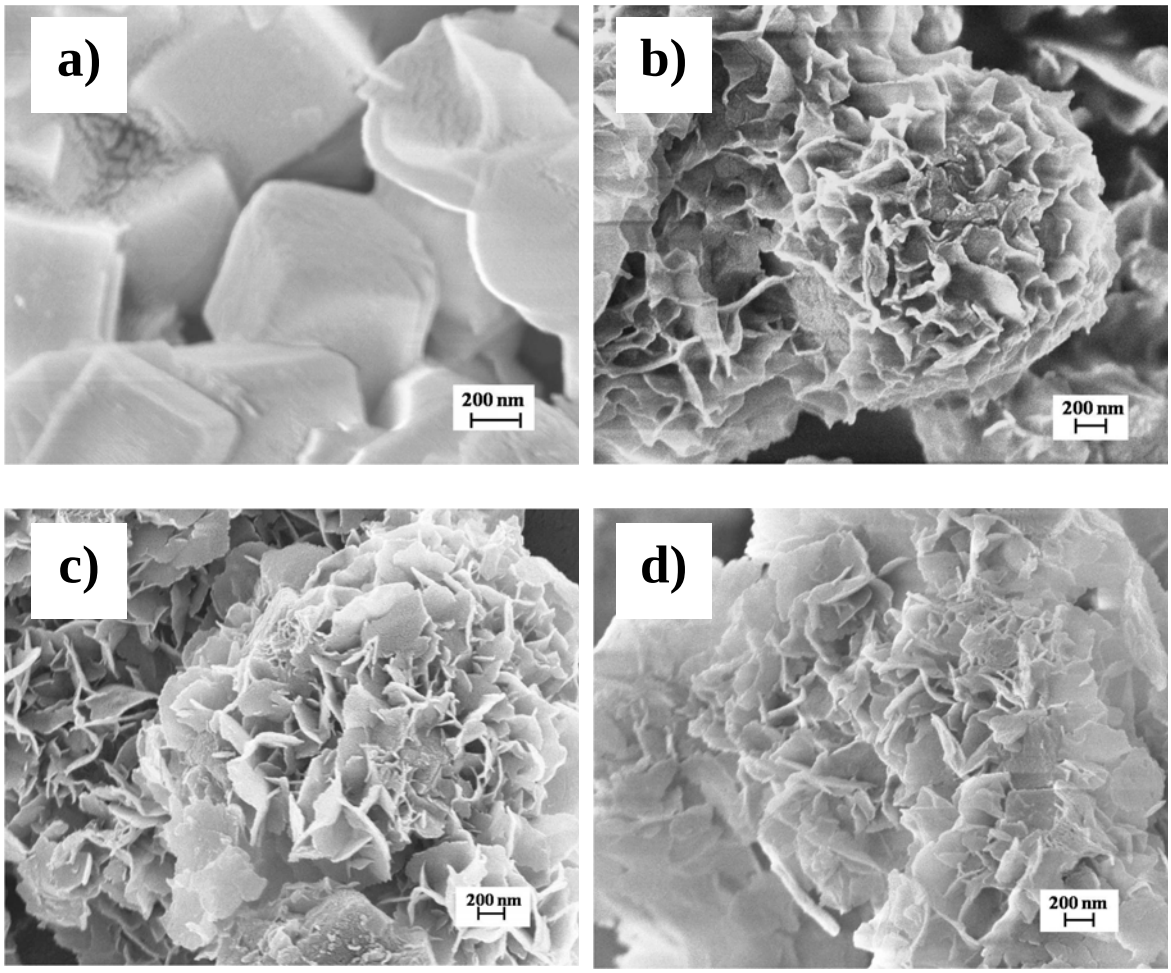

Fig. 3.6 Representative SEM images of zeolites obtained from experiments (a) A9, (b) A10, (c) A11, (d) A12.

3-4-4 *Influence of the base*

In order to examine the effects of pH on the formation of $Mg(OH)_2$/ zeolite nanocomposite, different precipitants including DI water, NaOH (strong base), and NH_4OH (weak base) were used in the synthesis. No experiments were conducted using acids since $Mg(OH)_2$ does not precipitate under acidic conditions in aqueous solution [17]. However, when a sol-gel method was used, whisker-like $Mg(OH)_2$ was obtained under acidic conditions [30] Experiments B1 – B4 were carried out with DI water as the precipitant. Figure 3.7 displays the SEM images of the zeolites obtained in these experiments. It can be clearly seen that no $Mg(OH)_2$ nanostructures were formed on the surfaces of these zeolites. When a strong base such as sodium hydroxide (NaOH) was used as the precipitant, $Mg(OH)_2$ nanoparticles were deposited on the surface of the zeolite (as shown in Fig. 3.7 e and f). Petal-like $Mg(OH)_2$ nanocrystals were obtained when a weak base such as ammonium hydroxide was used as the precipitant (see Fig. 3.8). From SEM images, the $Mg(OH)_2$ nanocrystals on the zeolite surfaces tended to be small and very thin, and had relatively high diameter to thickness ratio and surface area (see Fig. 3.8). Fig. 3.8 clearly shows that individual petals did not grow randomly but were homogeneously distributed on the surface. Furthermore, it can be seen that each petal is a thin platelet with defined edges.

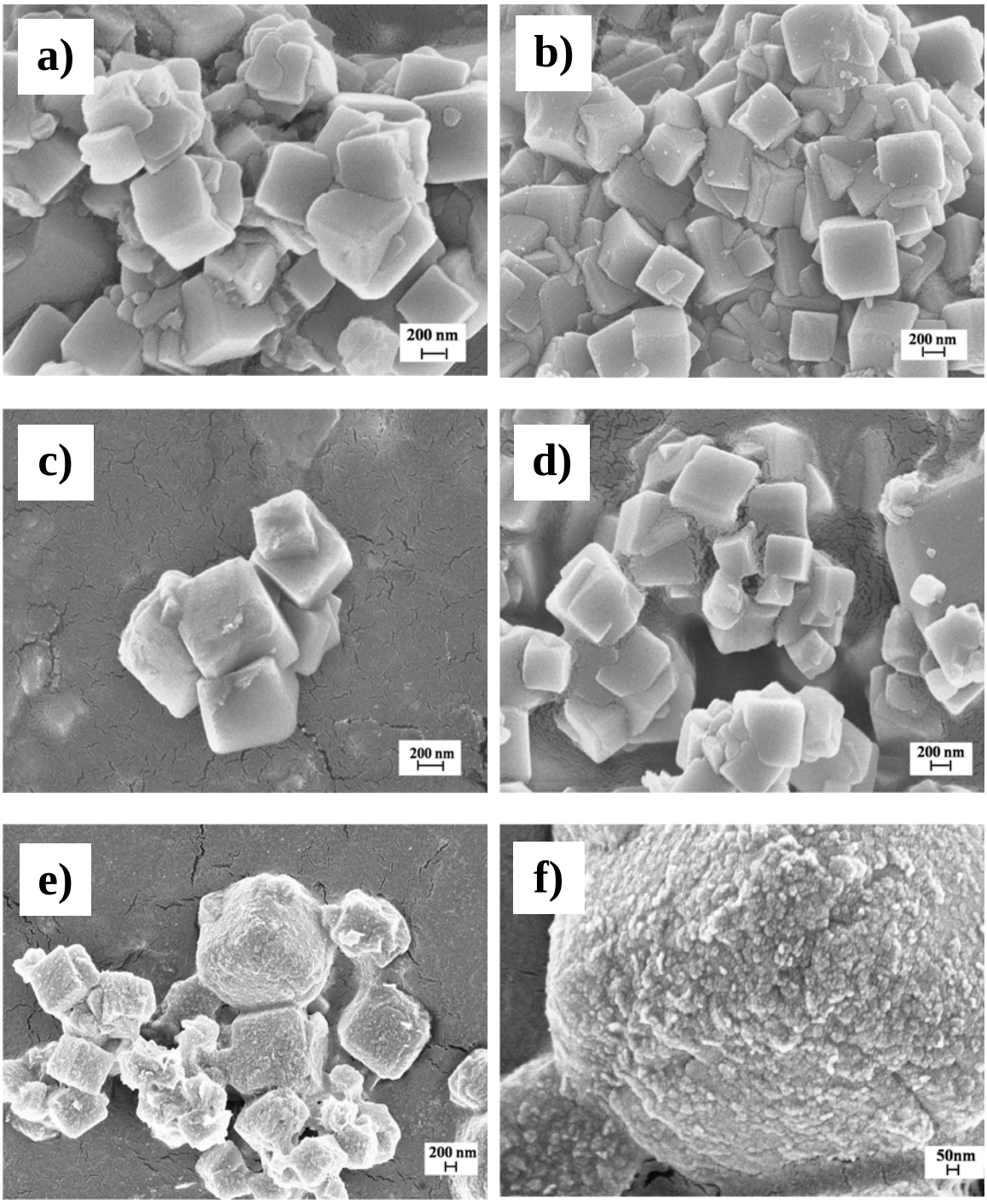

Fig. 3.7 Representative SEM images of treated zeolites obtained from experiments (a) B1, (b) B2, (c) B3, (d) B4, (e) C1, and (f) magnified image of (e).

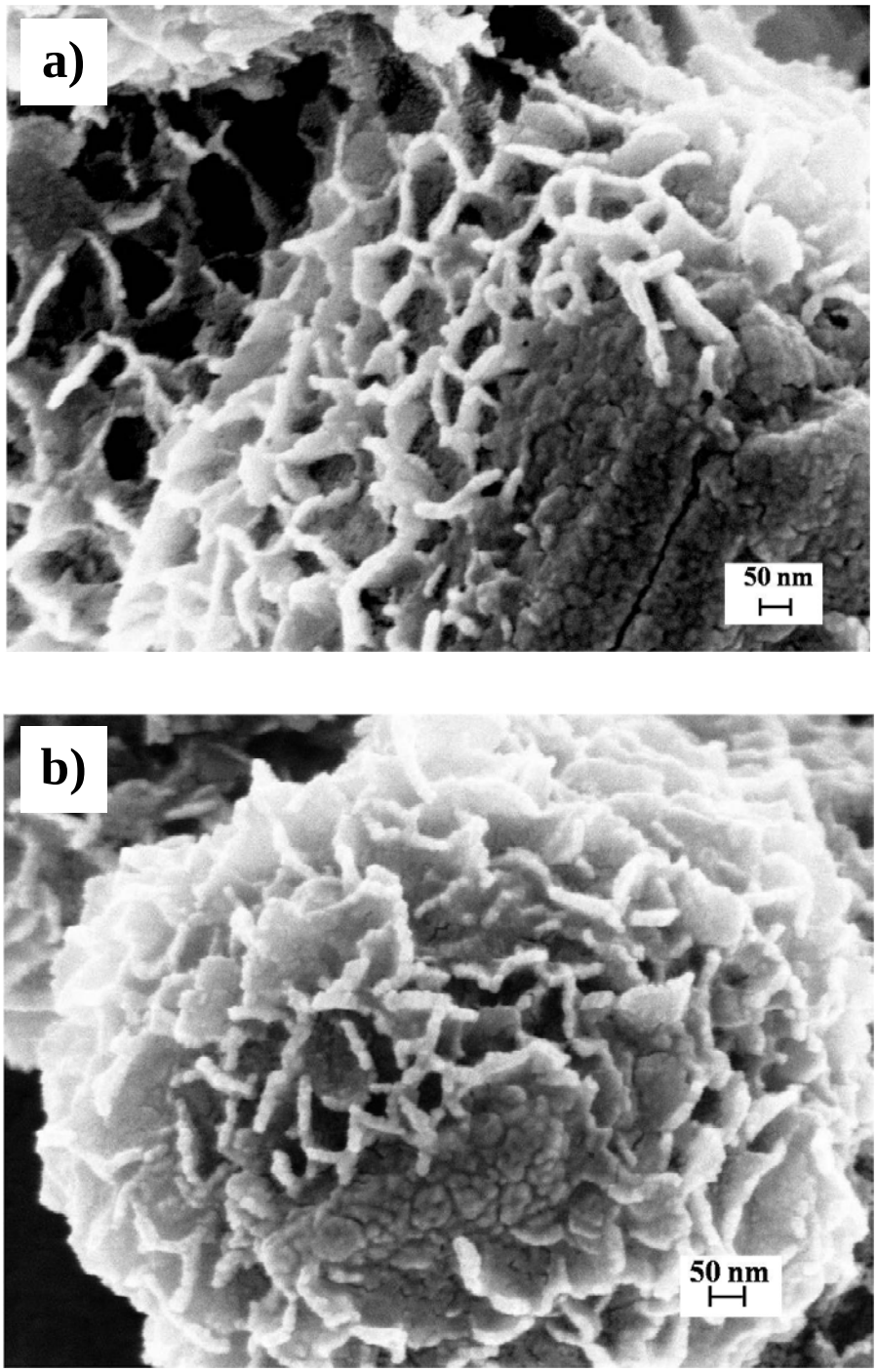

Fig. 3.8 Representative SEM images obtained from experiments (a) A3 and (b) A4.

3-4-5 *Effect of synthesis time*

The effect of synthesis time was investigated by collecting the zeolite particles at 24 h intervals for 72 h while keeping the temperature constant. From the SEM images shown in Fig. 3.9 it can be seen that the size and amount of $Mg(OH)_2$ nanopetals deposited on the zeolite increased as the synthesis time increased from 24 h to 48 h. However, the size and amount did not vary much when the synthesis time increased from 48 h to 72 h. Moreover, it can be seen that the magnesium hydroxide precipitated in 24 h consists of small imperfect thin plates. It only developed into well defined petal-like morphology during aging. The rate of formation and deposition of magnesium hydroxide can be obtained from Fig. 3.10. The weight percent of $Mg(OH)_2$ in the nanocomposite (discussed in chapter 4) increased from 10.49 % to 11.87 % when the synthesis time increased from 24 h to 48 h. However, as the synthesis time increased further to 72 h, the total weight percent of $Mg(OH)_2$ in the composite only increased by 0.49 % from 11.87 % to 12.36 %. This can also be seen by the change in Mg^{2+} ion concentration versus time as shown in Fig. 3.10.

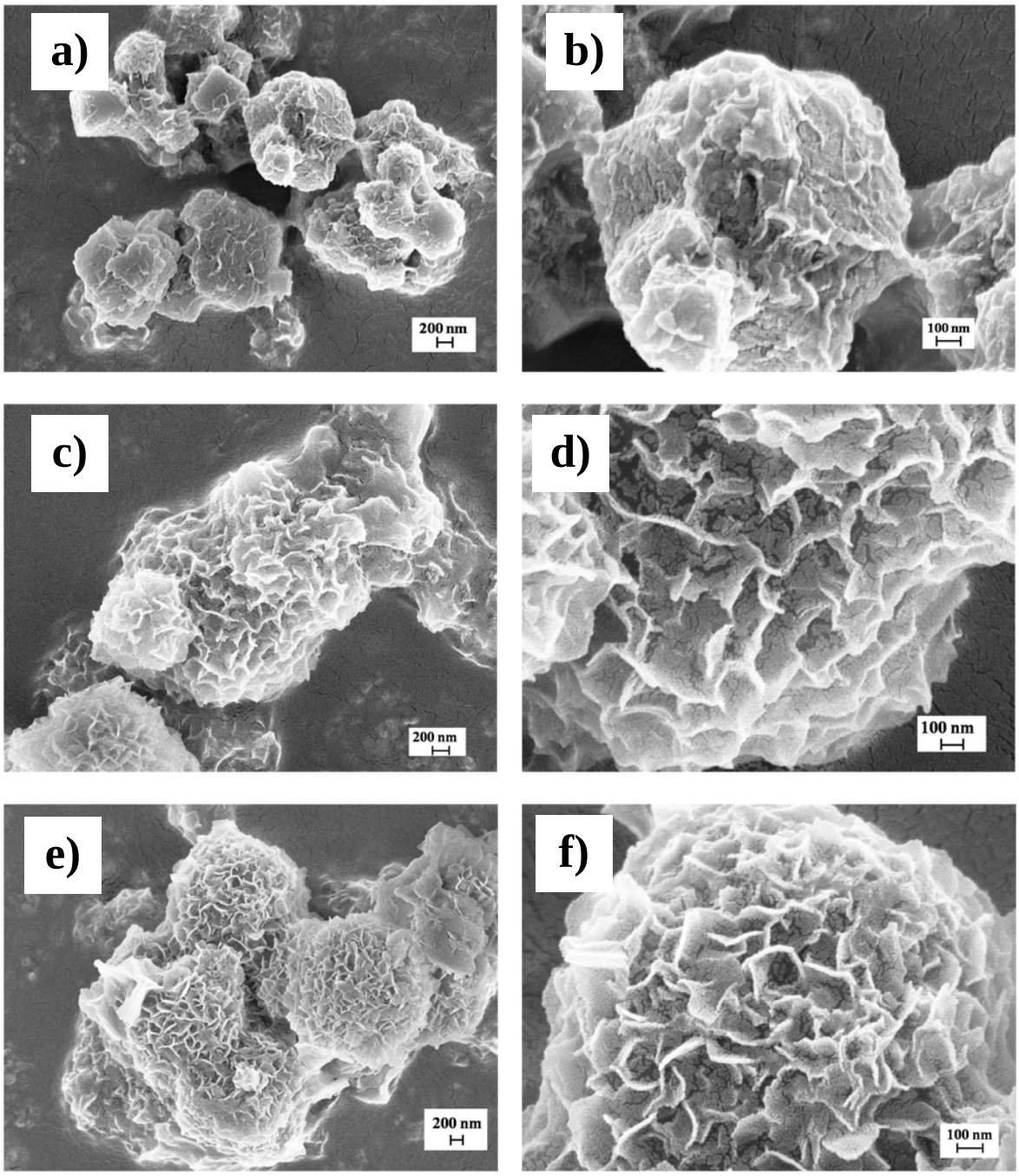

Fig. 3.9 Representative SEM images of treated zeolites at different magnification scales obtained from experiments (a,b) A2, (c,d) A6, and (e,f) A10.

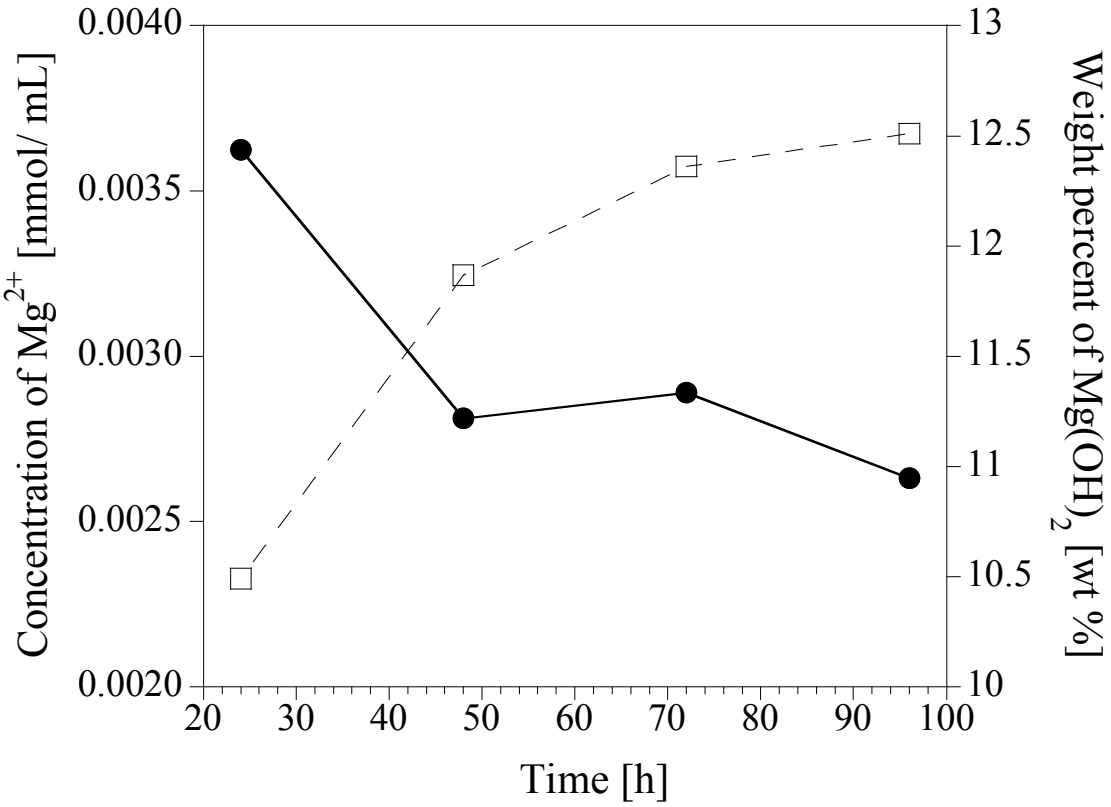

Fig. 3.10 Concentration of magnesium ions and weight percent of magnesium hydroxide deposited as a function of time. Dashed and solid lines represent weight percent of $Mg(OH)_2$ and concentration of Mg^{2+} respectively.

3-5 Discussion

The amount of $Mg(OH)_2$ deposited was expected to depend strongly on the concentration of magnesium ions, pH, and synthesis time. Table 3.1 shows that the pH of the solution decreased as the concentration of magnesium chloride increased. Mg^{2+} ions are weakly acidic [17] and when magnesium chloride dissolves in water, these ions behave as Lewis acids [31]. The positive charge on Mg^{2+} draws electron density from the O-H bond in water. As the unshared electron pairs of the water molecules are pulled closer to the Mg^{2+} ion, the electrons in O-H bond of water move closer to the oxygen to compensate for some of its loss of electron density. As a result, the hydrogen of the water molecule ends up with an increased positive charge. Eventually the O-H bond may dissociate, releasing an aqueous proton and leaving a hydroxide group attached to the Mg^{2+} ion, thus producing an acidic solution. Therefore, the pH of the solution decreases with increasing magnesium chloride concentration.

As can be seen from Fig. 3.5, $Mg(OH)_2$ / zeolite 4A nanocomposites could be obtained using sub- and supercritical water hydrothermal synthesis within 2 h. However, the resulting zeolite was deformed and lost its cubic shape. Subcritical water conditions are detrimental to the structure of the zeolite. It has been reported that the solubility of silica in water increases significantly at elevated temperatures [32]. Also, under subcritical to supercritical water conditions, alumina suffers intergranular corrosion at pH ~ 8 and completely dissolves at pH > 11 [33, 34]. Since zeolite 4A is made up of silica and alumina tetrahedra, it is very likely that the structure of zeolite will disintegrate at these conditions. Therefore, the sub- and supercritical water hydrothermal methods were not used for the synthesis of $Mg(OH)_2$ / zeolite 4A nanocomposites. Instead, the

deposition – precipitation method at ambient conditions was used to prepare the $Mg(OH)_2$ / zeolite 4A nanocomposites in this study.

No magnesium hydroxide nanostructures were visible on the zeolite surface at the lowest magnesium chloride concentration (Fig. 3.6). As the concentration increased to 0.04 M, the precipitated magnesium hydroxide consisted of individual particles in the form of hexagonal or truncated triangular platelets that were generally around 200 nm or less across. The diameter of the platelets increased with concentration, to around 400 nm at the highest concentration of 0.1 M used in this study.

The precipitation of magnesium hydroxide depends on the relation of the product $[Mg^{2+}] \times [OH]^2$ to the solubility-product K_{sp} of magnesium hydroxide [35], which is reported to be 1.5×10^{-12} [36]. This value corresponds to a solubility of magnesium hydroxide of $[Mg^{2+}] = 0.72 \times 10^{-4}$ mol L^{-1} and $[OH^-] = 2.07 \times 10^{-4}$ mol L^{-1}, respectively. Therefore, as the concentration of magnesium chloride increases, the heterogeneous zeolite solution becomes saturated with Mg^{2+} ions and the solubility product is exceeded [37]. Thus, high supersaturation level of the magnesium hydroxide building blocks $Mg(OH)_6^{4-}$ is obtained when ammonium hydroxide is added to the solution, resulting in the spontaneous formation of $Mg(OH)_2$ nuclei [38]. Depending on the supersaturation level of the solution, these nuclei may redissolve as rapidly as they form [39]. However, since the supersaturation level of the building blocks is high at elevated magnesium chloride concentration, the building blocks will continue to diffuse to the growing nuclei surface from the bulk solution and integrated into the crystal lattice. Therefore, larger magnesium hydroxide crystals were formed at higher concentration of magnesium chloride.

It can be seen from the above experiments that the nature of the base plays a significant role in the precipitation and formation of magnesium hydroxide and its morphology. Without a base, no visible magnesium hydroxide nanostructures were formed on the zeolite surface, although the solution was supersaturated with magnesium ions and the conditions were feasible for the precipitation of magnesium hydroxide (experiments B1 – B4). The Mg^{2+} ion is considered to be weakly acidic with a p*K*a of about 11.4 [17]. Weakly acidic cations show enough acidity to precipitate insoluble metal hydroxides at pH values over their p*K*a (i.e., in neutral or just slightly basic solutions). However, if the solution is not made basic, hydrated metal ion will be the predominant form [17]. Therefore, in experiments B1 – B4, dissolved magnesium ions remained predominantly as hydrated magnesium ions and did not form $Mg(OH)_2$ in the absence of a base.

According to previous reports, some significant variables during the growth of $Mg(OH)_2$ are the solution pH and nature of the base [38]. When a strong base such as NaOH was added to the zeolite solution, tiny particles of magnesium hydroxide were found on the surface of the zeolite (as shown in Fig 3.7e and f). A strong base dissolves completely in water to give stoichiometric quantities of hydroxide ions. The initial pH in the reacting mixture was about ~13 and settled at a pH of about ~11 at the end of 72 h. The elevated pH value created a high supersaturation level due to the high OH^- concentration. This resulted in a very fast nucleation of $Mg(OH)_6^{4-}$ building blocks and generated tiny and ill-defined $Mg(OH)_2$ nuclei [40]. In order to decrease the surface energy, the small $Mg(OH)_2$ nuclei tend to aggregate, adopting an irregular shape [38]. In addition, the isoelectric point of $Mg(OH)_2$ is around 11-12 [38, 41]. Above this value, the

growing $Mg(OH)_2$ nuclei are negatively charged. In the case of samples prepared with NaOH as the base, the initial pH of the medium was 13. Therefore under this condition, the sodium ions are attracted to the negative surfaces of the growing $Mg(OH)_2$ nuclei. Due to their high concentration and small hydration sphere in solution, the sodium ions probably adsorbed significantly onto all facets of the nuclei, without any selectivity, thus hindering the attachment of fresh $Mg(OH)_6^{4-}$ and decrease the growth rate of the nuclei [16]. This is also in agreement with the observation that increases in alkalinity tend to cause a decrease in particle size of $Mg(OH)_2$ [42]. It has also been reported previously by Ivanova et al. [43] that magnesium hydroxide precipitated with a strong base such as KOH has a smaller specific surface and size than when ammonia liquor is used. In general, when the supersaturation level is too high, the system mainly experiences the nucleation process and monodispersed particles will be obtained [27].

Petal-like $Mg(OH)_2$ nanocrystals were created on zeolite surfaces when a weak base such as ammonium hydroxide was used as the precipitant (as shown in Fig 3.8). The possible mechanism of forming such petal-like morphology may be due to the anisotropic structure of $Mg(OH)_2$ [44]. $Mg(OH)_2$ has a layered brucite crystal structure [16] and this intrinsic crystal property may dominate the shape of the primary $Mg(OH)_2$ particles [45], resulting in the formation of the petal-like crystals. A weak base such as ammonium hydroxide is only slightly dissociated into ammonium and hydroxide ions in solution, and some of it decomposes into ammonia and water [46]. Thus, the concentration of hydroxide ions in the zeolite solution increased slowly and allowed the pH to rise homogenously throughout the solution. The pH of the suspension when using ammonium hydroxide as precipitant was about pH 10 at the start of the experiment (which is very

close to the p*K*a value of Mg^{2+}) [17]. These conditions are favorable for the precipitation and growth of $Mg(OH)_2$. Several authors [16, 28, 41, 47, 48] have determined the isoelectric point of $Mg(OH)_2$ in water to be about pH 11-12. Therefore, $Mg(OH)_2$ particles are positively charged when the solution pH is around 10 and the adsorption of cations such as ammonium ions is not favored anymore. Moreover, the ammonium cation is larger than the sodium ion and is not easily adsorbed on the crystal facets. Furthermore, since ammonium hydroxide is only partially dissociated in aqueous solution, the supersaturation level is lower compared to that of NaOH. Subsequently, the rate of crystal growth is higher than the rate of nucleation when ammonium hydroxide is used as the base precipitant. Similar growth mechanism of the petal-like $Mg(OH)_2$ has also been reported by Xue and co-workers [44, 49-51]. It was shown that when ammonium hydroxide is used as the precipitant, the growth rates of the (001) and (100) planes are the slowest and the morphology of $Mg(OH)_2$ is determined by these two planes [49, 51]. Structurally, it can be found that both {001} and {100} planes are composed of Mg^{2+}, but the atom density of {001} planes is larger than that of {100} planes [51]. During the growth process, the amount of dissociated ammonium hydroxide adsorbed on the {001} planes is more than the {100} planes, suppressing the growth of the {001} planes [51]. Thus, the use of ammonium hydroxide resulted in a low supersaturation level which favors edgewise growth of petal-like magnesium hydroxide in directions lying in the basal crystallographic plane rather than growth along the *c*-axis [42, 47]. In addition, precipitation of magnesium hydroxide is reversible by the byproduct ammonium chloride [46, 52]. A large amount of ammonium chloride in the solution results in the decrease of ionization rate of ammonium hydroxide, therefore the formation rate of OH^- is decreased

[49]. Together these factors contributed to the slow self assembly process of the magnesium hydroxide into a petal – like morphology on the zeolite surface.

As can be seen from Fig. 3.9 and 3.10, the size and total mass of magnesium hydroxide in the nanocomposite increased with increasing synthesis time while the concentration of magnesium ion in the solution decreased. From the SEM images shown in Fig. 3.9 it can be seen that the size and amount of $Mg(OH)_2$ nanopetals deposited on the zeolite increased as the synthesis time increased from 24 h to 48 h. However, the size and amount did not vary much when the synthesis time increased from 48 h to 72 h. At the beginning, large amounts of starting materials dissolved and concentrations of magnesium ions in solution were high. This resulted in the initial rapid deposition of $Mg(OH)_2$ on the surface as observed from Fig. 3.9a-d and Fig. 3.10. After about 48 h, the concentration of Mg^{2+} ions in the solution approached their equilibrium value which retarded the growth of $Mg(OH)_2$ nanopetals. As the synthesis time increased, the amount of magnesium ions available for nucleation and formation of magnesium hydroxide decreased. Consequently, the rate of magnesium hydroxide formation and deposition decreased as well. It may therefore be assumed that increasing the magnesium hydroxide concentration increases the size of magnesium hydroxide crystals which decreases the concentration of magnesium ions in the solution.

3-6 Conclusions

A facile deposition – precipitation method was developed for the preparation of magnesium hydroxide nanostructures on zeolite 4A. The method employed an aqueous solution of magnesium chloride and ammonium hydroxide at ambient conditions. The size and precipitation of $Mg(OH)_2$ nanostructures increased with increasing magnesium chloride concentration. The use of a strong base (NaOH) led to the formation of tiny $Mg(OH)_2$ particles, while synthesis driven with a weak base (NH_4OH) promoted the obtaining of petal- shaped nanostructures. Increasing the synthesis time facilitated the crystal growth of $Mg(OH)_2$ nanostructure and composition of $Mg(OH)_2$ in the $Mg(OH)_2$/ zeolite nanocomposite.

3-7 References

1. Campanati, M., G. Fornasari, and A. Vaccari, *Fundamentals in the preparation of heterogeneous catalysts.* Catalysis Today, 2003. **77**(4): p. 299-314.

2. Perego, C. and P. Villa, *Catalyst preparation methods.* Catalysis Today, 1997. **34**(3-4): p. 281-305.

3. Bhatia, S., *Zeolite catalysis : Principles and applications*. 1990, Boca Raton, Fla. :: CRC Press.

4. Savage, N.F., *Nanotechnology applications for clean water*. 2009, Norwich, NY: William Andrew.

5. Regalbuto, J., ed. *Catalyst preparation : Science and engineering*. 2007, CRC Press/Taylor & Francis: Boca Raton.

6. Xu, C., *Continuous and batch hydrothermal synthesis of metal oxide nanoparticles and metal oxide-activated carbon nanocomposites*. 2006, Georgia Institute of Technology: United States -- Georgia. p. 258.

7. Cote, L.J., A.S. Teja, A.P. Wilkinson, and Z.J. Zhang, *Continuous hydrothermal synthesis and crystallization of magnetic oxide nanoparticles.* Journal of Materials Research, 2002. **17**(9): p. 2410-2416.

8. Cote, L.J., A.S. Teja, A.P. Wilkinson, and Z.J. Zhang, *Continuous hydrothermal synthesis of $CoFe_2O_4$ nanoparticles.* Fluid Phase Equilibria, 2003. **210**(2): p. 307-317.

9. Hao, Y.L. and A.S. Teja, *Continuous hydrothermal crystallization of a-Fe_2O_3 and Co_3O_4 nanoparticles.* Journal of Materials Research, 2003. **18**(2): p. 415-422.

10. Lee, J. and A.S. Teja, *Characteristics of lithium iron phosphate ($LiFePO_4$) particles synthesized in subcritical and supercritical water.* Journal of Supercritical Fluids, 2005. **35**(1): p. 83-90.

11. Xu, C. and A.S. Teja, *Continuous hydrothermal synthesis of iron oxide and PVA-protected iron oxide nanoparticles.* The Journal of Supercritical Fluids, 2008. **44**(1): p. 85-91.

12. Xu, C.B. and A.S. Teja, *Supercritical water synthesis and deposition of iron oxide (alpha-Fe2O3) nanoparticles in activated carbon.* Journal of Supercritical Fluids, 2006. **39**(1): p. 135-141.

13. Lee, J. and A.S. Teja, *Synthesis of $LiFePO_4$ micro and nanoparticles in supercritical water.* Materials Letters, 2006. **60**(17-18): p. 2105-2109.

14. Holm, L.J., *Continuous hydrothermal synthesis and crystallization of magnetic oxide nanoparticles*. 2001, Georgia Institute of Technology: United States -- Georgia.

15. Teja, A.S. and P.-Y. Koh, *Synthesis, properties, and applications of magnetic iron oxide nanoparticles.* Progress in Crystal Growth and Characterization of Materials. **55**(1-2): p. 22-45.

16. Henrist, C., J.P. Mathieu, C. Vogels, A. Rulmont, and R. Cloots, *Morphological study of magnesium hydroxide nanoparticles precipitated in dilute aqueous solution.* Journal of Crystal Growth, 2003. **249**(1-2): p. 321-330.

17. Wulfsberg, G., *Inorganic Chemistry*. 2000, Sausalito, Calif.: University Science Books.

18. Booth, N.A., T. Land, P. Erhmann, and P.G. Vekilov, *The aspect ratio of potassium dideuterium phosphate (DKDP) crystals.* Crystal Growth & Design, 2004. **5**(1): p. 105-110.

19. Xu, D. and D. Xue, *Chemical bond analysis of the crystal growth of KDP and ADP.* Journal of Crystal Growth, 2006. **286**(1): p. 108-113.

20. Bennema, P., H. Meekes, S.X.M. Boerrigter, H.M. Cuppen, M.A. Deij, J. van Eupen, P. Verwer, and E. Vlieg, *Crystal growth and morphology: new developments in an integrated Hartman-Perdok-connected net-roughening transition theory, supported by computer simulations.* Crystal Growth & Design, 2004. **4**(5): p. 905-913.

21. Hartman, P. and W.G. Perdok, *On the relations between structure and morphology of crystals. I.* Acta Crystallographica, 1955. **8**(1): p. 49-52.

22. Hartman, P. and W.G. Perdok, *On the relations between structure and morphology of crystals .2.* Acta Crystallographica, 1955. **8**(9): p. 521-524.

23. Hartman, P. and W.G. Perdok, *On the relations between structure and morphology of crystals .3.* Acta Crystallographica, 1955. **8**(9): p. 525-529.

24. *Encyclopedia of surface and colloid science*, ed. A.T. Hubbard. 2002, New York :: Marcel Dekker.

25. *Crystallization and solidification properties of lipids*, ed. N. Widlak, R.W. Hartel, and S. Narine. 2001, Champaign, Ill. :: AOCS Press.

26. *Science and technology of crystal growth*, ed. J.P.v.d. Eerden and O.S.L. Bruinsma. 1995, Dordrecht ;: Kluwer Academic Publishers.

27. Zhou, Z., *Synthesis of one-dimensional nanostructure materials*. 2009, Georgia Institute of Technology: United States -- Georgia. p. 179.

28. Wu, X.F., G.S. Hu, B.B. Wang, and Y.F. Yang, *Synthesis and characterization of superfine magnesium hydroxide with monodispersity.* Journal of Crystal Growth, 2008. **310**(2): p. 457-461.

29. de Oliveira, E.F. and Y. Hase, *Infrared study and isotopic effect of magnesium hydroxide.* Vibrational Spectroscopy, 2001. **25**(1): p. 53-56.

30. Junqiang, L., *Development of next generationmixed matrix hollow fiber membranes for butane isomer separation*, in *Chemical & Biomolecular Engineering*. 2010, Georgia Institute of Technology.

31. Livage, J., *Sol-gel synthesis of heterogeneous catalysts from aqueous solutions.* Catalysis Today, 1998. **41**(1-3): p. 3-19.

32. Poole, C.F., *The essence of chromatography* 2003, Amsterdam: Elsevier. 925.

33. *High pressure process technology fundamentals and applications*. 1st ed. ed. Industrial chemistry library ;, ed. A. Bertucco and G. Vetter. 2001, Amsterdam :: Elsevier.

34. Boukis, N., N. Claussen, K. Ebert, R. Janssen, and M. Schacht, *Corrosion screening tests of high-performance ceramics in supercritical water containing oxygen and hydrochloric acid.* Journal of the European Ceramic Society, 1997. **17**(1): p. 71-76.

35. Stieglitz, J., *The elements of qualitative chemical analysis, with special consideration of the application of the laws of equilibrium and of the modern theories of solution*. 1911, New York: Century Co.

36. Wiberg, E., N. Wiberg, and A.F. Holleman, *Inorganic chemistry*. 2001, San Diego, Calif. : Berlin: Academic Press, W. de Gruyter.

37. *Inorganic chemistry*. Topics in current chemistry ed. J.H. Holloway. 1984, Berlin ;: Springer-Verlag.

38. Matos, C.R.S., M.J. Xavier, L.S. Barreto, N.B. Costa, and I.F. Gimenez, *Principal Component Analysis of X-ray Diffraction Patterns To Yield Morphological Classification of Brucite Particles.* Analytical Chemistry, 2007. **79**(5): p. 2091-2095.

39. Baird, T., P.S. Braterman, H.D. Cochrane, and G. Spoors, *Magnesium hydroxide precipitation as studied by gel growth methods.* Journal of Crystal Growth, 1988. **91**(4): p. 610-616.

40. Lv, J., L. Qiu, and B. Qu, *Controlled growth of three morphological structures of magnesium hydroxide nanoparticles by wet precipitation method.* Journal of Crystal Growth, 2004. **267**(3-4): p. 676-684.

41. Pokrovsky, O.S. and J. Schott, *Experimental study of brucite dissolution and precipitation in aqueous solutions: surface speciation and chemical affinity control.* Geochimica et Cosmochimica Acta, 2004. **68**(1): p. 31-45.

42. Phillips, V.A., J.L. Kolbe, and H. Opperhauser, *The growth of $Mg(OH)_2$ crystals from $MgCI_2$ and $Ca(OH)_2$ in a brine environment.* Journal of Crystal Growth, 1977. **41**(2): p. 235-244.

43. Turek, M. and W. Gnot, *Precipitation of magnesium hydroxide from brine.* Industrial & Engineering Chemistry Research, 1995. **34**(1): p. 244-250.

44. Yan, C. and D. Xue, *Novel self-assembled MgO nanosheet and its precursors.* The Journal of Physical Chemistry B, 2005. **109**(25): p. 12358-12361.

45. Duan, X., D. Evans, J. He, M. Wei, B. Li, Y. Kang, and X. Duan, *Preparation of layered double hydroxides*, in *Layered Double Hydroxides*. 2006, Springer Berlin / Heidelberg. p. 89-119.

46. Caven, R.M., *Systematic inorganic chemistry from the standpoint of the periodic law*. 5th ed., revised ed, ed. G.D. Lander and A.B. Crawford. 1936, London: Blackie.

47. Phillips, V.A., J.L. Kolbe, and H. Opperhauser, *Effect of pH on the growth of $Mg(OH)_2$ crystals in an aqueous environment at 60 ^oC.* Journal of Crystal Growth, 1977. **41**(2): p. 228-234.

48. Yan, H., J.M. Wu, X.C. Zhang, Y. Zhang, L.Q. Wei, X.G. Liu, and B.S. Xu, *Synthesis of magnesium hydroxide nanoneedles and short nanorods on polymer dispersant template.* Journal of Materials Research, 2007. **22**(9): p. 2544-2549.

49. Xue, D., X. Yan, and L. Wang, *Production of specific $Mg(OH)_2$ granules by modifying crystallization conditions.* Powder Technology, 2009. **191**(1-2): p. 98-106.

50. Yan, C., D. Xue, and L. Zou, *Fabrication of hexagonal MgO and its precursors by a homogeneous precipitation method.* Materials Research Bulletin, 2006. **41**(12): p. 2341-2348.

51. Hardwell, T.G., *Astrophysics and condensed matter*. Horizons in world physic, ed. T.G. Hardwell. 2008, New York: Nova Science Publishers. 269.

52. Walker, J., *Introduction to physical chemistry*. 10th ed. ed. 1927, London: Macmillan.

CHAPTER 4

PROPERTIES OF $Mg(OH)_2$/ ZEOLITE NANOCOMPOSITES

In this chapter, the surface area, pore volume, and composition of $Mg(OH)_2$/ zeolite nanocomposites were measured and membranes were developed by dispersing zeolite 4A and $Mg(OH)_2$ / zeolite nanocomposites in a commercially available polymer (Ultem®). Ultem®, also known as poly(ether-imide), was selected as the continuous phase for all membranes as it is a glassy polymer with high glass transition temperature (Tg) and possesses high gas permeability and selectivity as well as high thermal stability and solvent resistivity [1, 2]. Hybrid (mixed-matrix) membranes were fabricated by a solution-casting method with different loadings of bare zeolite and $Mg(OH)_2$ / zeolite nanocomposites. The mechanical and thermal properties of the hybrid membranes were evaluated.

The equipment and techniques used to measure the properties of the zeolite nanocomposites are described in Section 4-1, followed by fabrication of hybrid membranes in Section 4-2, and determination of the thermal and mechanical properties of the hybrid membranes in Section 4-3. The effects of the magnesium hydroxide nanostructures on the interfacial adhesion between zeolites and Ultem® polymer matrix are discussed in Section 4-4.

4-1 Determination of the properties of zeolite nanocomposites

4-1-1 *Surface area and pore volume by Brunauer-Emmett-Teller (BET) Analysis*

The surface area and porosity of selected zeolite nanocomposite obtained from experiment A10 were obtained using cryogenic oxygen physisorption at 77 K. This analysis was carried out using a Micromeritics Instrument Corp. (Norcross, GA) ASAP 2020 instrument. The external surface area is given as the difference between the BET surface area (O_2 adsorption) and the micropore surface area determined according to the t-plot method [3]. The objective of the porosity measurement was to examine whether channels/ pores of the zeolite were plugged by the growth of $Mg(OH)_2$ nanostructures during the deposition – precipitation process. A decrease in the pore volume would suggest blockage of these channels/ pores. Table 4.1 gives BET surface area and porosity characteristics of bare zeolite 4A and the magnesium hydroxide / zeolite nanocomposite obtained in experiment A10. It can be seen that the pore volume of selected treated zeolite from A10 is larger than the pore volume of virgin zeolite. This suggests that magnesium hydroxide nanostructures did not grow inside the zeolite pores and that the increase in pore volume is most likely due to replacement of sodium ions in the virgin zeolite by magnesium ions during treatment. The magnesium ion has a smaller ionic radius than sodium and one magnesium ion could replace two sodium ions. This would lead to an increase in the pore volume of the treated zeolite. This indicates that the pores of the zeolite nanocomposites prepared using this method are not plugged by the nanostructures. In the present study, liquid oxygen was used as the probe molecule for BET surface area measurement. Although nitrogen is the usual choice for the probe molecule, it is not the best choice for measuring the micropore volume of a zeolite. For

small pore zeolites such as zeolite NaA, nitrogen may not be able to enter the zeolite framework [4]. Furthermore, nitrogen isotherms commonly show complex changes in packing density leading to hysteresis of the isotherm which may not give a true representation of the pore volume [4, 5].

Table 4-1 External surface area and pore volumes of bare zeolite and treated zeolite obtained from experiment A10

Samples	Surface area (m^2 g^{-1})	Pore volume (cm^3 g^{-1})
Virgin zeolite	302.18	0.147
Treated zeolite from A10	422.18	0.243

4-1-2 *Composition of the zeolite nanocomposite via thermogravimetric analysis (TGA)*

Thermogravimetric analysis (TGA) was used to determine the composition and thermal behavior of the $Mg(OH)_2$ / zeolite nanocomposite as a function of magnesium chloride concentration and synthesis time. From chapter 3, it was hypothesized that the composition of $Mg(OH)_2$ in the nanocomposite should increase with increasing concentration and synthesis time. At higher concentration, the aqueous solution becomes more saturated with magnesium ions which is conducive to the precipitation of $Mg(OH)_2$. A longer synthesis time is favorable for the crystal growth of $Mg(OH)_2$. These analyses were performed using a Netzsch STA 409 PC Luxx thermobalance (Selb, Germany). A N_2 gas sweep at a flow rate of 25 ml /min was used during TGA measurements. The heating procedure was set up as follows: (1) the temperature was raised from room temperature to 443 K at a rate of 2 K/ min, kept at 443 K for 90 minutes, then increased

from 440 K to 683 K at a rate of 10 K / min, and kept at 683 K for another 90 min before cooling down.

The weight percent $Mg(OH)_2$ in the nanocomposite was determined from differences in the weight loss due to desorption of water molecules and exclusion of occluded water molecules from both virgin zeolite 4A and treated zeolite 4A. The TGA results of virgin zeolite 4A, and $Mg(OH)_2$ / zeolite 4A nanocomposite obtained at various synthesis times (A2, A6, A10) and magnesium chloride concentrations (A9, A11, A12) are shown in Fig. 4.1 and Fig 4.2 respectively. The TGA curve of virgin zeolite 4A shows weight loss intervals at 443 K and 683 K, corresponding to the exclusion of adsorbed water and occluded water molecules. In treated zeolite 4A, the first weight loss stage at 443 K corresponds to the desorption of physisorbed water from the surface of zeolite and $Mg(OH)_2$ nanopetals. All of the treated zeolite 4A obtained from experiments A2, A6, A9, A10, A11, and A12 experienced similar weight loss at this stage. It can also be seen that treated zeolite 4A suffered a larger weight loss than virgin zeolite 4A during the first heating step to 443 K. This could be due to the larger surface area of $Mg(OH)_2$ nanopetals around the surface of zeolite 4A. Moreover, the treated zeolite 4A also suffered greater weight loss than virgin zeolite 4A at 683 K. The weight loss at 683 K is most likely due to the exclusion of occluded water molecules and thermal decomposition of $Mg(OH)_2$ [6, 7]. In addition, the weight losses from samples A6 (~ 6.18%) and A10 (~6.32%) are slightly more than sample A2 (~5.81%), indicating that more $Mg(OH)_2$ nanopetals were deposited at longer synthesis times. On the other hand, it can be seen from Fig. 4.2 and Table 4.2 that the weight percent of magnesium hydroxide in the

$Mg(OH)_2$ / zeolite nanocomposite increased as the concentration of magnesium chloride increased.

Assuming that the treated zeolite 4A has the same amount of occluded water molecules as the virgin zeolite, the weight percent of $Mg(OH)_2$ nanopetals formed on the surface of treated zeolite 4A can be calculated as follows:

$$w_{Mg(OH)2} = \frac{1 - w_{treated,1} - \left(1 + \frac{w_{virgin,2}}{w_{virgin,end}}\right) w_{treated,end}}{1 - \left(1 + \frac{w_{virgin,2}}{w_{virgin,end}}\right) \frac{M_{MgO}}{M_{Mg(OH)2}}} \qquad (1)$$

Here $w_{\text{treated, 1}}$ is the weight loss of the treated zeolite 4A at the first heating step and $w_{\text{virgin, 2}}$ is the weight loss of the virgin zeolite 4A at the second heating step. Also $w_{\text{treated, end}}$ and $w_{\text{virgin, end}}$ are the weight percent of the remaining treated and virgin zeolite 4A at the end of the second heating step. M_{MgO} (= 40.32) and $M_{\text{Mg(OH)2}}$ (= 58.32) are the molecular weights of MgO and $Mg(OH)_2$ respectively. From the TGA curve (Fig. 4.1), $w_{\text{virgin, 2}}$ and $w_{\text{virgin, end}}$ are 3.09 % and 79.01 % respectively. The values of $w_{\text{treated, end}}$ and weight percent of magnesium hydroxide in the $Mg(OH)_2$ / zeolite nanocomposite obtained from experiments A2, A6, A9, A10, A11, and A12 are displayed in the Table 4-2.

Table 4-2 Values of $w_{\text{treated, end}}$ and composition of $Mg(OH)_2$ / zeolite nanocomposite

Expt. no	$w_{\text{treated, end}}$	Weight percent of $Mg(OH)_2$ [wt. %]
A2	73.13 %	10.49 ± 1.25
A6	72.75 %	11.79 ± 0.07
A9	74.72 %	4.98 ± 0.44
A10	72.60%	12.36 ± 0.30
A11	71.14 %	18.46 ± 0.02
A12	70.14 %	23.89 ± 0.41

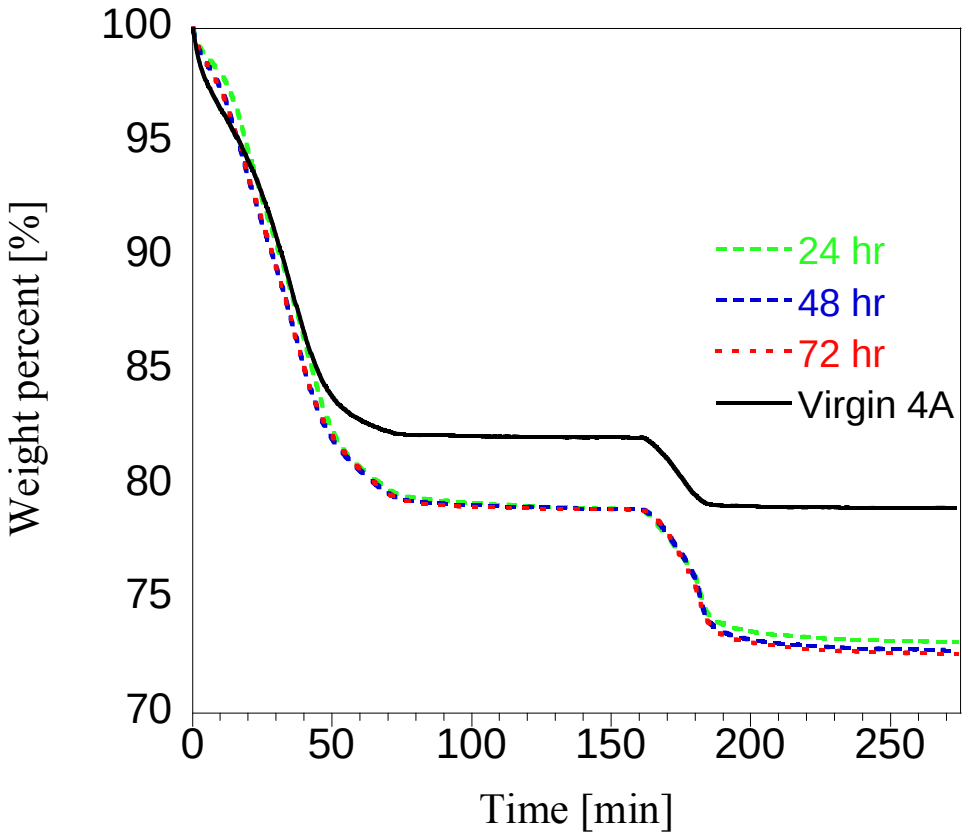

Fig. 4.1 TGA results of virgin zeolite 4A (solid line), treated zeolite 4A from A2 (green dashed line), A6 (blue dashed line), A10 (red dashed line).

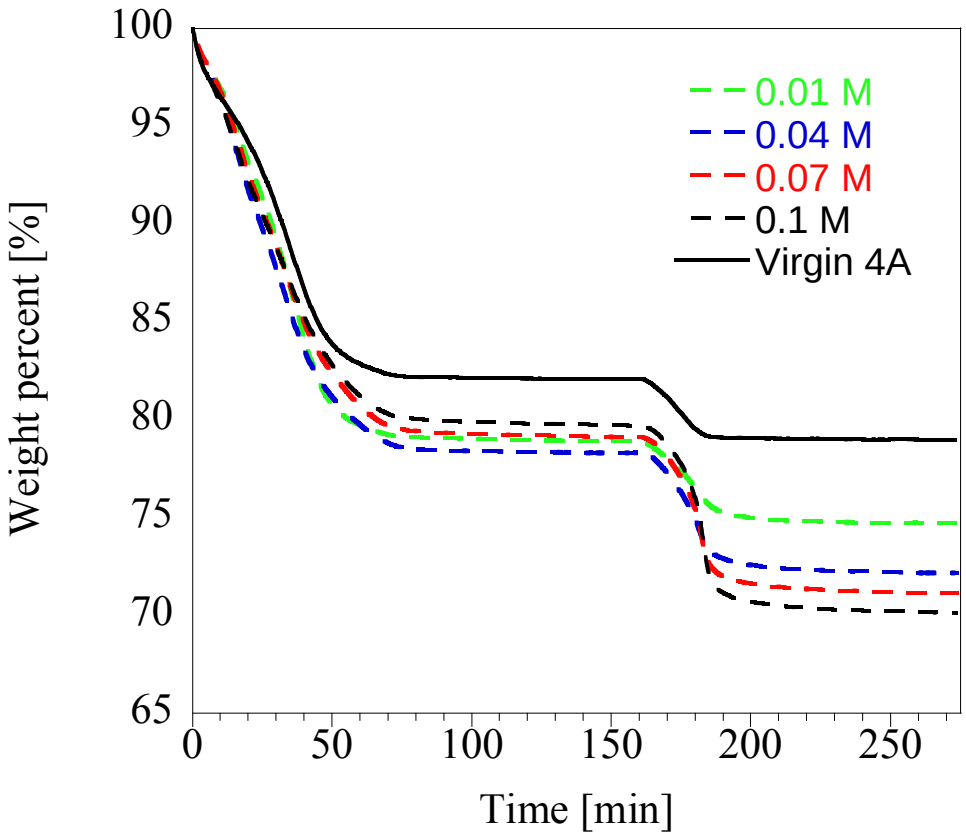

Fig. 4.2 TGA results of virgin zeolite 4A (solid line), treated zeolite 4A from A9 (green dashed line), A10 (blue dashed line), A11 (red dashed line), A12 (black dashed line).

4-1-3 Yield of $Mg(OH)_2$ during the deposition – precipitation process

During the synthesis of $Mg(OH)_2$ / zeolite 4A nanocomposites, the deposition of $Mg(OH)_2$ nanostructures on the zeolite 4A surfaces is most likely accompanied by the precipitation of $Mg(OH)_2$ in the bulk solution. In order to better control the synthesis of the nanocomposites, it is of practical interest to determine the yield of $Mg(OH)_2$ during the deposition – precipitation process. For example, the yield of $Mg(OH)_2$ in experiment A6 can be calculated as follows:

$$\text{Percentage yield of } Mg(OH)_2 = \frac{[W_{Mg(OH)_2,\,zeolite} + W_{Mg(OH)_2,bulk}] \times \dfrac{M_{Mg}}{M_{Mg(OH)_2}}}{W_i} \times 100\%$$

$$W_{Mg(OH)_2,zeolite} = Wt\%_{Mg(OH)_2-zeolite} \times W_{zeolite}$$

$$W_{Mg(OH)_2,bulk} = \left[W_i - W_f - \frac{W_{Mg(OH)_2,zeolite} \times M_{Mg}}{M_{Mg(OH)_2}} \right] \times \frac{M_{Mg(OH)_2}}{M_{Mg}}$$

where $W_{Mg(OH)2,zeolite}$, and $W_{Mg(OH)2,bulk}$ are the weight of $Mg(OH)_2$ deposited on the zeolite and the weight of $Mg(OH)_2$ precipitated in the bulk solution respectively, in g. $Wt\%_{Mg(OH)2\text{-}zeolite}$ (= 11.79 %) and $W_{zeolite}$ (= 0.2 g) are the weight percent of $Mg(OH)_2$ in the nanocomposites determined by TGA as presented in section 4-1-2 and weight of zeolite used in the preparation of the nanocomposite. W_i (= 0.01944 g) and W_f (= 0.005443 g) are the weight of free magnesium ions in the bulk solution at the beginning and at the end of the synthesis process. The weight of the magnesium ions in the solutions are determined by using an EDTA titration method (see chapter 5). M_{Mg} (= 24.3 g/mol) and $M_{Mg(OH)2}$ (= 58.3 g/mol) are the molecular weight of magnesium and

magnesium hydroxide respectively. The amount of $Mg(OH)_2$ deposited on the zeolite and in the bulk solution are 0.0236 g and 0.01 g respectively. Therefore, the percentage yield of $Mg(OH)_2$ in experiment A6 is 72 %. Approximately 30 % of the $Mg(OH)_2$ formed are precipitated in the bulk solution. This precipitation in the bulk solution may be driven by the addition of the zeolite or spontaneous precipitation of $Mg(OH)_2$ when ammonium hydroxide is mixed with magnesium chloride solution.

In order to better account for the effect of zeolite in $Mg(OH)_2$ formation, a zeolite free control study was carried out to determine the amount of $Mg(OH)_2$ precipitated by mixing only magnesium chloride and ammonium hydroxide solutions. The procedure of the control study is described in section 5-3-2-1 where the initial concentration of $MgCl_2$ is 0.04 M. The percentage yield of $Mg(OH)_2$ can be calculated as follows (assuming all of the Mg^{2+} ions consumed are precipitated as $Mg(OH)_2$):

$$\text{Percentage yield of } Mg(OH)_2 = \frac{(W_i - W_f)}{W_i} \times 100\%$$

where W_i (= 0.01944 g) and W_f (= 0.0167 g) are the weight of magnesium ions at the beginning and at the end of the synthesis process. Thus, the yield of $Mg(OH)_2$ in the absence of zeolite is 14 % which is approximately 0.00657 g.

By taking into consideration the spontaneous precipitation of $Mg(OH)_2$ in the zeolite free control study, the net amount of $Mg(OH)_2$ precipitated in the bulk solution induced by the zeolite in experiment A6 is roughly 0.00343 g (= 0.01 g – 0.00657 g), by assuming the equilibrium of the precipitation process does not vary much between the zeolite free control study and experiment A6. Therefore, approximately 65.7 % of the

$Mg(OH)_2$ precipitated in the bulk solution of experiment A6 was due to the spontaneous precipitation of $Mg(OH)_2$ caused by the mixing of ammonium hydroxide and magnesium chloride solutions. Roughly 7.4 % of the total magnesium ions added in experiment A6 was precipitated as $Mg(OH)_2$ in the bulk solution by zeolite. It is noted that this value may cause discrepancy in the adsorption isotherms presented in chapter 5 and should be taken into consideration when discussing the adsorption results.

4-2 Fabrication of hybrid membranes

The hybrid membranes were prepared according to the procedure established by Dr Koros's research group. The procedure is as follows: The Ultem® powder was dried under vacuum at 323 K for 24 h to remove water. 0.2 g of bare zeolite 4A was added to a 8 mL glass vial and placed in a vacuum oven. Under vacuum, the zeolites were activated overnight (~12 h) at 323 K, after which the oven was allowed to cool and purged with dry nitrogen gas. The vial was quickly removed and 4 g of dichloromethane (CH_2Cl_2) was added. The zeolites were then dispersed using a sonication bath (Branson Ultrasonics Corp., Danbury, CT) for 2 h. Once the zeolites were dispersed, a small amount of previously dried Ultem® powder was added to the vial. This addition, representing 1-3 % of the total Ultem® that was added to the polymer solution, served to prime the sieves. Priming is known to stabilize the dispersion and to improve membrane formation [8]. After priming, small amounts of dry Ultem® powder were added to the vial, followed by vigorous shaking until the polymer dissolved. This procedure was repeated until the required amount of polymer had been added to reach the desired zeolite loading (e.g., 3 %, 10%, 20 %, and 30% zeolite in Ultem® by weight). Once the required amount of Ultem® had been added and dissolved, the vial was placed on an axial roller overnight (12

– 24 h) to ensure homogenous mixing. The vial was subsequently removed from the roller and allowed to remain static in order to remove entrained air bubbles.

All membranes were cast in a controlled atmosphere established in a polyethylene glove bag. The glove bag was purged several times with dry argon gas to displace atmospheric water vapor. Several milliliters of dichloromethane were poured into an open glass petri dish which was placed in the glove bag. The glove bag was sealed to allow the CH_2Cl_2 to evaporate in order to saturate the local atmosphere. The membrane dope was then slowly poured onto a GlasClad®-treated (Gelest Inc., PA, USA) tempered glass plate. The dope was then draw-cast using a Bird film applicator with a gap of 100 μm (Elcometer, MI, USA). The membrane was allowed to vitrify in the glove bag for at least 24 h. At the end of the 24 h period, the membrane was delaminated from the plate and kept in a ziplock bag. The ziplock bag was then placed into a vacuum oven unlocked and evacuated at ~ -584 Torr at room temperature for at least one hour. The membrane was then annealed at 503 K under vacuum for 12 h prior to further characterization. The above procedure was repeated for membrane dispersed with magnesium hydroxide / zeolite 4A nanocomposite.

4-3 Thermal and mechanical properties of the hybrid membranes

4-3-1 *Glass transition temperature by differential scanning calorimetry (DSC)*

Differential scanning calorimetry (DSC) Q200 (TA Instruments, USA) was used to estimate the glass transition temperature (Tg) of the hybrid membranes. Approximately 5 mg of dried sample was transferred to 40 μL aluminum pans, which were hermetically sealed with aluminum covers. The samples were initially heated under an inert environment from 298 K to 573 K at 10 K/min, kept at 573 K for 5 mins before cooling down to 283 K at 20 K/min. During the second run, the temperature was kept at 283 K for 1 min before the temperature was raised again to 573 K at 10 K /min. The temperature was kept at 573 K for 1 min before cooling down. DSC curves were obtained during the second run and the Tg of each sample was obtained from the inflection point of the respective DSC curve. The glass transition temperatures of the Ultem® polymer composites are listed in Table 4-2.

Table 4-3 Glass transition temperature (Tg) of as prepared nanocomposite membranes

Sample	Glass transition temperature Tg (°C)
Neat Ultem®	216.7
Ultem® with 3 wt% bare zeolite 4A loading	215.9
Ultem® with 10 wt% bare zeolite 4A loading	215.1
Ultem® with 20 wt% bare zeolite 4A loading	216.4
Ultem® with 30 wt% bare zeolite 4A loading	216.6
Ultem® with 3 wt% treated zeolite 4A loading	216.0
Ultem® with 10 wt% treated zeolite 4A loading	216.4
Ultem® with 20 wt% treated zeolite 4A loading	216.8
Ultem® with 30 wt% treated zeolite 4A loading	216.8

4-3-2 *High-throughput dynamic impact characterization of polymer films*

The mechanical properties of the hybrid membranes were evaluated using a high-throughput impact analyzer designed and constructed in-house by Dr. Carson Meredith's research group. The high-throughput impact apparatus is shown in Fig. 4.3. The sample is enclosed between two stainless steel plates, perforated by a 10 × 10 grid of holes with a diameter of 3 mm and a distance of 1 mm between neighboring holes. The stainless steel plate provides uniform pressure on the sample, prevents slippage, and isolates the 100 individual impact sites during testing. The sample plates are mounted onto a ball bearing guide rail and an ultrasonic displacement sensor (Migatron RPS-401A-40, IL, USA) is used to measure the position of the sample as a function of time during the impact tests. The velocity is determined using a finite difference approximation for the first derivative. The samples are slowly lowered from a fixed height onto a hemispherical contact tip that

is positioned under the sample plate. The position of the tip is coordinated using an x, y translation stage (Newport 443 Series, CA, USA). The tip is embedded in a steep cap that is screwed onto a piezoelectric force sensor (Omega DLC101-10, CT, USA), which records the force on the tip during tests. The force versus time measurements were collected at 50,000 Hz using a data acquisition system (National Instruments, TX, USA). The mechanical properties (toughness and strain-at-break) of the Ultem® polymer composites are shown in Figs. 4.4 and 4.5 respectively.

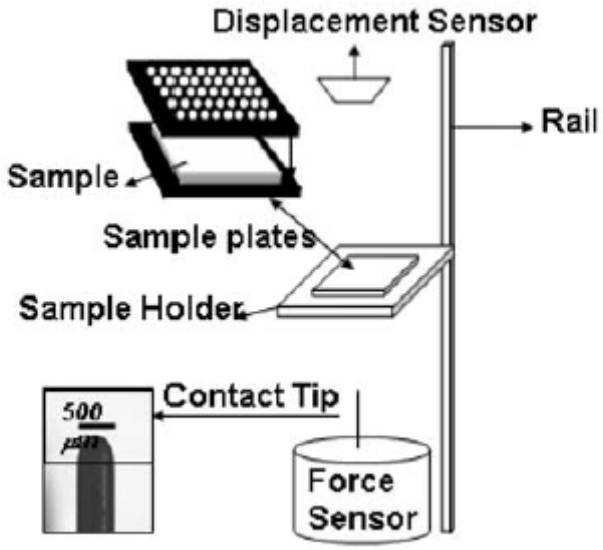

Fig. 4.3 Experimental setup of the high-throughput impact apparatus.

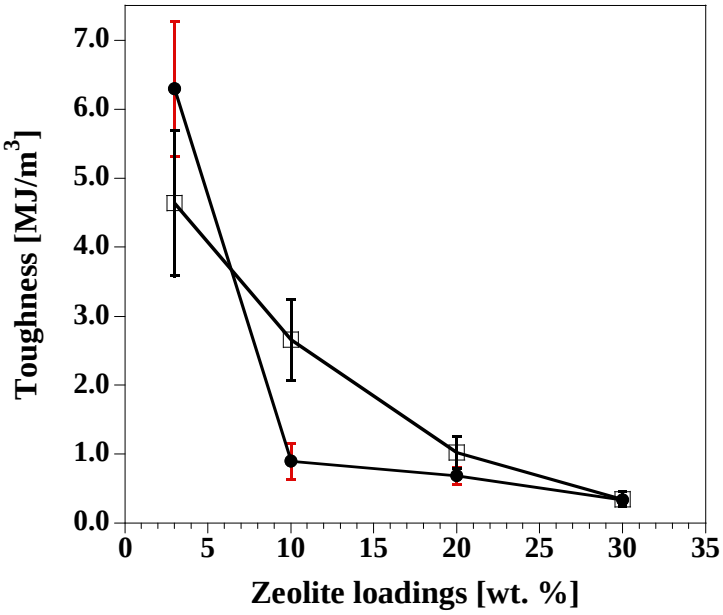

Fig. 4.4 Effect of bare and treated zeolite 4A loadings on the toughness of Ultem® composite. Solid circle (●) and open square (□) represent bare zeolite 4A and treated zeolite 4A respectively.

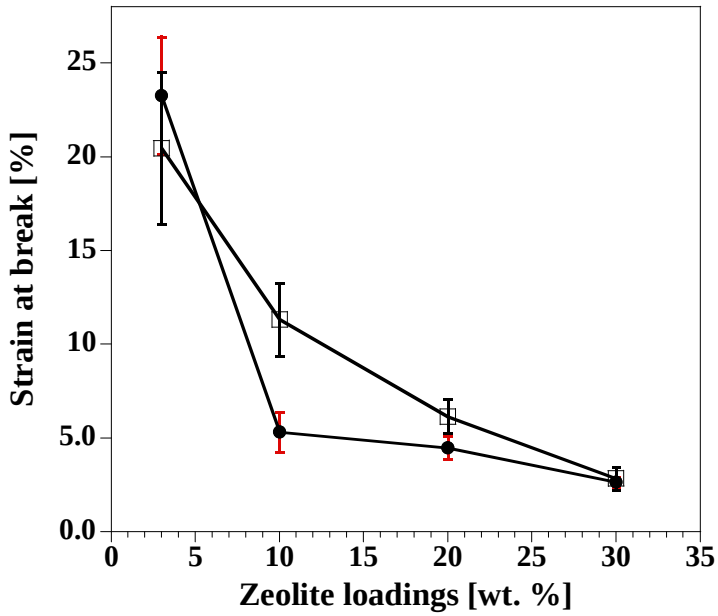

Fig. 4.5 Effect of zeolite loadings on the strain at break of Ultem® composite. Solid circle (●) and open square (□) represent bare zeolite 4A and treated zeolite 4A respectively.

4-4 Effects of the magnesium hydroxide nanostructures on interfacial adhesion

From above results, it can be seen that the addition of rigid zeolites into a glassy polymer such as Ultem® resulted in a decrease in the mechanical properties of the polymer. The Tg results suggest that Ultem® polymer loaded with bare zeolite has a higher free volume, therefore a lower glass transition temperature. It has been suggested that the reduction in Tg is due to non-adhering nanoparticles that act as well-dispersed internal void/polymer interfaces that break up the percolating structure of dynamically heterogenous domains that are responsible for the Tg reduction in polymer ultrathin films [9]. Therefore, it should be possible to prevent the suppression of Tg by surface treating the zeolite with $Mg(OH)_2$ nanostructures [2] (as shown in Table 4-2). These nanostructures increase the contact area for polymer adhesion [10]. Therefore, increasing the fraction of treated zeolite 4A in the polymer composite increases the total surface area available for entrapment of the polymer chains, thereby increasing the Tg of the resulting polymer composite. However, an increase in the zeolite loading in the polymer composite often promotes agglomeration of zeolites. Figure 4.6 shows the SEM images of Ultem® polymer composite loaded with 20 wt.% bare zeolite and treated zeolite respectively. It can be seen that although treated zeolites have a better interfacial adhesion with the polymer, large agglomerate are formed. Subsequently, such agglomerates behave like big particles which may cause the formation of interstitial voids between the particles and polymer (as shown in Fig. 4.6b). This observation is also corroborated by the toughness and strain-at-break values of the Ultem® polymer composite.

The toughness and strain at break for a pure Ultem® were 9.43 MJ/ m^3 and 33.4 %. Toughness is related to impact strength and indicates the energy that a material can

absorb before breaking. It is directly proportional to elongation at break (strain at break) [11]. On the other hand, strain at break is governed by the energy required to orient and stretch the polymer in the direction of the applied load. As shown in Figs. 4.4 and 4.5, the mechanical properties of the Ultem® polymer composites are lower than those of pure Ultem® and in general, Ultem® loaded with treated zeolite 4A has better mechanical properties than bare zeolite 4A. Overall, the toughness and strain-at-break of the Ultem® polymer composites decreased with increasing zeolite loading. At higher zeolite concentrations, toughening was not very efficient, probably because of the agglomeration of zeolite particles which caused weak interfacial adhesion. It is well known that strong interfacial adhesion leads to greater toughness and strain-at-break in composite matrices because of more efficient force distribution [12]. Less energy is dissipated in overcoming the intramolecular forces of the rigid polymer and more energy is available to stretch the polymer [13]. Because of better interfacial adhesion between the zeolite and polymer in the Ultem® polymer composite loaded with treated zeolite 4A, less energy is required to re-orient the zeolites in the direction of elongation and more energy is available to stretch the polymer before breaking. Therefore, high strain-at-break values were obtained with Ultem® polymer composites loaded with treated zeolite 4A.

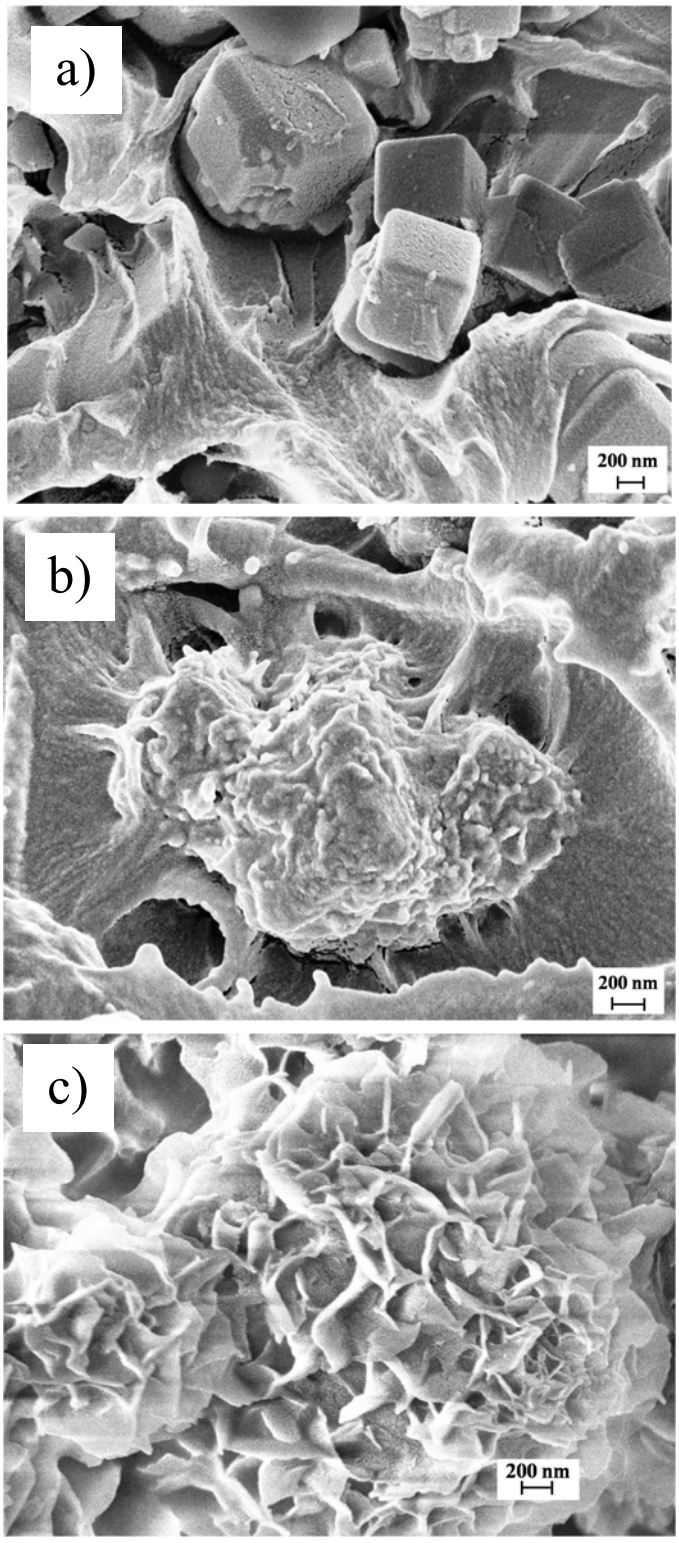

Fig. 4.6 Representative SEM images of Ultem® polymer nanocomposites loaded with (a) 20 wt% bare zeolite 4A, (b) 20 wt % treated zeolite 4A, and (c) treated zeolite 4A obtained from experiment A10.

4-5 Conclusions

The BET analysis indicates that the pores of the $Mg(OH)_2$ / zeolite nanocomposite were not plugged. This suggests that the $Mg(OH)_2$ nanostructures grow mainly on the external surface of the zeolite. The TGA measurements show that the composition of the nanocomposite can be effectively controlled by varying the concentration of magnesium chloride/ ammonium hydroxide and synthesis time. It was found that the glass transition temperature, toughness, and strain-at-break properties of the hybrid membranes decreased overall with the addition of the zeolites. However, some of the adverse effects could be mitigated by depositing $Mg(OH)_2$ nanostructures on the zeolite surface.

4-6 References

1. Koros, W.J., G.K. Fleming, S.M. Jordan, T.H. Kim, and H.H. Hoehn, *Polymeric membrane materials for solution-diffusion based permeation separations.* Progress in Polymer Science, 1988. **13**(4): p. 339-401.

2. Shu, S., *Engineering the performance of mixed matrix membranes for gas separations*. 2007, Georgia Institute of Technology: United States -- Georgia. p. 251.

3. Lippens, B.C. and J.H. de Boer, *Studies on pore systems in catalysts : V. The t method.* Journal of Catalysis, 1965. **4**(3): p. 319-323.

4. *Introduction to zeolite science and practice*. 3rd rev. ed. ed. Studies in surface science and catalysis ;, ed. J. Čejka. 2007, Amsterdam ;: Elsevier.

5. *Verified syntheses of zeolitic materials*. 2nd rev. ed. ed, ed. H.E. Robson. 2001, Amsterdam ;: Elsevier.

6. Yan, L., J. Zhuang, X. Sun, Z. Deng, and Y. Li, *Formation of rod-like $Mg(OH)_2$ nanocrystallites under hydrothermal conditions and the conversion to MgO nanorods by thermal dehydration.* Materials Chemistry and Physics, 2002. **76**(2): p. 119-122.

7. Choudhary, V.R., S.G. Pataskar, M.Y. Pandit, and V.G. Gunjikar, *Influence of precipitation conditions of magnesium hydroxide on its thermal decomposition in the preparation of active MgO.* Thermochimica Acta, 1992. **194**: p. 361-373.

8. Mahajan, R. and W.J. Koros, *Factors controlling successful formation of mixed-matrix gas separation materials.* Industrial & Engineering Chemistry Research, 2000. **39**(8): p. 2692-2696.

9. Ash, B.J., A. Eitan, and L.S. Schadler, *Polymer nanocomposites with particle and carbon nanotube fillers.* Dekker Encyclopedia of Nanoscience and Nanotechnology, 2004: p. 2917 - 2930.

10. Bae, T.H., J.Q. Liu, J.S. Lee, W.J. Koros, C.W. Jones, and S. Nair, *Facile high-yield solvothermal deposition of inorganic nanostructures on zeolite crystals for mixed matrix membrane fabrication.* Journal of the American Chemical Society, 2009. **131**(41): p. 14662-14663.

11. García, M.G., J. Marchese, and N.A. Ochoa, *Effect of the particle size and particle agglomeration on composite membrane performance.* Journal of Applied Polymer Science, 2010. **118**: p. 2417-2424.

12. Tjong, S.C., *Structural and mechanical properties of polymer nanocomposites.* Materials Science and Engineering: R: Reports, 2006. **53**(3-4): p. 73-197.

13. *Polymeric materials encyclopedia*, ed. J.C. Salamone. 1996, Boca Raton :: CRC Press.

CHAPTER 5

ADSORPTION AND SURFACE PRECIPITATION STUDIES OF $Mg(OH)_2$ ON ZEOLITE SURFACES

5-1 Introduction

In this chapter, the deposition of $Mg(OH)_2$ on zeolite 4A is investigated via adsorption isotherms. Zeolite 4A was dispersed into a solution of magnesium chloride and ammonium hydroxide of different concentrations (this is termed the magnesium hydroxide – zeolite system in this chapter) and the adsorption was measured via an EDTA titration method. The adsorption isotherms provide a macroscopic description of $Mg(OH)_2$ formation and loading on the zeolite surface. It is hypothesized that, depending on the Mg^{2+} ions concentration and pH of the solution, the deposition of $Mg(OH)_2$ on zeolite will involve ion exchange, surface adsorption of Mg^{2+} ions, and surface precipitation of $Mg(OH)_2$. In order to distinguish between these adsorption mechanisms, adsorption on ion-exchanged zeolite and virgin zeolite 4A dispersed in magnesium chloride solution were studied. These systems are termed magnesium ion – ion exchanged zeolite and magnesium ion – zeolite systems respectively. Ion – exchanged zeolite refers to zeolite 4A that was previously treated with 1 M of magnesium chloride solution. This was done in order to replace the Na^+ ions in the zeolite with Mg^{2+} ions. When most of the Na^+ ions in the pores of the zeolite have been replaced by Mg^{2+} ions, the adsorption mechanism should be surface adsorption of Mg^{2+} ions. On the other hand, it is expected that the predominant adsorption mechanism in the magnesium ion – zeolite system would be ion exchange and surface adsorption of Mg^{2+} ions. The pH change in

these three systems is closely examined in order to elucidate its effect on the adsorption process.

5-2 Literature review

Adsorption isotherms can be classified according to their initial slopes. The four main classes, which are shown in Fig. 5.1, are named the *S*, *L* ("Langmuir" type), *H* ("high affinity"), and *C* ("constant partition") isotherms, and the variations in each class are divided into sub-groups [1]. Sub-groups for each class are based on the shapes of the upper parts of the curves. [1-3]. In an adsorption process, an adsorbate refers to the material that accumulates at an interface, and the solid surface on which the adsorbate accumulates is referred to as the adsorbent [4]. An adsorptive refers to the molecule or ion in solution that has the potential of being adsorbed [4].

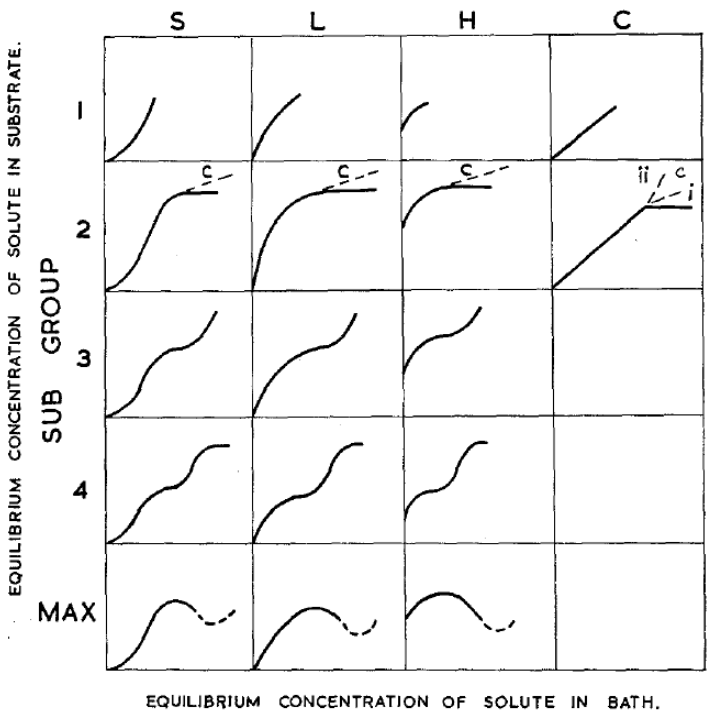

Fig. 5.1 Classification of isotherms: S-type, L-type, H-type, and C-type. The 2c subgroup indicates microporosity in the substrates, and in the C-class, the second branch of the curve in the subgroup 2 may be horizontal, or have a slope of different steepness that the main portion, according to the nature of the system. Adapted from [1].

An S-type isotherm is characterized by an initially small slope that increases with adsorptive concentration. This indicates that at low concentration, the affinity of the solid substrate for the adsorbate is less than that of the adsorbent solution for the adsorptive. The S-type isotherm suggests that the adsorbate-adsorbate interaction is stronger than adsorbate-adsorbent interaction [1, 3]. Therefore, clustering of adsorbate molecules at the surface is favored because adsorbate molecules bond more strongly with one another than with the surface [1, 2]

An L-type isotherm is characterized by a concave initial region. It represents systems in which there is a relatively high affinity between the adsorbate and the adsorbent [1]. The initial slopes show that as more sites in the solid substrate are filled, it becomes increasingly difficult for the solute to find a vacant site.

An H-type isotherm represents an extreme version of the L-type isotherm and is characterized by a large initial slope. The H-type isotherm indicates very strong adsorbate-adsorbent interaction, caused either by specific interactions between the solid phase and the adsorbate or by significant van der Waals interactions in the adsorption process [5]. In this case, the solute has such high affinity that in dilute solutions it is completely adsorbed, or at least there is no measurable amount remaining in solution. The adsorbed species are often large units such as ionic micelles, or single ions which exchange with others of much lower affinity for the surface [3]. Sub-groups 4 and 5 have been obtained by Tamamushi et al. [3, 6, 7] and Giles et al. [1-3, 8] respectively. Tamamushi et al. [7] reported that the adsorption of sodium dodecyl sulphate on an anion-exchange resin Dowex 1, and X-1 gives an H-type sub-group 4 isotherm and the adsorption process is considered to be the superposition of the ion-exchange type and the van der Waals adsorption type. Similar isotherms were also obtained when birnessite (δ-$MnO_{1.7}$) and manganite (γ-MnOOH) were used as adsorbents for lead ions [9]. On the other hand, an H-type sub-group 5 isotherm was obtained in the adsorption of cationic dyes such as Crystal Violet ($C_{25}H_{30}N_3Cl,1.5H_2O,0.5HCl,0.05NaCl$) and Victoria pure Blue BO ($C_{33}H_{40}N_3Cl,HCl$) on alumina [8]. The fall in the slope of the isotherm after the first inflection is probably due to association of the solute in solution [3]. As the solute concentration increases, the solute-solute attraction begins to increase more rapidly than the substrate-solute attraction [3]. Thus, the adsorption density decreases at high solute concentration.

The C-type isotherm is characterized by the constant partition of solute between solution and substrate, right up to the maximum possible adsorption, where an abrupt

change to a horizontal plateau occurs [3]. This type of isotherm is produced either by a proportionate increase in the amount of adsorbing surface as the amount adsorbed increases or by a constant partitioning of a substance between the interfacial region and the solute solution [5].

In this chapter, adsorption isotherms for the deposition of magnesium hydroxide on zeolite 4A were measured and compared with these four classes of isotherms in order to determine the nature of interaction (chemisorption vs physisorption) between magnesium hydroxide and zeolite.

5-3 Experimental

5-3-1 *Materials*

Magnesium chloride ($MgCl_2.6H_2O$, ACS reagent), ammonium hydroxide (NH_4OH, ACS reagent), ammonium chloride (NH_4Cl, ACS reagent), and sodium hydroxide (NaOH, ACS reagent) were purchased from Fischer Scientific (NJ, USA). (Ethylenedinitrilo)tetraacetic (EDTA) disodium salt dihydrate was purchased from J.T. Baker (NJ, USA). Calmagite indicator 0.1% (w/ v) aqueous solution was purchased from Ricca Chemical Company (TX, USA). ADVERA 401P hydrated sodium zeolite 4A with a characteristic 3 – 6 μm cubic form was purchased from PQ Corporation (PA, USA). Deionized water was made in the lab and all materials were used without further purification.

5-3-2 *Procedure*

Magnesium chloride and ammonium hydroxide solutions of concentrations ranging from 0.01 M to 0.12 M were prepared by adding deionized water to known mass of $MgCl_2.6H_2O$ and NH_4OH to make 20 mL and 60 mL of equimolar magnesium chloride and ammonium hydroxide solutions respectively. 50 mL of pH 10 buffer was prepared by dissolving 3.75 g of NH_4Cl to 28.5 mL of concentrated NH_4OH, followed by addition of 21.5 mL of deionized water.

5-3-2-1 ***Control study***

Zeolite 4A is known to hydrolyze in aqueous solution and releases hydroxide ions, which may affect the deposition of magnesium hydroxide. The hydrolysis of zeolite 4A in aqueous solution can be expressed as [10]:

$$NaA + (H_2O)_x \leftrightarrow HA + (H_2O)_{x-1} + Na^+ + OH^-$$

A control study was carried out with a solution of magnesium chloride and ammonium hydroxide in the absence of zeolite 4A in order to determine the amount of $Mg(OH)_2$ precipitated in the bulk solution. The control study was carried out as follows: 1) 20 mL of magnesium chloride solution of known concentration (ranging from 0.01 M to 0.12 M) was prepared; 2) 60 mL of ammonium hydroxide solution of equivalent concentration to that of magnesium chloride prepared was titrated to above magnesium chloride solutions with stirring; 3) the solution was allowed to sit at ambient conditions for 96 h; 4) a 1-3 mL aliquot was collected from each of the magnesium chloride and ammonium hydroxide solution every 24 h; 5) 0.5 mL of $NH_3 – NH_4Cl$ buffer and 2 drops of Calmagite indicator (red color) were added to each aliquot; 6) 0.001 M of EDTA

solution was titrated into the aliquot until the color of the aliquot solution changed from red to blue (Note: a 0.0001 M EDTA titrant was used in determining the concentration of Mg^{2+} in the 0.01 M magnesium chloride and 0.01 M ammonium hydroxide solution for better accuracy). The amount of $Mg(OH)_2$ precipitated in the magnesium chloride and ammonium hydroxide solution was taken into consideration when determining the amount of free Mg^{2+} ions in the batch adsorption experiments.

5-3-2-2 ***Batch adsorption experiments***

The batch adsorption experiments were carried out as follows: 1) 20 mL of magnesium chloride solution ranging from 0.01 M to 0.12 M was prepared by adding deionized water to a known mass of $MgCl_2.6H_2O$ salt, 2) 0.2 g of zeolite 4A was added to each of the magnesium chloride solutions, 3) 60 mL of NH_4OH solution of equivalent concentration to the magnesium chloride solution prepared was titrated slowly into each of the zeolite mixtures whilst stirring, 4) the final mixtures were allowed to sit at ambient conditions for 96 h, 5) approximately 1-5 mL aliquot was collected from each mixture at every 24 h interval, 6) 0.5 mL of $NH_3 – NH_4Cl$ buffer solution and 2 drops of Calmagite indicator were added to the aliquot, and finally 7) 0.001 M of EDTA solution was titrated into the aliquot solution until the color of the aliquot solution changed from red to blue (Note: 0.0001 M of EDTA was titrated with the aliquots collected from 0.01 M magnesium chloride and ammonium hydroxide solutions for better accuracy).

5-3-3 *Sample analysis*

At the conclusion of the adsorption studies, zeolite particles from selected experiments were collected via vacuum filtration through a cellulose nitrate membrane

filter of pore size 0.2 μm. The particles were subsequently washed with an excess of deionized water and dried overnight in a vacuum oven at 323 K. A small amount of the particles was sampled for examination by scanning electron microscopy (SEM).

The SEM sample was examined using a LEO 1530 FEG field-emission instrument (Carl Zeiss SMT Inc., Germany) equipped with an energy dispersive X-ray spectroscope (EDS). Powder X-ray diffraction (XRD) patterns were obtained on a Philips X'pert diffractometer (PANalytical Inc, USA) equipped with X'celerator using Cu Kα radiation.

5-4 Results and discussion

5-4-1 *Determination of the degree of adsorption*

The magnesium hydroxide precipitated per unit volume of solution in the zeolite free control study was calculated using the following equations

$$C_{Mg} = \frac{V_{EDTA} \times C_{EDTA}}{V_{aliquot}}$$

$$C_{Mg(OH)_2} = C_{Mg,i} - C_{Mg}$$

where $C_{Mg,i}$ and C_{Mg} are the concentrations of Mg^{2+} at the start of the control study and at the end of the time interval respectively, in mmol mL^{-1}. V_{EDTA} and $V_{aliquot}$ are the volume of EDTA required to change the color of the solution from red to blue, and the volume of the aliquot solution titrated with EDTA, respectively, in mL. $C_{Mg(OH)2}$ and C_{EDTA} are the amount of magnesium hydroxide precipitated per unit volume of the solution and concentration of EDTA respectively, in mmol mL^{-1}. The concentration of EDTA used in

this study was 0.001 mmol mL^{-1} unless stated otherwise. The degree of adsorption in the batch experiments was calculated using the following equations

$$q = \frac{(C_0 - C_{Mg(OH)_2}) - C_f}{m}$$

$$C_f = \frac{V_{EDTA} \times C_{EDTA}}{V_{aliquot}}$$

where q is the amount of adsorption (adsorbate per unit mass of adsorbent) in mmol mg^{-1}, C_0 and C_f are the initial and final magnesium ion concentrations, respectively, in mmol mL^{-1}, $C_{Mg(OH)2}$ is the concentration of magnesium hydroxide precipitated in the absence of adsorbent (zeolite), in mmol mL^{-1}, and m (= 2.5) is the concentration of adsorbent in mg mL^{-1}.

5-4-2 *Adsorption isotherms*

Figure 5.2 depicts the adsorption isotherms of magnesium hydroxide adsorb onto zeolite 4A at different contact times. The isotherms exhibit similar trends at different contact times and the shapes of the adsorption curves resemble an H-type isotherm (see section 5-2). This implies that there may be specific interactions between the adsorbate and the adsorbent. Similar isotherms were also obtained by Komárek et al. [11] in the retention of Cu in contrasting soil types (Leptosol, Chernozem, and Cambisol). The authors reported that the retention mechanisms of Cu on the soils may include specific and non-specific adsorption, as well as precipitation of newly formed Cu phases such as CuO, $Cu(OH)_2$, $Cu_2(OH)_3NO_3$, and $CuCO_3/Cu_2(OH)_2CO_3$. It was postulated that at low copper concentrations, the retention process is probably controlled by high selectivity sorption sites, in which adsorption is the main process [11]. As Cu concentration

increases, selective sorption sites become saturated and metal sorption takes place at low selectivity cation exchange sites [11]. Finally, at high initial Cu concentrations, the precipitation of newly formed Cu compounds on the adsorbent becomes an important retention mechanism [11, 12].

In Fig. 5.2, the adsorption density (q) increased rapidly at low concentrations of Mg^{2+} ions, attained a short plateau, and then increased until another plateau was achieved. The adsorption isotherms of zeolite 4A exhibit 4 regions of interest. The first region (region I), characterized by a sharp rise in adsorption, indicates that ion exchange between magnesium ions and exchangeable sodium ions in the zeolite is likely. Depending on the pH and magnesium ion concentration, this ion exchange process is likely to be accompanied by precipitation of magnesium ion hydroxide complexes on hydroxyl groups of the zeolite surface. Similar results were reported for lead and chromium elsewhere [13-16]. Since the initial pH of the zeolite solution was above 10, precipitation of magnesium hydroxide is favored [17, 18]. However, only a very small amount of magnesium hydroxide was found to precipitate and adsorb on the surface of zeolite as shown in Fig. 5.3. In region I, as the contact time increased to 48 h, the adsorption density reached saturation and further increase in contact time has no effect on the adsorption density. At 24 h, ion exchange and surface adsorption of magnesium ions are likely along with very little surface precipitation of magnesium hydroxide.

The second region (region II) marks the onset of the plateau region where the adsorption density (q) remained nearly constant before the onset of the third region. This plateau marks the completion of a “monolayer” in which all the hydroxyl groups on zeolite 4A are occupied by magnesium hydroxide or magnesium ions. The plateau length

decreased as the contact time increased. It is known that adsorption of ionic micelles gives isotherms with long plateaus; in this case ionic micelles on the surface repel other micelles holding the same charge [1-3]. This might be the case here with the adsorption of magnesium ions at 24 h. The adsorbed magnesium ions repel the positively charged magnesium ions in the solution resulting in a long plateau. The long plateau implies that a high energy barrier has to be overcome before additional adsorption can occur on the next site, after the surface has been saturated [3]. Magnesium ions may have higher affinity for the solvent, but low affinity for the layer of magnesium ions already adsorbed. A short plateau means that the adsorbed solute molecules expose a surface which has nearly the same affinity for more solute as the original surface had [1-3]. This could be due to the nucleation and growth of magnesium hydroxide crystals on the magnesium hydroxide nuclei that were adsorbed on the zeolite surface. It has been reported that the formation of a homogenous solid on a surface can occur from a chemisorption-precipitation continuum, i.e when adsorption reaches monolayer coverage sorption continues on the newly created sites resulting in a precipitate on the surface (multilayer surface coverage) [4, 5]. From Fig. 5.2, it can be seen that the adsorption density in region II reached equilibrium within 72 h. Therefore, region II could represent the ideal region for the formation of magnesium hydroxide on zeolite surfaces without excessive precipitation or intergrowth between magnesium hydroxide nanostructures.

The third region (region III) is characterized by another sharp rise in adsorption density. In this region, the surface precipitation of magnesium hydroxide was more accentuated due to a higher concentration of magnesium ions. Also, it can be seen that the adsorption density in region III increased with increasing contact time implying a

continuous growth of magnesium hydroxide crystals over time. As the concentration of magnesium ions is increased beyond region III, it is seen that the adsorption isotherm reaches a second plateau (region IV). Within this region, the growth rate of magnesium hydroxide nanostructures is independent of the concentration of magnesium ions because of a very high supersaturation level of magnesium ions.

Figure 5.3 displays SEM images of the products obtained from region I through IV at 24 h contact time. From this figure, it can be seen that the amount of magnesium hydroxide nanostructures deposited on the zeolite surface increased with increasing magnesium ion / ammonium hydroxide concentration. Figure 5.4 shows the XRD patterns of the zeolites obtained from region I through IV. The zeolite structure and crystallinity remained intact after treatment. The peaks from nanocrystals created after treatment were well matched with tabulated magnesium hydroxide peaks. The formation of a stable precipitate nucleus involved bringing together a sufficient number of magnesium hydroxide molecules to form a nucleus of critical size [19]. Therefore, with the addition of ammonium hydroxide, a large quantity of magnesium hydroxyl species would be generated and would tend to ease the diffusion supply problem, facilitating formation of a critical nucleus. This is also supported by SEM images shown in Fig. 5.3. At low magnesium ion / ammonium hydroxide concentration, little to no magnesium hydroxide nanostructures were formed on the zeolite surface and the quantity of deposited magnesium hydroxide nanostructure increased with increasing magnesium ion / ammonium hydroxide concentration (Fig. 5.3a – d).

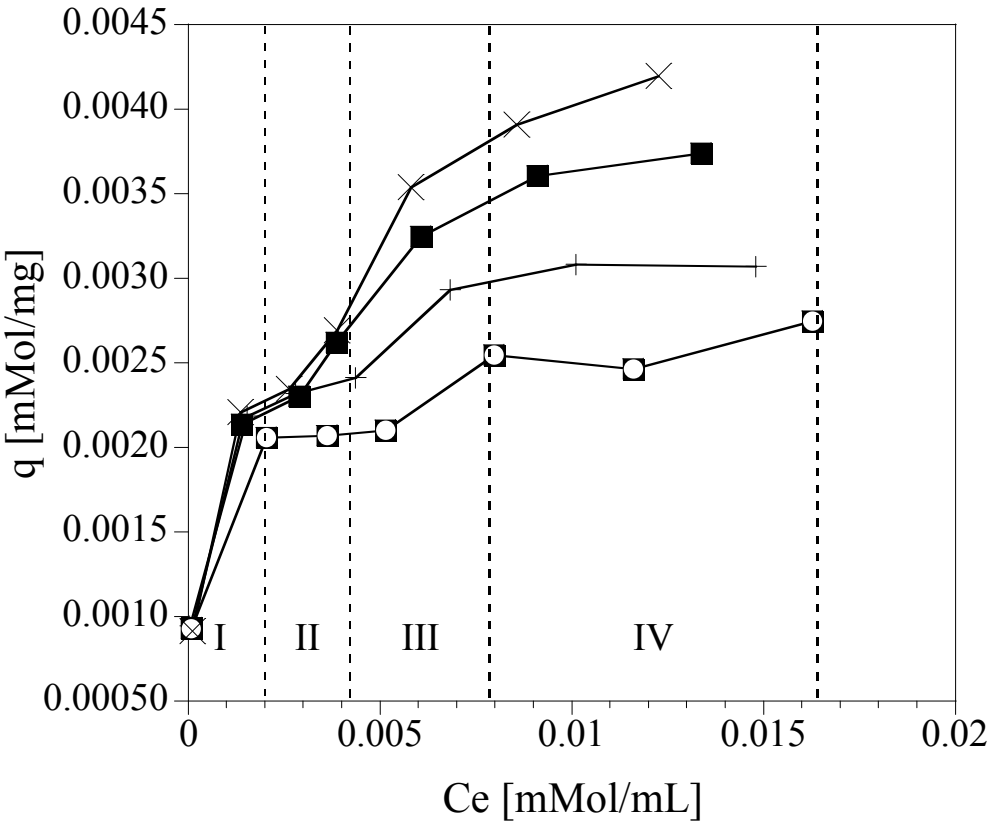

Fig. 5.2 Adsorption isotherms for Mg^{2+} ions on/in virgin zeolite A in the presence of ammonium hydroxide at different contact times: (◘) 24 h, (+) 48 h, (■) 72 h, and (X) 96 h.

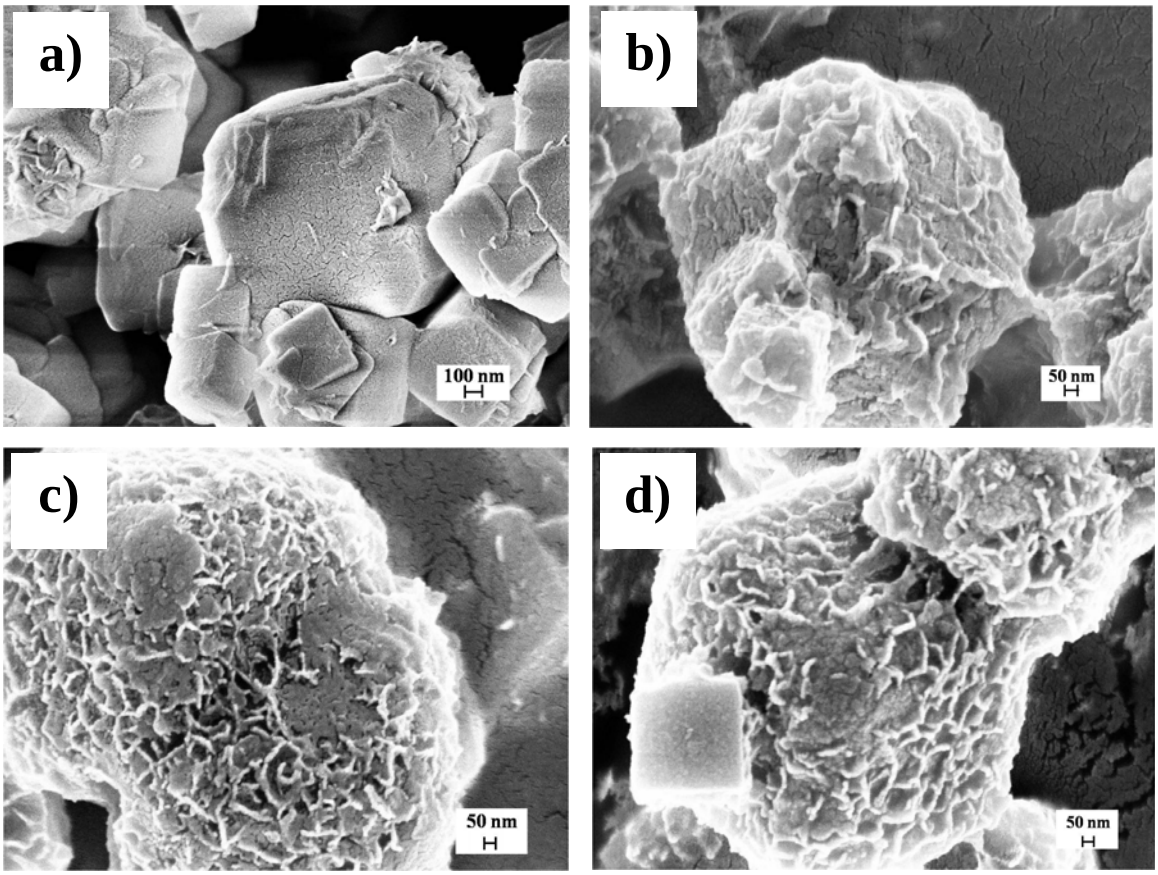

Fig. 5.3 Adsorption and precipitation of magnesium ions/ hydroxides onto zeolite A at 24 h obtained at 4 regions of interest: (a) region I, (b) region II, (c) region III, and (d) region IV.

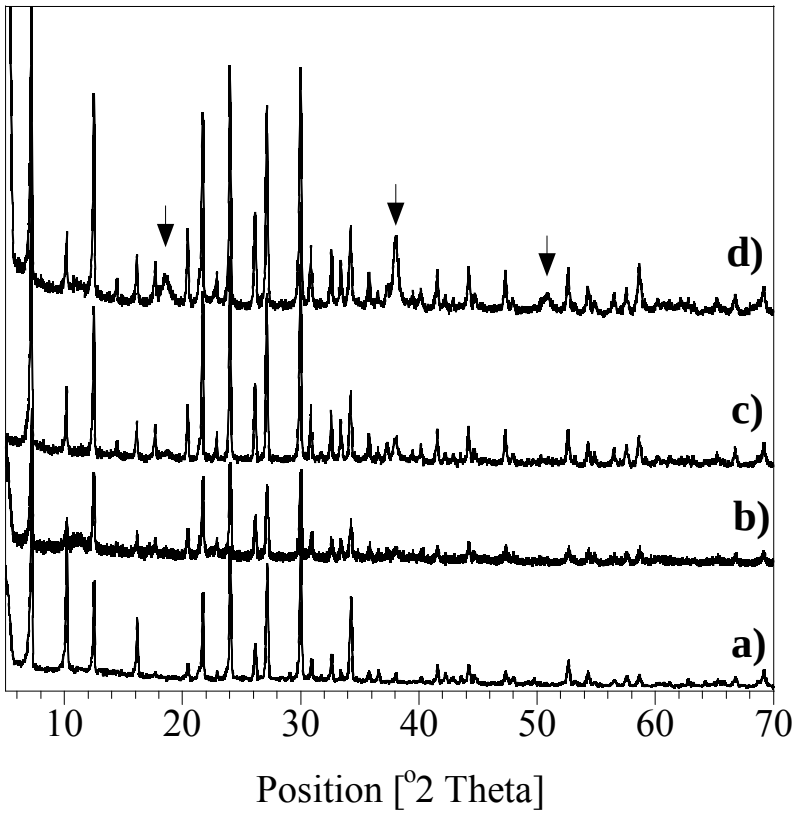

Fig. 5.4 XRD patterns of zeolites obtained from regions a) I, b) II, c) III, and d) IV. The peaks from nanocrystals created after treatment were well matched with tabulated $Mg(OH)_2$ peaks.

From the above discussion, it may be summarized that the zeolite is negatively charged and exhibits cation adsorption capacity because the solution pH (see Fig 5.6) is higher than the zeolite isoelectric point (IEP ~ 8.2) [20]. The first region probably represents electrostatic adsorption of the magnesium ions on/ in the zeolite support along with ion exchange between magnesium ions and sodium ions. As the amount of magnesium ions adsorbed on/ in the zeolite surface increases, adsorption proceeds from mononuclear adsorption to surface precipitation (region II). The magnesium hydroxide nuclei close to the zeolite surface can react with the zeolite surface hydroxyl groups via hydrolytic adsorption [21], which is a heterocondensation reaction between surface

hydroxyl $S_{surface}$ –OH and Mg –OH and leads to the formation of $S_{surface}$ – O – Mg bonds. In addition, the magnesium hydroxide complexes can react with each other via an olation reaction to form magnesium hydroxide sheets [22, 23]. The surface precipitation of magnesium hydroxide becomes more accentuated in region III and subsequently at high enough magnesium ion concentration, the growth rate of the precipitated magnesium hydroxide became independent of the magnesium ion concentration (region IV).

It can be concluded that the adsorption / precipitation process is to a large extent dependent on the concentration of magnesium ions and the pH of the solution. Furthermore, it is deduced that the adsorption process involves three mechanisms: ion exchange, surface adsorption of Mg^{2+} ions, and surface precipitation of $Mg(OH)_2$. The pH of the aqueous solution is an important controlling parameter in the adsorption / precipitation process and adsorption typically increases with increasing pH values [24]. Depending on the pH and metal concentration, Mg^{2+} ions may form complexes with OH^- at higher pH values, and as a result Mg-hydroxyl species may participate in the adsorption and precipitation onto the zeolite structure [16].

In order to distinguish between different adsorption mechanisms and the effect of ammonium hydroxide on the adsorption and precipitation of $Mg(OH)_2$ on zeolite surfaces, adsorption isotherms were measured for the virgin zeolite and also for ion – exchanged zeolite (zeolite that was previously treated with 1 M magnesium chloride solution) in the absence of ammonium hydroxide. These systems were termed magnesium ion – zeolite and magnesium ion – ion exchanged zeolite systems respectively and compared with the magnesium hydroxide – zeolite system. It is hypothesized that the predominant adsorption mechanism in the magnesium ion – ion

exchanged zeolite system is surface adsorption of Mg^{2+} ions since most of the Na^{+} ions if not all in the zeolite have been replaced by Mg^{2+} ions during the pretreatment process. On the other hand, the predominant adsorption mechanisms in the magnesium ion – zeolite system are expected to be ion exchange and surface adsorption of Mg^{2+} ions. Finally, we expect all these processes of ion exchange, surface adsorption of Mg^{2+}, and surface precipitation of $Mg(OH)_2$ to be involved in the magnesium hydroxide – zeolite system.

Figure 5.5 illustrates the adsorption isotherms of magnesium hydroxide – zeolite, magnesium ion – zeolite, and magnesium ion – ion exchanged zeolite systems at 72 h. The studies described in the previous section identified region II of the adsorption isotherm as the ideal region for the formation of magnesium hydroxide on zeolite surfaces, and also showed that adsorption reached saturation in 72 h. Therefore, 72 h was chosen as the standard contact time for this study.

From Fig. 5.5, it can be seen that the adsorption isotherms of these three systems differ significantly from each other. The adsorption density of the magnesium ion – ion exchanged zeolite system was significantly lower than the magnesium hydroxide – zeolite and magnesium ion – zeolite systems. This is because in dilute solution of magnesium ion, the ion exchanged zeolite hydrolyzed by exchanging magnesium ions for hydronium ions from water. The hydrolysis reaction of a zeolite in the magnesium form can be written as:

$$\mathrm{MgA} + 2(\mathrm{H_2O})_x \leftrightarrow x\mathrm{H_3O^+A} + \mathrm{Mg^{2+}} + x\mathrm{OH^-}$$

where MgA refers to the ion exchanged zeolite. This hydrolysis might produce significant amounts of magnesium ions, thereby reducing the adsorption capacity of the

magnesium ion – ion exchanged zeolite system and resulted in an apparent negative adsorption density at low Mg^{2+} ions concentration. Similar results have been reported by Harjula et al. [25] who showed that greater amount of calcium ions were detected when CaY zeolite was added to trace calcium solutions. In dilute solutions, hydrolysis of the zeolite essentially controlled the concentration of the ions in solution [25-27]. However, as the concentration of the magnesium ion increased, the adsorption density of the magnesium ion – ion exchanged zeolite system increased as well. This increase in adsorption density may be attributed to surface adsorption of Mg^{2+} ions. Magnesium ions are bonded to the surface functional groups via electrostatic bonding and are free to move around. However, this increase in adsorption density was negligible compare to the magnesium hydroxide – zeolite and magnesium ion – zeolite systems.

The pH change in the magnesium hydroxide – zeolite, magnesium ion – zeolite, and magnesium ion – ion exchanged zeolite systems were closely examined to determine the effect of pH on the adsorption and deposition of Mg^{2+} ions and $Mg(OH)_2$. Figure 5.6 shows the pH of magnesium hydroxide – zeolite, magnesium ion – zeolite, and magnesium ion – ion exchanged zeolite systems at 72 h. It can be seen from Fig. 5.6 that the magnesium ion – zeolite system stabilized at pH values within the basic pH range. It has been reported in the literature that the isoelectric point of zeolite NaA is ~ 8 [20], therefore, the $\equiv Si\text{-}O^-$ and $\equiv Al\text{-}O^-$ groups of the zeolite A predominated, giving the surface a net negative charge which is available to adsorb Mg^{2+} from solution [24], resulting in a higher adsorption capacity than the magnesium ion – ion exchanged zeolite system shown in Fig. 5.5. In addition, this process is most likely accompanied by the ion exchange process between Mg^{2+} ions and Na^+ ions in the zeolite. On the other hand, the

ion exchanged zeolite in magnesium chloride solution stabilized at pH value close to neutral (see Fig. 5.6) and thus it is expected to carry less negative surface charge. Consequently, the adsorption capacity of the ion exchanged zeolite is lower.

Figure 5.7 shows SEM images of zeolites obtained from magnesium ion – zeolite and magnesium ion – ion exchanged systems at initial magnesium ion concentration of 0.04 M and 0.1 M respectively. It can be seen from this figure that there is little to no formation of magnesium hydroxide nanostructures on the zeolite surface although both systems were saturated with magnesium ions. This observation is consistent with the hypothesis that the predominant adsorption mechanism in the magnesium ion – ion exchanged zeolite is surface adsorption of Mg^{2+} ions, whereas the predominant adsorption mechanisms in the magnesium ion – zeolite system are ion exchange and surface adsorption of Mg^{2+} ions. This also suggests that ammonium hydroxide plays a crucial role in inducing the nucleation and growth of magnesium hydroxide crystals on the zeolite as noted in the magnesium hydroxide – zeolite system.

In comparison with the magnesium ion – zeolite and magnesium ion – ion exchanged zeolite systems, the magnesium hydroxide – zeolite system displays the highest adsorption capacity and a step-wise adsorption behavior. In the magnesium hydroxide – zeolite system, three distinctive processes such as surface adsorption of Mg^{2+} ions, ion exchange between Mg^{2+} and Na^{+} ions, as well as surface precipitation of $Mg(OH)_2$ may happen simultaneously. At low initial Mg^{2+} ions concentration, roughly the same amount of Mg^{2+} ions was adsorbed by the magnesium ion – zeolite and magnesium hydroxide – zeolite systems. Furthermore, the pH value of both systems was the highest when the concentration of Mg^{2+} ion was the lowest (as shown in Fig. 5.6).

This shows that at low Mg^{2+} ion concentration, ion exchange and hydrolysis of zeolite predominate and there is little to no precipitation of $Mg(OH)_2$. As the initial Mg^{2+} ion concentration increased, the adsorption density of magnesium ion – zeolite system and magnesium hydroxide – zeolite system increased by different amounts. At the same time, a decrease in the pH can be observed in both systems. The pH decreased as the initial Mg^{2+} ion concentration increased (see Fig. 5.6).

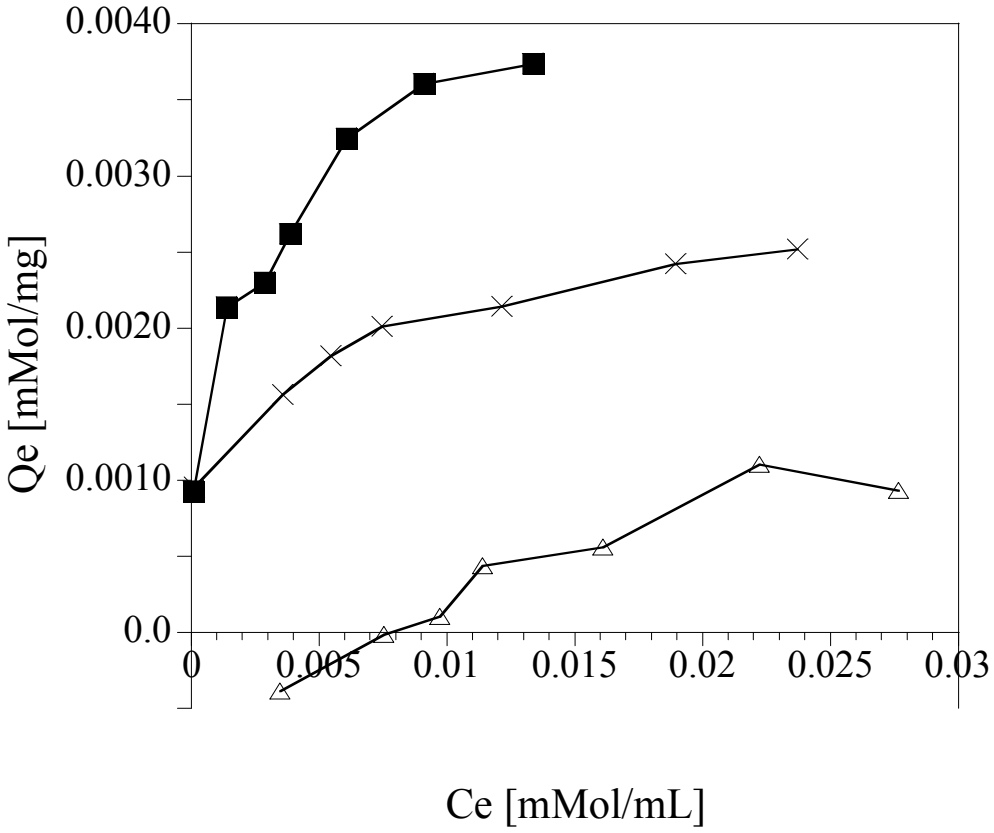

Fig. 5.5 Adsorption isotherms for magnesium hydroxide – zeolite system (■), magnesium ion –zeolite system (x), and magnesium ion – ion exchanged zeolite system (Δ) obtained at 72 h.

Figure 5.6 shows the change in the pH of the magnesium hydroxide – zeolite, magnesium ion – zeolite, and magnesium ion – ion exchanged zeolite systems with respect to the change in initial magnesium ion concentration. In this figure, it can be

observed that the overall pH was highest in the magnesium hydroxide – zeolite system, followed by magnesium ion – zeolite system and magnesium ion – ion exchanged zeolite system. In all of these systems, the pH was highest when the concentration of Mg^{2+} ion was lowest and it decreased with increasing initial Mg^{2+} ion concentration. This is because when magnesium ions dissolved in the solution, the magnesium ions were hydrolyzed according to:

$$Mg^{2+} + H_2O \leftrightarrow [MgOH]^+ + H^+$$

At low concentration of Mg^{2+} ions, only a small amount of hydronium ions were generated. However, the amount of hydronium ions increased as the concentration of Mg^{2+} ions increased, thus reducing the pH. At the same time, the zeolite might be hydrolyzed by the hydronium ions especially in dilute cation solution [25, 27-29]. High cation concentrations have been shown to decrease the selectivity of the zeolite for hydronium ions [28, 29]. Therefore, the pH of these systems was the highest at low concentration of Mg^{2+} ions and decreased as the concentration of Mg^{2+} ions increased.

It can also be seen that although the magnesium ion – zeolite and magnesium ion – ion exchanged zeolite systems were treated under similar experimental conditions, the pH of the magnesium ion – zeolite system is higher than the pH of the magnesium ion – ion exchanged zeolite system. This is because in the magnesium ion – ion exchanged zeolite system, the Na^+ ions in the zeolite were partially, if not completely, exchanged with Mg^{2+} ions. It has been reported that the basic strength of the zeolite increases with the electropositivity of the exchangeable cations [30, 31]. Since sodium is more electropositive than magnesium [32], the zeolite in the magnesium ion – zeolite system is more basic, and the system stabilized at higher pH values. The higher the number of

sodium ions present in the zeolite, the more alkaline is the zeolite solution [33]. Moreover, according to Lutz et al. [34], A-type zeolites can be considered as salts of a heteropoly acid composed of an acidic component (the proton form of the anionic framework) and a base (metal hydroxide). In this way, the general zeolites such as NaA consist of a weak acid and a strong base. When the Na^{+} ion is replaced with Mg^{2+} ion, for example, MgA, the zeolite consists of a weak acid and a very weak base. The stronger the base (the more soluble the cation hydroxide), the higher the pH value of the zeolite solution. Therefore, the pH value of the magnesium ion –zeolite system is higher than the magnesium ion – ion exchanged zeolite system.

Moreover, it can be observed that the pH value of the magnesium ion – zeolite system was close to neutral at high Mg^{2+} ion concentrations. This could be due to hydrolysis of the dissolved Mg^{2+} ions which generated hydronium ions that decreased the pH. In addition, it can be seen from Fig.5.6 that the pH drop in the magnesium hydroxide – zeolite system is less drastic than the magnesium ion – zeolite system at high initial Mg^{2+} ion concentration. This is because in the magnesium hydroxide – zeolite system, equimolar ammonium hydroxide was added in a 3: 1 ratio with respect to the volume of magnesium chloride solution in the system. When ammonium hydroxide is added to a solution of magnesium chloride, part of the magnesium is precipitated as magnesium hydroxide in accordance with the equation [35, 36]

$$MgCl_2 + 2NH_4OH \rightarrow Mg(OH)_2 + 2NH_4Cl$$

but the precipitation is never complete, for the reverse action occurs simultaneously.

$$Mg(OH)_2 + 2NH_4Cl \rightarrow MgCl_2 + 2NH_4OH$$

Therefore, at high concentration of magnesium chloride, sufficient ammonium chloride was generated which reversed the precipitation of $Mg(OH)_2$ and generated ammonium hydroxide that prevented the drastic drop of pH as seen in the magnesium ion – zeolite system.

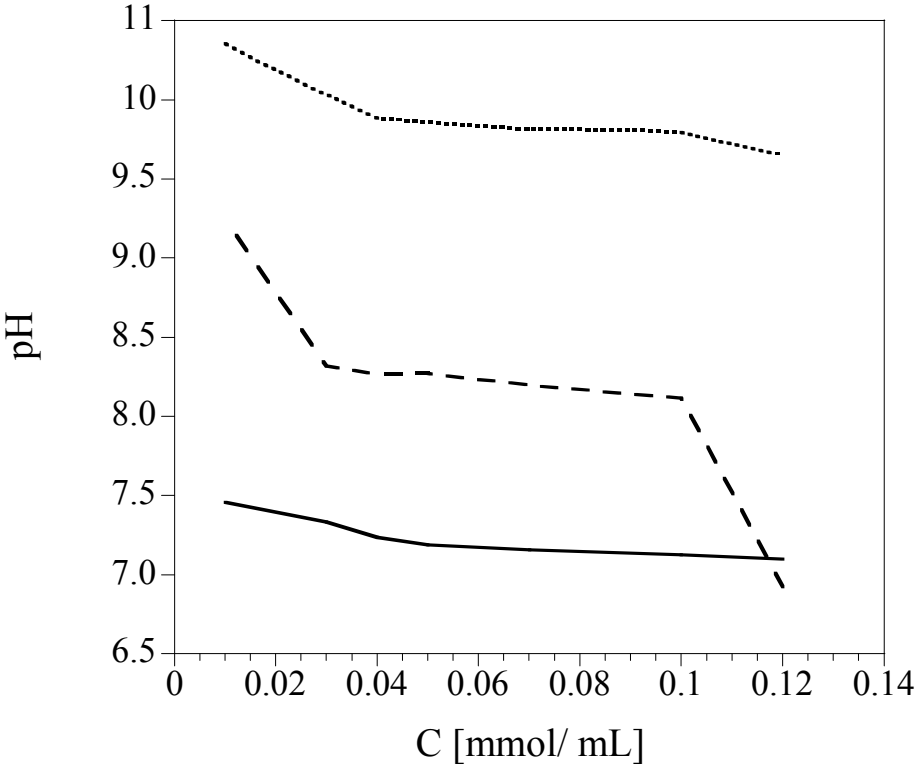

Fig. 5.6 pH versus initial magnesium ion concentration at 72 h; magnesium hydroxide – zeolite system (dotted line), magnesium ion – zeolite system (dashed line), and magnesium ion – ion exchanged zeolite system (solid line).

These adsorption and pH studies of the magnesium hydroxide – zeolite, magnesium ion – zeolite, and magnesium ion – ion exchanged zeolite systems show that three adsorption mechanisms (ion exchange, surface adsorption of Mg^{2+}, and surface precipitation of $Mg(OH)_2$) are involved in the adsorption of $Mg(OH)_2$. It is also clear that ammonium hydroxide induces the nucleation and precipitation of $Mg(OH)_2$ on the zeolite. Without ammonium hydroxide, the predominant species in the system is Mg^{2+}

ions [37] and therefore surface adsorption of Mg^{2+} ions predominates (as seen in the magnesium ion – ion exchanged zeolite system. In the magnesium ion – zeolite system, the predominant processes are adsorption of Mg^{2+} ions and ion exchange between Mg^{2+} and Na^{+} ions in the zeolite. Little to no surface precipitation of $Mg(OH)_2$ took place in these two systems. This is also collaborated by the pH analyses and SEM images shown in Fig. 5.6 and 5.7. The pH of these two systems was not favorable for the precipitation of $Mg(OH)_2$ and no precipitation of $Mg(OH)_2$ nanostructures can be seen on the surfaces of these zeolites.

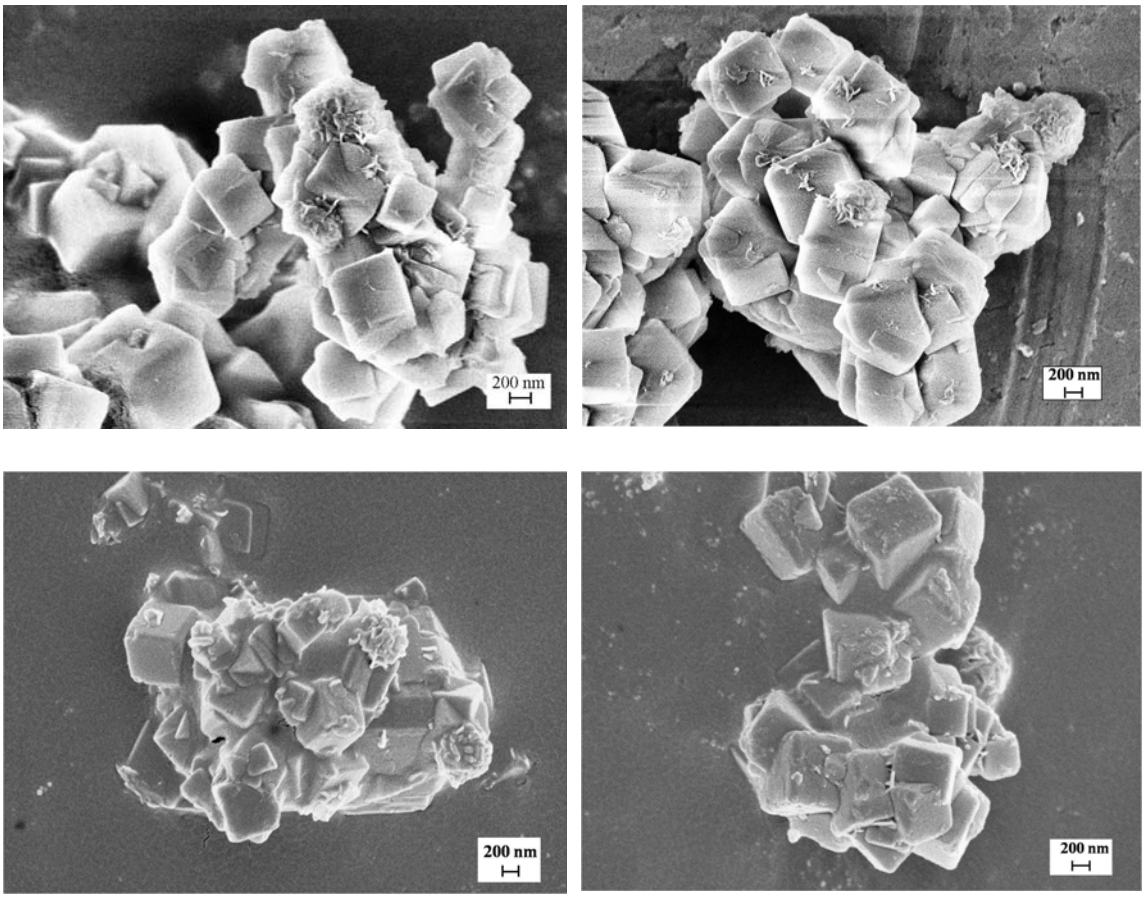

Fig. 5.7 Representative SEM images of zeolites obtained at 72 h from magnesium ion – zeolite system at initial magnesium ion concentration: a) 0.04 M, b) 0.1 M; Magnesium ion – ion exchanged zeolite systems at initial magnesium ion concentration: c) 0.04 M, d) 0.1 M.

5-5 Conclusions

Isotherms were measured for the adsorption of $Mg(OH)_2$ on zeolite 4A (magnesium hydroxide – zeolite system). It was demonstrated that three adsorption mechanisms namely ion exchange, surface adsorption of Mg^{2+} ions, and surface precipitation of $Mg(OH)_2$ are involved in the deposition of $Mg(OH)_2$. Analysis of the magnesium hydroxide – zeolite system adsorption isotherms showed that the isotherms resemble an H-type isotherm, suggestive of specific interactions between $Mg(OH)_2$ and zeolite. The adsorption isotherms also indicated four distinct regions of adsorption. In region I, ion exchange and surface adsorption of Mg^{2+} ions were observed. Simultaneous Mg^{2+} ion adsorption and surface precipitation occurred in region II which marks the completion of "monolayer" formation. Surface precipitation was predominant in region III and the growth rate of the precipitated magnesium hydroxide became independent of the Mg^{2+} ion concentration in region IV. Adsorption isotherms were also measured using virgin zeolite 4A and ion-exchanged zeolite 4A in magnesium chloride solution and it was determined that the predominant processes in the absence of ammonium hydroxide are ion exchange and surface adsorption of Mg^{2+} ions. Therefore, ammonium hydroxide plays a significant role in controlling the pH of the slurries and in inducing nucleation and precipitation of $Mg(OH)_2$ on zeolite surfaces.

5-6 References

1. Giles, C.H., D. Smith, and A. Huitson, *A general treatment and classification of the solute adsorption isotherm. I. Theoretical.* Journal of Colloid and Interface Science, 1974. 47(3): p. 755-765.

2. Giles, C.H., A.P. D'Silva, and I.A. Easton, *A general treatment and classification of the solute adsorption isotherm part. II. Experimental interpretation.* Journal of Colloid and Interface Science, 1974. 47(3): p. 766-778.

3. Giles, C.H., T.H. Macewan, S.N. Nakhwa, and D. Smith, *Studies in adsorption. Part XI. A system of classification of solution adsorption isotherms, and its use in diagnosis of adsorption mechanisms and in measurement of specific surface areas of solids.* Journal of the Chemical Society, 1960(OCT): p. 3973-3993.

4. Sparks, D.L., *Environmental soil chemistry*. 2nd ed. ed. 2003, Amsterdam ;: Academic Press.

5. Selim, H.M.E. and I.K. Iskandar, eds. *Fate and transport of heavy metals in the vadose zone*. 1999, Lewis Publishers: Boca Raton, Fla. 328 p.

6. Tamamushi, B. and K. Tamaki, *Adsorption of long-chain electrolytes at the solid/liquid interface. Part 2.-The adsorption on polar and non-polar adsorbents.* Transactions of the Faraday Society, 1959. 55: p. 1007-1012.

7. Tamamushi, B. and K. Tamaki, *Adsorption of long-chain electrolytes at the solid/liquid interface. Part 3.-The adsorption on ion-exchange resins.* Transactions of the Faraday Society, 1959. 55: p. 1013-1016.

8. Giles, C.H., I.A. Easton, and R.B. McKay, *Mechanism of adsorption of cationic dyes by alumina and a note on heat changes in solution adsorption.* Journal of the Chemical Society, 1964(NOV): p. 4495-4503.

9. Matocha, C.J., E.J. Elzinga, and D.L. Sparks, *Reactivity of Pb(II) at the Mn(III,IV) (oxyhydr)oxide-water interface.* Environmental Science & Technology, 2001. 35(14): p. 2967-2972.

10. Breck, D.W., *Zeolite molecular sieves: Structure, chemistry, and use.* . 1973, New York: John Wiley & Sons.

11. Komarek, M., A. Vanek, V. Chrastn, J. Szakova, K. Kubov, P. Drahota, and J. Balik, *Retention of copper originating from different fungicides in contrasting soil types.* Journal of Hazardous Materials, 2009. 166(2-3): p. 1395-1402.

12. Ponizovsky, A.A., H.E. Allen, and A.J. Ackerman, *Copper activity in soil solutions of calcareous soils.* Environmental Pollution, 2007. 145(1): p. 1-6.

13. Turan, M., U. Mart, B. Yuksel, and M.S. Celik, *Lead removal in fixed-bed columns by zeolite and sepiolite*. 2005. p. 1487-1492.

14. Peric, J., M. Trgo, and N. Vukojevic Medvidovic, *Removal of zinc, copper and lead by natural zeolite-A comparison of adsorption isotherms.* Water Research, 2004. 38(7): p. 1893-1899.

15. Wu, D., Y. Sui, S. He, X. Wang, C. Li, and H. Kong, *Removal of trivalent chromium from aqueous solution by zeolite synthesized from coal fly ash.* Journal of Hazardous Materials, 2008. 155(3): p. 415-423.

16. Hui, K.S., C.Y.H. Chao, and S.C. Kot, *Removal of mixed heavy metal ions in wastewater by zeolite 4A and residual products from recycled coal fly ash.* Journal of Hazardous Materials, 2005. 127(1-3): p. 89-101.

17. Leentvaar, J. and M. Rebhun, *Effect of magnesium and calcium precipitation on coagulation-flocculation with lime.* Water Research, 1982. 16(5): p. 655-662.

18. Choudhary, V.R., S.G. Pataskar, M.Y. Pandit, and V.G. Gunjikar, *Influence of precipitation conditions of magnesium hydroxide on its thermal decomposition in the preparation of active MgO.* Thermochimica Acta, 1992. 194: p. 361-373.

19. Phillips, V.A., J.L. Kolbe, and H. Opperhauser, *Effect of pH on the growth of $Mg(OH)_2$ crystals in an aqueous environment at 60 ^oC.* Journal of Crystal Growth, 1977. 41(2): p. 228-234.

20. Sanchez, R.M.T., E.I. Basaldella, and J.C. Tara, *Zeolites surface reactions pointed out by charge parameters.* Materials Letters, 2001. 50(2-3): p. 138-144.

21. Regalbuto, J., ed. *Catalyst preparation : Science and engineering*. 2007, CRC Press/Taylor & Francis: Boca Raton.

22. Bokhimi, X., A. Morales, M. Portilla, and A. Garcia-Ruiz, *Hydroxides as precursors of nanocrystalline oxides.* Nanostructured Materials, 1999. 12(1-4): p. 589-592.

23. Ohtsuka, K., M. Suda, M. Tsunoda, and M. Ono, *Synthesis of metal hydroxide-layer silicate intercalation compounds (metal = Mg(II), Ca(II), Mn(II), Fe(II), Co(II), Ni(II), Zn(II), and Cd(II)).* Chemistry of Materials, 1990. 2(5): p. 511-517.

24. Doula, M.K., *Removal of Mn^{2+} ions from drinking water by using Clinoptilolite and a Clinoptilolite-Fe oxide system.* Water Research, 2006. 40(17): p. 3167-3176.

25. Harjula, R., A. Dyer, and R.P. Townsend, *Ion-exchange in zeolites .3. Hydrolysis and trace $^{45}Ca^{2+}$ and $^{22}Na^{+}$ exchanges in zeolite-X and zeolite-Y.* Journal of the Chemical Society-Faraday Transactions, 1993. 89(6): p. 977-981.

26. Harjula, R., A. Dyer, S.D. Pearson, and R.P. Townsend, *Ion-exchange in zeolites .1. Prediction of Ca^{2+}-Na^{+} equilibria in zeolites-X and zeolite-Y.* Journal of the Chemical Society-Faraday Transactions, 1992. 88(11): p. 1591-1597.

27. Harjula, R., J. Lehto, J.H. Pothuis, A. Dyer, and R.P. Townsend, *Ion-exchange in zeolites .2. Hydrolysis and dissolution of zeolites NaX and NaY.* Journal of the Chemical Society-Faraday Transactions, 1993. 89(6): p. 971-976.

28. Brouillette, F., B. Chabot, D. Morneau, and C. Daneault, *Effect of physico-chemical conditions on the properties of zeolite microparticles used in pulp and paper applications.* Microporous and Mesoporous Materials, 2004. 70(1-3): p. 51-56.

29. Cook, T.E., W.A. Cilley, A.C. Savitsky, and B.H. Wiers, *Zeolite A hydrolysis and degradation.* Environmental Science & Technology, 1982. 16(6): p. 344-350.

30. Bonenfant, D., M. Kharoune, P. Niquette, M. Mimeault, and R. Hausler, *Advances in principal factors influencing carbon dioxide adsorption on zeolites.* Science and Technology of Advanced Materials, 2008. 9(1).

31. Doskocil, E.J. and R.J. Davis, *Spectroscopic characterization and catalytic activity of zeolite X containing occluded alkali species.* Journal of Catalysis, 1999. 188(2): p. 353-364.

32. Arora, M.G., *Periodic Table and Periodic Properties*. 1997, Delhi: Anmol Publications Pvt Ltd. 160.

33. Wark, M., W. Lutz, G. Schulz-Ekloff, and A. Dyer, *Quantitative monitoring of side products during high loading of zeolites by heavy metals via pH measurements.* Zeolites, 1993. 13(8): p. 658-662.

34. Lutz, W., M. Bulow, N.N. Feoktistova, L.B. Vtjurina, S.P. Shdanov, and H. Siegel, *Zeolite NaCaA as a desulphurization adsorbent - modification of its thermal and hydrothermal stability.* Crystal Research and Technology, 1989. 24(2): p. 161-165.

35. Caven, R.M., *Systematic inorganic chemistry from the standpoint of the periodic law*. 5th ed., revised ed, ed. G.D. Lander and A.B. Crawford. 1936, London: Blackie.

36. Walker, J., *Introduction to physical chemistry*. 10th ed. ed. 1927, London: Macmillan.

37. Wulfsberg, G., *Inorganic Chemistry*. 2000, Sausalito, Calif.: University Science Books.

CHAPTER 6

MECHANISM OF SITE-SPECIFIC DEPOSITION OF MAGNESIUM HYDROXIDE ON ZEOLITE 4A – SOLID STATE NMR AND FTIR STUDIES

6-1 Introduction

In Chapter 5, it was found that the adsorption of magnesium hydroxide on zeolite 4A yields H-type isotherms. H-type isotherms indicate that there may be very strong adsorbate-adsorbent interactions, caused either by specific interactions between the solid phase and the adsorbate or by significant van der Waals interactions in the adsorption process [1]. Therefore, it is necessary to determine the nature of these specific interactions between magnesium hydroxide and zeolite 4A.

In this chapter, the mechanism of deposition and growth of $Mg(OH)_2$ nanostructures on the zeolite surface are explored. There are three possible sites on the zeolite where magnesium hydroxide can adsorb. These sites are silanol (Si-OH), aluminol (Al-OH), and bridging hydroxyl proton (Si-OH-Al). In principle, the Brönsted acidity of these three hydroxyl protons increases in the order of Al-OH < Si-OH < Si-OH-Al, with bridging hydroxyl proton being the strongest acid [2-4]. Therefore, it is hypothesized that the weakly basic $Mg(OH)_2$ will preferably interact with the most acidic Si-OH-Al via an acid-base interaction. In this study, $Mg(OH)_2$ / zeolite 4A nanocomposites were synthesized based on the procedure stated in chapter 3 The nanocomposites were also prepared using two other different methods where the sequence of magnesium chloride and ammonium hydroxide addition was varied. It is hypothesized that if zeolite is added

into the ammonium hydroxide solution first instead of magnesium chloride solution, the acidic bridging hydroxyl proton will be neutralized by ammonium hydroxide and there will be very little deposition of magnesium hydroxide on the zeolite. Adsorption studies were also carried out on alumina and silica in order to identify specific sites for the deposition of $Mg(OH)_2$. It is noted that Al-OH sites are found on alumina and zeolite 4A surfaces, Si-OH sites on silica and zeolite 4A surfaces, and bridging hydroxyl proton (Si-OH-Al) sites only on zeolite 4A surfaces. The $Mg(OH)_2$ / zeolite 4A nanocomposites were characterized and examined by solid state ^{1}H, ^{29}Si, and ^{27}Al NMR and FTIR. Solid state NMR was used for characterizing the structure of modified zeolites as well as interactions between guests and hosts in zeolite complexes. FTIR analysis was used to verify the presence of $Mg(OH)_2$ in the nanocomposite and to examine the vibrational properties of water confined in the zeolite.

6-2 Experimental

6-2-1 *Materials*

The following materials were purchased and used as received: Magnesium chloride ($MgCl_2.6H_2O$, ACS reagent grade) and ammonium hydroxide (NH_4OH, ACS reagent grade) from Fischer Scientific (NJ, USA); silicon oxide particles with an average primary particle size of 3 μm from Nanomaterials & Amorphous Materials Inc. (TX, USA); aluminum oxide particles with an average primary particle size of 3 μm from Electron Microscopy Sciences (PA, USA); and magnesium hydroxide powder ($Mg(OH)_2$, 95 wt %) with a bulk density of 2.36 g/cm^3 from Spectrum Chemicals and Laboratory Products (CA, USA). Deionized water was made in the laboratory.

6-2-2 *Nanocomposite preparation procedures*

The $Mg(OH)_2$ / zeolite 4A nanocomposites were prepared following the procedure outlined in chapter 3 (known as method (i) in this chapter) with 0.04 M of magnesium chloride and ammonium hydroxide solutions. The same procedure was followed with silica and alumina particles except that the concentrations of $MgCl_2.6H_2O$ and NH_4OH were increased to 0.1 M. In addition, $Mg(OH)_2$ / zeolite 4A nanocomposites were also prepared using a second method. In method (ii), 0.1 g of zeolite was added to 30 mL of 0.04 M NH_4OH solution followed by titration with 10 mL of 0.04 M of $MgCl_2.6H_2O$ with stirring. The $Mg(OH)_2$ particles were then allowed to diffuse/ grow at ambient conditions for 48 h without further stirring, after which nanocomposites were collected and treated as described in method (i). In method (iii), 0.1 g of zeolite was added to 10 mL of deionized water, followed by simultaneous titration of 10 mL of 0.05 M of $MgCl_2.6\ H_2O$ and 30 mL of 0.05 M NH_4OH solutions and subsequent diffusion/ growth period of 48 h at at ambient conditions without stirring. At the end of 48 h, nanocomposites were collected and treated as described in method (i) (see chapter 3).

6-2-3 *Characterizations*

The concentrations of magnesium and sodium in the zeolite solution were determined via ICP-OES (Inductively Coupled Plasma - Optical Emission Spectroscopy) using a JY- Horiba Ultima 2C instrument (HORIBA Jobin Yvon, USA). A 2 mL sample was collected from the zeolite solution at the end of the 72 h growth period and diluted with 3 mL of 2 % nitric acid before performing the analysis.

SEM images of the nanocomposites were obtained with a LEO 1530 TFE (thermally-assisted field-emission) scanning electron microscope (Carl Zeiss SMT Inc., Germany) equipped with an EDS (energy dispersive X-ray spectroscopy) and thermally assisted field emission gun operating at 5 KeV. The samples were sputter-coated with a thin layer of gold film before SEM analysis. Powder XRD (X-ray diffraction) patterns were obtained on a Philips X'pert diffractometer (PANalytical Inc, USA) equipped with X'celerator using Cu Kα radiation.

Solid-state MAS NMR spectra were measured with a Bruker DSX 300 spectrometer (Bruker Corporation, USA) at resonance frequency of 54.6 MHz for ^{29}Si nuclei at spinning rate 5 kHz. The measurements for ^{29}Si spectra were performed using a 90 degree pulse length of 5 μs, and recycle delay of 10 s respectively. ^{1}H and ^{27}Al MAS NMR spectra were recorded on a Bruker Avance III spectrometer (Bruker Corporation, USA) at resonance frequencies of 400.1 MHz and 104.2 MHz and at spinning rates of 12 kHz and 10 kHz. The measurements for ^{1}H spectra were performed using a 90 degree pulse length of 5 μs and recycle delay of 4 s. The measurements for ^{27}Al were conducted using a $\pi/12$ pulse length of 0.6 μs and a recycle delay of 0.2 s. ^{1}H, ^{29}Si, and ^{27}Al chemical shifts were referred to adamantane at 1.9 ppm, 2 (Trimethylsilyl) -1-propanesulfonic acid at 0 ppm, and saturated aqueous solution of $AlCl_3$ at 0 ppm, respectively.

FTIR spectra were collected under vacuum conditions on a Bruker IFS 66 v/S spectrometer (Bruker Corporation, USA). The sample was finely ground and diluted to 3 wt % with KBr powder before being pressed into a translucent pellet with a hand press.

All IR measurements were carried out with a repetition of 50 scans under a resolution of 4 cm^{-1} in the absorbance mode at room temperature.

The $Mg(OH)_2$ powder, virgin zeolite 4A, and treated zeolite 4A were dried in a vacuum oven at 50 ºC for 24 h before analysis. The thermal behavior of the samples was analyzed on a Seiko TG/DTA 320 thermogravimetric analyzer (Seiko Instruments, USA). A N_2 gas sweep at a flow rate of 100 ml /min was used during the TGA measurements. Two separate heating procedures were employed: (1) during dynamic TG runs, the temperature was raised from room temperature to 550 ºC at a heating rate of 10 ºC /minute; (2) based on TG dynamic runs, the temperature was first increased from room temperature to 170 ºC at a rate of 2 ºC /min, kept at 170 °C for 90 min, then increased from 170 ºC to 410 ºC at a rate of 10 ºC /min, and kept at 410 °C for another 30 min before cooling down.

6-3 Results

6-3-1 *Characterization and identification of surface nanostructures*

Figure 6.1 shows the surface morphologies of zeolite 4A, aluminum oxide and silicon oxide before and/or after treatment. Figure 6.1a confirms that a nanopetal structure was created on the outer surfaces of zeolite 4A. Figure 6.1b shows a SEM image of commercial $Mg(OH)_2$ powder that is discussed later. Figure 6.1c and d show SEM images of treated zeolite 4A at different magnification scales. It can be clearly seen that uniform $Mg(OH)_2$ nanopetals are formed on the zeolite 4A surface.

The treated zeolite 4A, aluminum oxide and silicon oxide samples are compared in order to identify specific sites for the deposition of $Mg(OH)_2$. It is noted that Al-OH

sites are found on alumina and zeolite 4A surfaces, Si-OH sites on silica and zeolite 4A surfaces, and bridging hydroxyl proton (Si-OH-Al) sites only on zeolite 4A surfaces. Figure 6.1e and f show SEM images of aluminum oxide and silicon oxide after undergoing the same treatment as zeolite 4A. These figures clearly show the smooth surfaces of aluminum oxide and silicon oxide, indicating that there is no formation of $Mg(OH)_2$ on the surfaces of these samples. This was also confirmed by EDS spectra which showed no magnesium on the surfaces of these two oxides (Fig. 6.2b and c). In contrast, Fig. 6.2a shows peaks from Na, Al, and Si from the zeolite and Mg from $Mg(OH)_2$ on the surface of treated zeolite 4A. The Au peak appears in the image because the zeolite sample was coated with gold film to improve resolution of SEM images. Figure 6.3 shows XRD patterns of virgin zeolite 4A, commercial $Mg(OH)_2$ powder, and treated zeolite 4A. As can be seen from Fig. 6.3c, the zeolite 4A structure and crystallinity remained intact after treatment. Peaks from crystalline $Mg(OH)_2$ in the treated zeolite 4A prepared via method (i) are relatively weak due to the high crystallinity of the zeolite (Fig. 6.3c).

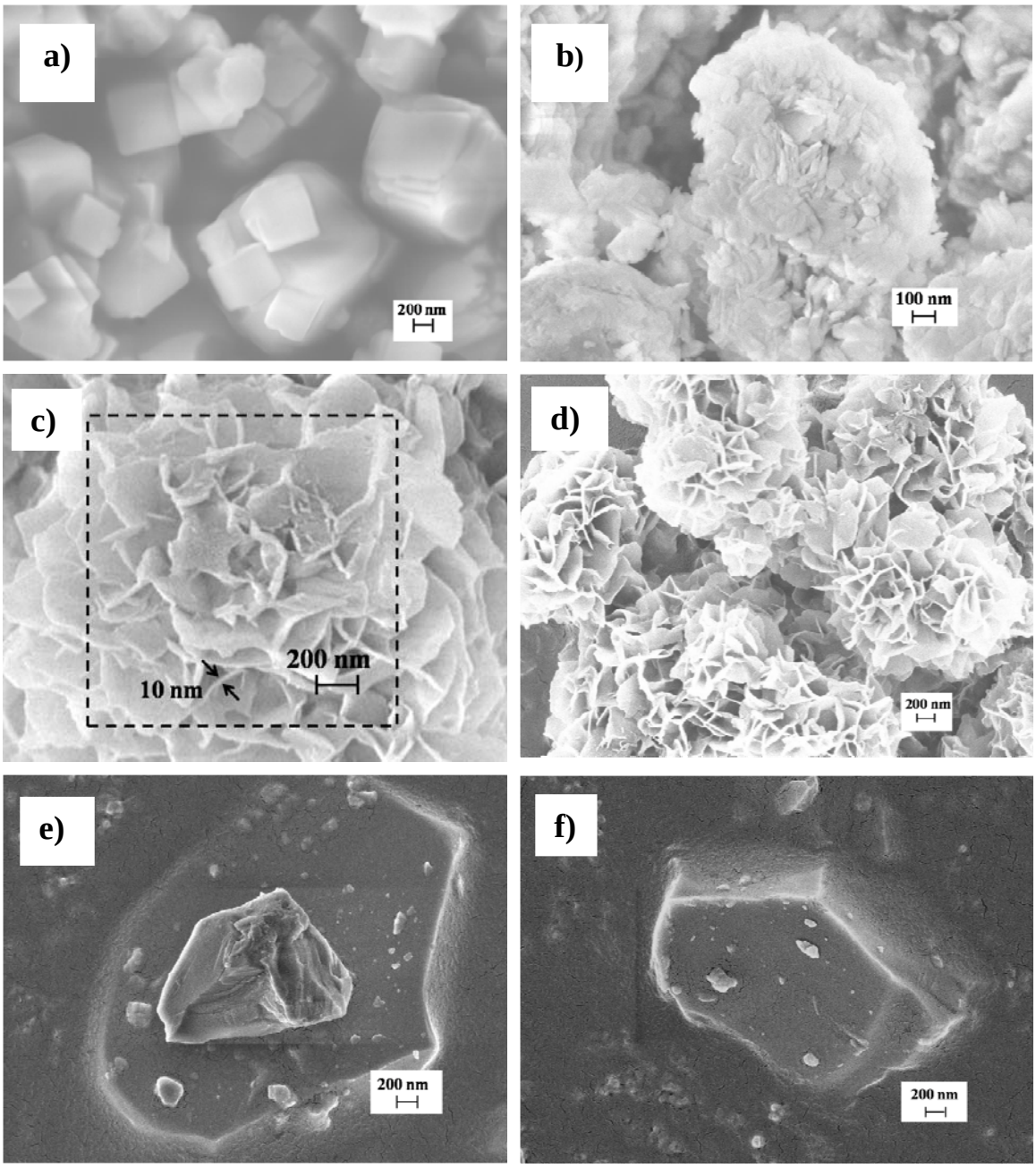

Fig. 6.1 Representative SEM images of (a) untreated zeolite 4A, (b) $Mg(OH)_2$ powder, (c, d) treated zeolite 4A, (e) treated aluminum oxide, and (f) treated silicon oxide.

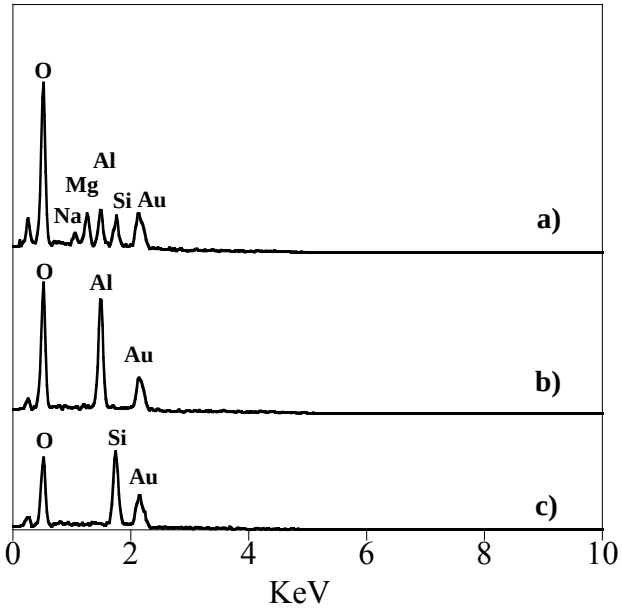

Fig. 6.2 EDS analysis of treated (a) zeolite 4A, (b) aluminum oxide, and (c) silicon oxide.

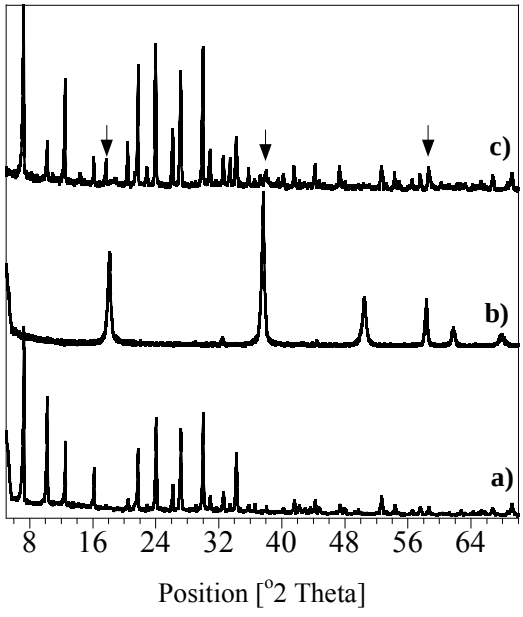

Fig. 6.3 XRD patterns of (a) virgin zeolite 4A, (b) commercial $Mg(OH)_2$ powder, (c) zeolite treated with 0.04 M $MgCl_2$ / NH_4OH.

6-3-2 *Effect of synthesis procedure on deposition of $Mg(OH)_2$ nanostructures*

The effect of the synthesis procedure was investigated by comparing samples prepared using the three procedures described in section 6-2-2 with a growth time of 48 h. Figure 6.4a and 6.4c show that $Mg(OH)_2$ nanopetals were deposited on the surface of the zeolite within 48 h in samples prepared using methods (i) and (iii). Method (i) favors homogeneous growth and more uniform distribution of $Mg(OH)_2$ nanopetals than method (iii), as indicated in the insets of Fig. 6.4a and c. On the other hand, when method (ii) was used to prepare the samples, small irregular $Mg(OH)_2$ platelets were obtained and these platelets were nonuniformly distributed on the zeolite surface (Fig. 6.4b). This suggests that there are less active sites for the deposition of $Mg(OH)_2$ because the acidic bridging hydroxyl protons were neutralized by ammonium hydroxide. The platelets transformed to a peony-like shape within 48 h (Fig. 6.4a). With a further increase in growth time (from 48 h to 72 h), the peony grew larger and became spherical, as shown in Fig. 6.1c and d. It is therefore concluded that the shape, size and distribution of $Mg(OH)_2$ nanopetals can be controlled via the experimental procedure.

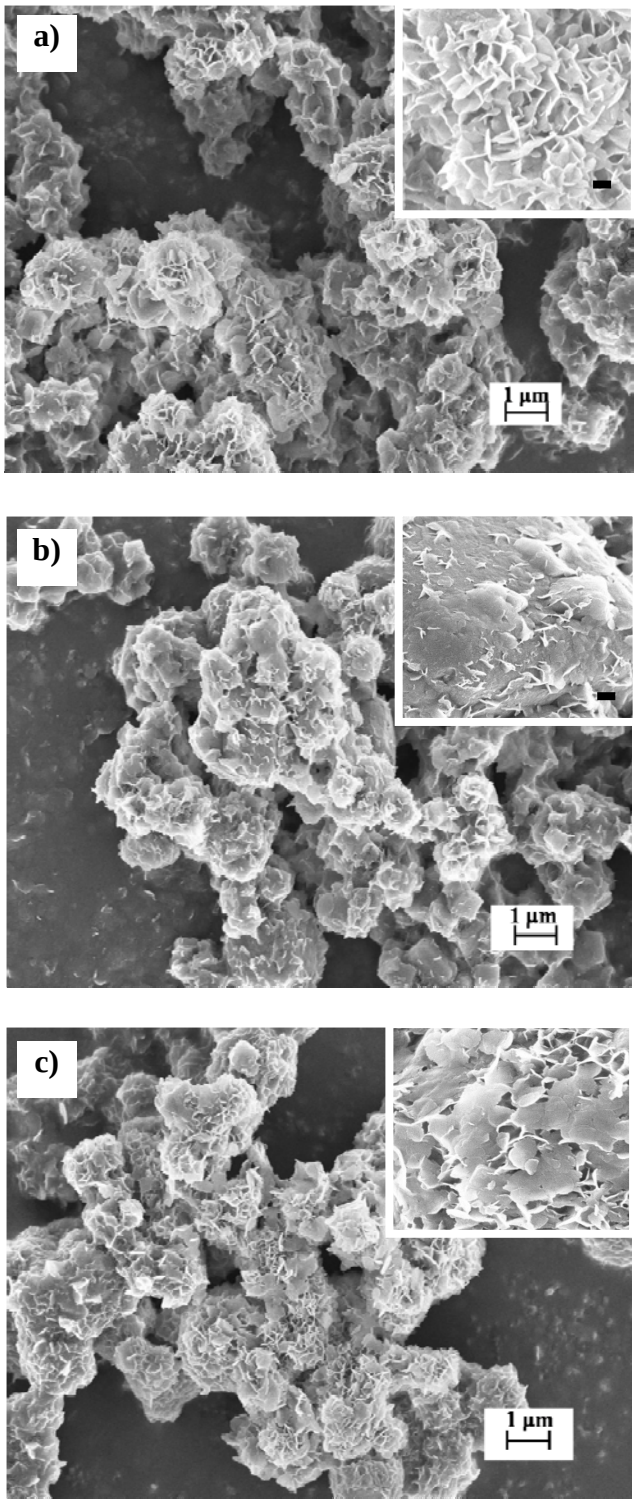

Fig. 6.4 SEM images of treated zeolite 4A obtained using (a) method (i) (b) method (ii), and (c) method (iii). The insets are magnified images with a scale bar of 200 nm.

6-3-3 *Structure of zeolite after surface modification*

Changes in the zeolite structure due to surface modification by $Mg(OH)_2$ were investigated using a combination of solid-state ^{1}H, ^{27}Al and ^{29}Si NMR, ICP-OES, TGA, and FTIR measurements. Solid state NMR has been extensively used for characterizing the structure of modified zeolites as well as interactions between guests and hosts in zeolite complexes [5-8]. The ^{1}H spectra of untreated zeolite are shown in Fig. 6.5a and reveal a strong peak at 4.8 ppm from physisorbed water in the bulk-like state. In contrast, treated zeolite exhibits a broad ^{1}H spectrum consisting of a strong peak at 7.3 ppm, a broad peak centered at ~5.5 ppm, and two weak peaks at 1.3 ppm and 0.8 ppm. The broad peak at ~5.5 ppm could be due to[27] i) dipolar coupling of water molecules which is too strong to be averaged out by magic angle spinning (MAS); (ii) outer bulk and surface water; (iii) chemical exchange between protons; or to (iv) distribution of chemical shifts arising from the different status of water molecules. These factors are not mutually exclusive in the treated zeolite 4A. Grey *et al.* [9] recently reported that layered double hydroxide confines interlayer water and hydroxides, as well as neighboring OH groups, to the layer surface, leading to very strong ^{1}H homonuclear and ^{1}H–Al heteronuclear dipolar coupling [10]. FTIR spectra of the treated nanocomposite (Fig. 6.6) show that the amount of tetrahedrally arranged water molecules increased after treatment from 32.9 % (I+II) (Fig. 6a) to 53.5 % (Fig. 6.6b). Also, the treated zeolite contained more outer bulk water molecules than virgin zeolite 4A as indicated by TGA runs (Fig. 6.7). The $Mg(OH)_2$ nanopetals on the surface could also increase the distribution of chemical shifts by creating additional defect sites containing water. A chemical shift distribution covering the scale from 6 ppm to 2 ppm [10] would then lead to a peak at ~ 5.5 ppm in

the ^{1}H spectrum. All these factors could have contributed to a significant broadening of the water peak. The high-filed ^{1}H line at 0.8 ppm and 1.3 ppm could originate from the existence of $MgOH^{+}$ [11, 12]. As water is removed during the dehydration process in a vacuum oven, the magnesium cation cannot satisfy the framework charge distribution and the cation associated electrostatic field causes dissociation of the coordinated water molecules, giving rise to the formation of $MgOH^{+}$ [13]. The deposition of $Mg(OH)_2$ nanopetals generates a much stronger peak at 7.3 ppm assigned to the disturbed bridging OH groups [11, 14].

Figure 6.5b illustrates the corresponding ^{29}Si MAS NMR spectra for virgin and treated zeolite 4A. The narrow peak at -90.5 ppm ($\Delta\upsilon_{1/2}$ = 1.5 ppm) in the untreated sample is due to the inherently uniform Si (4Al) framework of zeolite 4A [15, 16]. Such narrow peaks ($\Delta\upsilon_{1/2} \approx$ 0.2 - 3 ppm) are obtained for perfectly ordered structures of zeolite [17]. The peak becomes broad ($\Delta\upsilon_{1/2}$ = 3.1 ppm) after treatment as shown in Fig. 6.5b, which implies that the treated zeolite had a well-ordered Si structure (Si(4Al)). Shu *et al.* [17] reported that a new peak at -96 ppm was generated when zeolite 4A was pretreated with thionyl chloride to create $Mg(OH)_2$ on the surface. This peak was obtained because part of the uniform Si(4Al) framework of their zeolite 4A was converted to Si(3Al) by a dealumination reaction. Since our method is non-destructive, it does not produce a peak at -96 ppm. On the other hand, the line broadening after treatment in Fig. 6.5b could be due to broader distribution of dipolar interactions between ^{29}Si and ^{1}H nuclei, leading to distribution of ^{29}Si chemical shifts and lower decoupling efficiency. This observation reflects the more diverse local environment between ^{29}Si and ^{1}H after treatment, which is in agreement with the ^{1}H spectra discussed above.

Figure 6.5c shows ^{27}Al NMR spectra of zeolite 4A before and after the growth of $Mg(OH)_2$. The single signal at 58.8 ppm in Fig. 6.5c corresponds to tetrahedrally coordinated aluminum (Al^{IV} or AlO_4) in the virgin zeolite framework [16, 17]. The treated 4A exhibits two peaks at 57.2 ppm and 10.7 ppm attributed to Al in octahedral coordination (Al^{VI} or AlO_6) [18]. Treatment induces conversion of AlO_4 to AlO_6. As indicated in Fig. 6.5c, part of AlO_4 (~ 13 % of the total spectral intensity) has been converted to AlO_6. The change in the aluminum coordination has been previously observed in zeolites. In general, octahedral Al sites are created from tetrahedral Al in the zeolite framework by a rigorous dealumination reaction [6, 15, 19, 20]. In this work, octahedral aluminum was created in zeolite 4A under mild process conditions. The ^{29}Si spectrum (Fig. 6.5b) was unchanged after treatment, indicative of no change in the framework structure. It has been reported that framework Al-OH sites can host water molecules giving rise to octahedrally coordinated Al species [21]. A small high field chemical shift of AlO_4 sites after treatment is observed in Fig. 6.5c. This could be due to an increase in the Si-O-Al angle when Na^+ ions were exchanged for Mg^{2+}. Van Bokhoven *et al* .[6] reported that the lanthanum cation La^{3+}, when exchanged with Na^+ in NaY zeolite, polarizes the framework Al, distorts the zeolitic framework and generates a high-field shift of AlO_4. It is worth noting that the treated 4A in Fig. 6.5c demonstrates a slight broadening of the AlO_4 line, the asymmetrical AlO_6 line and strong spinning sidebands (marked by asterisks) relative to untreated 4A. These changes indicate that the 4A under mild treatment has formed distorted AlO_4 sites and local Al positions with diverse isotropic chemical shifts and larger quadrupolar couplings.

The concentrations of Na^+ and Mg^{2+} ions in the mixture containing the zeolites were measured after 72 h of treatment with ICP-OES. Approximately 22 mg of Na^+ (=W_{Na^+}) and 4.89 mg of Mg^{2+} (=W_1) ions were detected in 80 mL of the heterogeneous liquid mixture, indicating that an ion-exchange process took place during the growth of $Mg(OH)_2$. The mass percent of $Mg(OH)_2$ on the surface of the zeolite was estimated from the concentration of Mg^{2+} ions as follows:

$$w_{Mg(OH)_2} = \frac{W_{Mg(OH)_2}}{W_{4A} + W_{Mg(OH)_2}} \times 100\% \qquad \textbf{(1)}$$

where

$$W_{Mg(OH)_2} = (W_0 - W_1 - W_2) \times M_{Mg(OH)_2} / M_{Mg}$$

$$W_2 = \frac{W_{Na^+} \times M_{Mg}}{M_{Na^+} \times 2}$$

Here $w_{Mg(OH)2}$ is the mass percent of magnesium hydroxide on the zeolite surface, W_0 (= 19.2 mg) and W_1 (= 4.89 mg) are the initial and final mass of Mg^{2+} ions in the liquid mixture containing the zeolites, W_2 is the mass of Mg^{2+} ions exchanged for Na^+ ions (assuming that 2 moles of Na^+ ions were substituted by 1 mole of Mg^{2+}) and W_{4A} (= 0.2 g) is the mass of zeolite 4A added to the solution of $MgCl_2$ and NH_4OH. $M_{Mg(OH)2}$ (= 58.32), M_{Mg} (= 24.3), and M_{Na} (= 23) are the molecular weights of magnesium hydroxide, magnesium, and sodium respectively. From the ICP-OES analysis W_{Na^+} = 22.91 mg, which translates to W_2 = 11.95 mg. Since 0.2 g of zeolite 4A was added to the solution, the mass percent of $Mg(OH)_2$ was calculated to be 2.75 %. Without ion exchange (W_2= 0), the theoretical mass percent of $Mg(OH)_2$ was calculated to be 14.66 %.

The thermal behavior of the nanocomposites and their composition were investigated using thermogravimetric analysis. The weight percent of $Mg(OH)_2$ in the nanocomposite was determined from differences in the weight loss due to desorption of water molecules and exclusion of occluded water molecules from both virgin zeolite 4A and treated zeolite 4A, as well as the thermal decomposition of $Mg(OH)_2$. The TGA results of $Mg(OH)_2$ powder, virgin zeolite 4A, and $Mg(OH)_2$ / zeolite 4A composite are shown in Fig. 6.7. Figure 6.7a shows results of TG dynamic runs and corresponding first-order derivatives (DTG) obtained using procedure (1). According to the inset of Fig. 6.6a, two main weight loss events can be seen for the $Mg(OH)_2$ powder. The loss at about 200 ºC is due to desorption of water physisorbed on $Mg(OH)_2$, and the loss at about 300 ºC is due to thermal decomposition of $Mg(OH)_2$ [22]. At a temperature of about 450 ºC, virgin zeolite 4A shows a completion of weight loss, whereas treated zeolite 4A continues to lose weight. The treated zeolite 4A displays a larger weight loss from physisorbed water than virgin zeolite 4A before the decomposition of $Mg(OH)_2$ at about 300 ºC. This could be due to the larger surface area of $Mg(OH)_2$ nanopetals for physisorption of water molecules. Figure 6.7a also shows the weight loss rate of the samples. From the DTG profiles of these samples, a peak centered at about 410 ºC is detected for $Mg(OH)_2$ powder. The weight loss peak detected before 150 ºC for virgin zeolite 4A and treated zeolite 4A samples corresponds to desorption of physically adsorbed water [23-25]. Between 250 ºC and 320 ºC, these two zeolite samples demonstrate a close weight loss rate which is due to the exclusion of occluded water or water aggregates in the cages, cavities, or channels of the zeolite [26]. The peak at 373 ºC for the treated zeolite 4A is ~ 40 ºC lower than for $Mg(OH)_2$ powder. Moreover, this DTG peak is narrower than that of

$Mg(OH)_2$ powder, suggesting uniform growth of $Mg(OH)_2$ nanopetals on the zeolite 4A surface, as shown in Fig. 6.1d. This difference could be attributed to the lower thermal stability of $Mg(OH)_2$ nanopetals than the microscale $Mg(OH)_2$ powder. These findings are similar to those of Pourmortazavi *et al.* [25] for copper carbonate micro and nanoparticles. The decomposition temperature range for copper carbonate nanoparticles is smaller than that for microparticles, and the decomposition temperature of the former is lower than that of the latter [25].

TGA curves of the samples and their weight loss during isothermal runs are shown in Fig. 6.7b. The isothermal temperatures of 170 ºC and 410 ºC correspond to the desorption of physisorbed water and the maximum DTG peak of $Mg(OH)_2$, respectively. The three samples examined experienced no weight loss at 170 ºC. The TGA curve of virgin zeolite 4A shows weight loss intervals at 170 ºC and 410 ºC, corresponding to the exclusion of adsorbed water and occluded water molecules. In the treated zeolite 4A, the first weight loss stage at 170 ºC corresponds to the desorption of physisorbed water from the surface and from $Mg(OH)_2$ nanopetals. The treated zeolite suffered a larger weight loss (~ 3.30 %) than virgin zeolite 4A during the first heating step to 170 ºC. The weight loss of 6.06 % in the treated sample at 410 ºC is most likely due to the exclusion of occluded water molecules and thermal decomposition of $Mg(OH)_2$. Assuming that the treated zeolite 4A has the same amount of occluded water molecules as the virgin zeolite, the weight percent of $Mg(OH)_2$ nanopetals formed on the surface of treated zeolite 4A can be calculated as follows:

$$w_{Mg(OH)2} = \frac{1 - w_{treated,1} - \left(1 + w_{virgin,2} / w_{virgin,end}\right) w_{treated,end}}{1 - \left(1 + w_{virgin,2} / w_{virgin,end}\right) M_{MgO} / M_{Mg(OH)2}} \quad (2)$$

Here $w_{\text{treated, 1}}$ is the weight loss of the treated zeolite during the first heating step and $w_{\text{virgin, 2}}$ is the weight loss of the virgin zeolite during the second heating step. Also $w_{\text{treated, end}}$ and $w_{\text{virgin, end}}$ are the weight percent of the remaining treated and virgin zeolite 4A at the end of the second heating step. M_{MgO} (= 40.32) and $M_{\text{Mg(OH)2}}$ (= 58.32) are the molecular weights of MgO and $Mg(OH)_2$ respectively. As shown in Fig. 7b, $w_{\text{virgin, 2}}$ = 3.22 %, and $w_{\text{virgin, end}}$ = 79.60 %; for the treated zeolite, $w_{\text{treated, 1}}$ = 20.51 % and $w_{\text{treated, end}}$ = 73.28 %. The weight percent of $Mg(OH)_2$ on the surface of zeolite 4A is calculated to be 11.56 % using the above equation. Although the calculation ignores the influence of $Mg(OH)_2$ nanopetals as well as the ion exchange process on the exclusion of occluded water between 170 ^{o}C and 410 ^{o}C, this value is within the weight percent range calculated from ICP-OES analysis (2.75 % - 14.66 %). This confirms that Na^{+} ions in the cavities of zeolite were exchanged for Mg^{2+}.

FTIR analysis was used to verify the presence of $Mg(OH)_2$ in the nanocomposite and to examine the vibrational properties of water confined in the zeolite. Figure 6.6 shows the O-H band fitting results for virgin and treated zeolite 4A. The broad O-H band can be decomposed into four contributions related to bulk and interfacial water molecules [18, 27]. The sub-band ω_1 at ~3000 cm^{-1} is attributed to tetrahedral aggregates involving four water molecules coordinated by the extraframework cation. The sub-band ω_2 centered at about 3200 cm^{-1} describes the tetrahedral arrangement of large clusters of water molecules. The sub-band ω_3 at ~ 3400 cm^{-1} corresponds to water molecules that are

not fully tetrahedrally bonded and it is ascribed to the partial formation of H bridges that generates bifurcated H-bonds (BHB). Finally, the sub-band ω_4 centered at ~ 3600 cm^{-1} is associated with H bonded water molecules that are not arranged in a supramolecular network. The water molecules may exist as dimers exhibiting linear bonds or as interfacial water molecules that are linked to the framework but not connected to any other molecule [18, 27]. From Fig. 6.6, it can be observed that the center frequencies of treated zeolite 4A sub-bands shifted to lower values than in the case of virgin zeolite 4A. Crupi *et al*. [27] reported that when Na-A zeolites are partially ion-exchanged with Mg^{2+} ions, the frequencies of the O-H stretching bands decrease, which agrees with our observations. When virgin zeolite 4A is dispersed in the magnesium chloride solution, the monovalent Na^+ ions in the zeolite are partially substituted with the Mg^{2+} bivalent ions. The smaller Mg^{2+} ions are located on the edges of the α cages of zeolite A, leaving the access channels to the cavities free, which favors a more regular formation of stable water clusters [27]. The validity of the ion exchange process was confirmed by the presence of Na^+ ions in the solution containing the zeolites after 72 h treatment shown by ICP-OES. It should be added that vibration bands [28] corresponding to $Mg(OH)_2$ can also be observed in Fig. 6.6b at 3700 cm^{-1}, and that the bending vibration [29] of the –OH bond in $Mg(OH)_2$ at ~1400 cm^{-1} was also detected but is not shown.

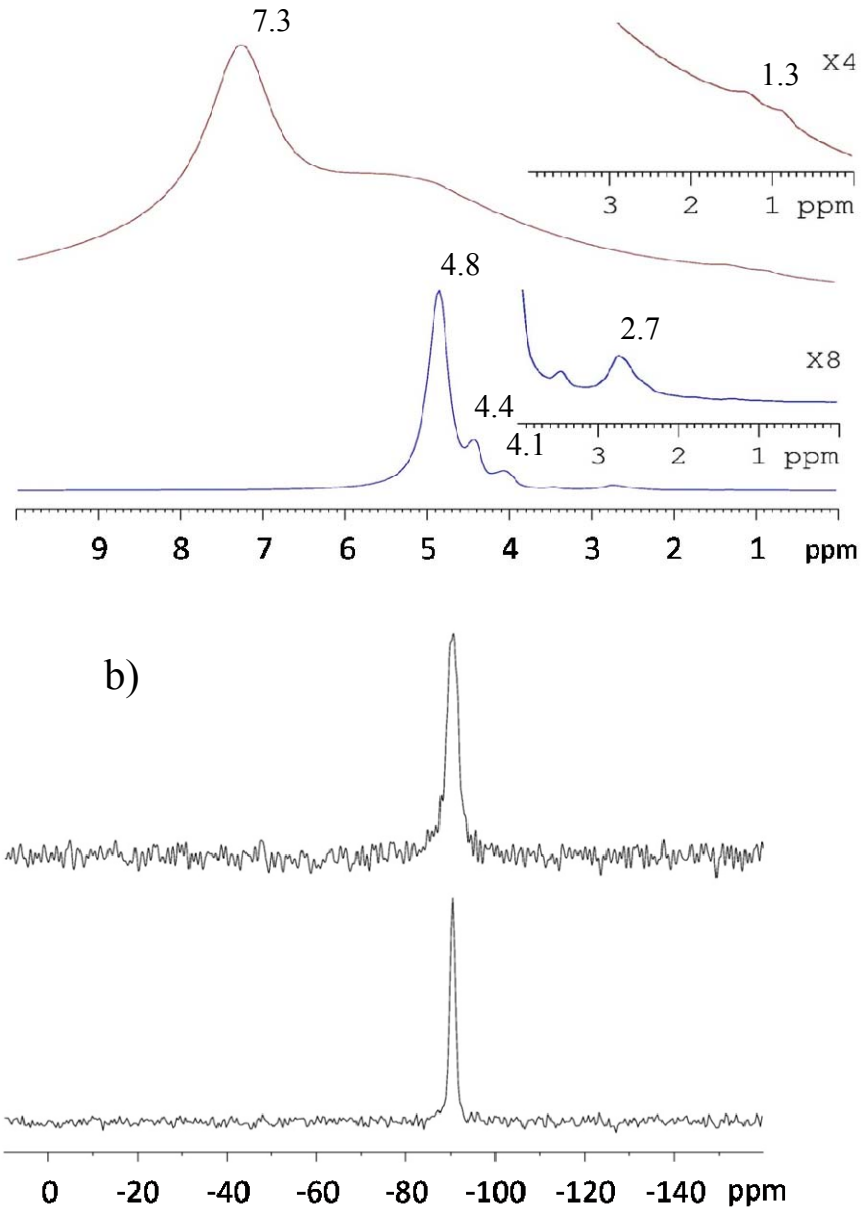
7.3
1.3
X4
3
2
1 ppm
4.8
2.7
X8
4.4
4.1
3
2
1 ppm
9
8
7
6
5
4
3
2
1
ppm
b)
0
-20
-40
-60
-80
-100
-120
-140
ppm

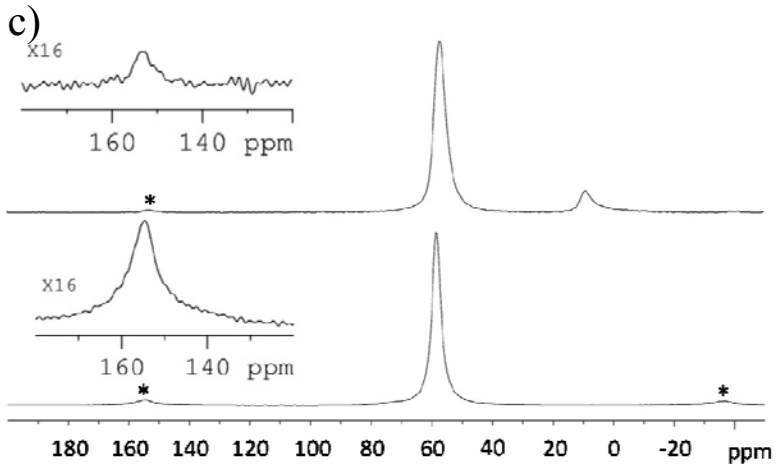

Fig. 6.5 Solid state NMR spectra of treated zeolite 4A (top) and untreated zeolite 4A (bottom): (a) ^{1}H spectra at 400.1 MHz and spinning rate of 12 kHz; (b) ^{29}Si spectra at 54.6 MHz and spinning rate of 5 kHz; (c) ^{27}Al spectra at 104.2 MHz and spinning rate of 10 kHz. The numbers denote chemical shifts relative to the peaks, and the insets are 8 and 4 times magnification of the region from 4 ppm to 0 ppm for treated and untreated samples in (a). The spinning sidebands in (c) are marked by asterisks and the insets are 16 times magnification of the corresponding regions.

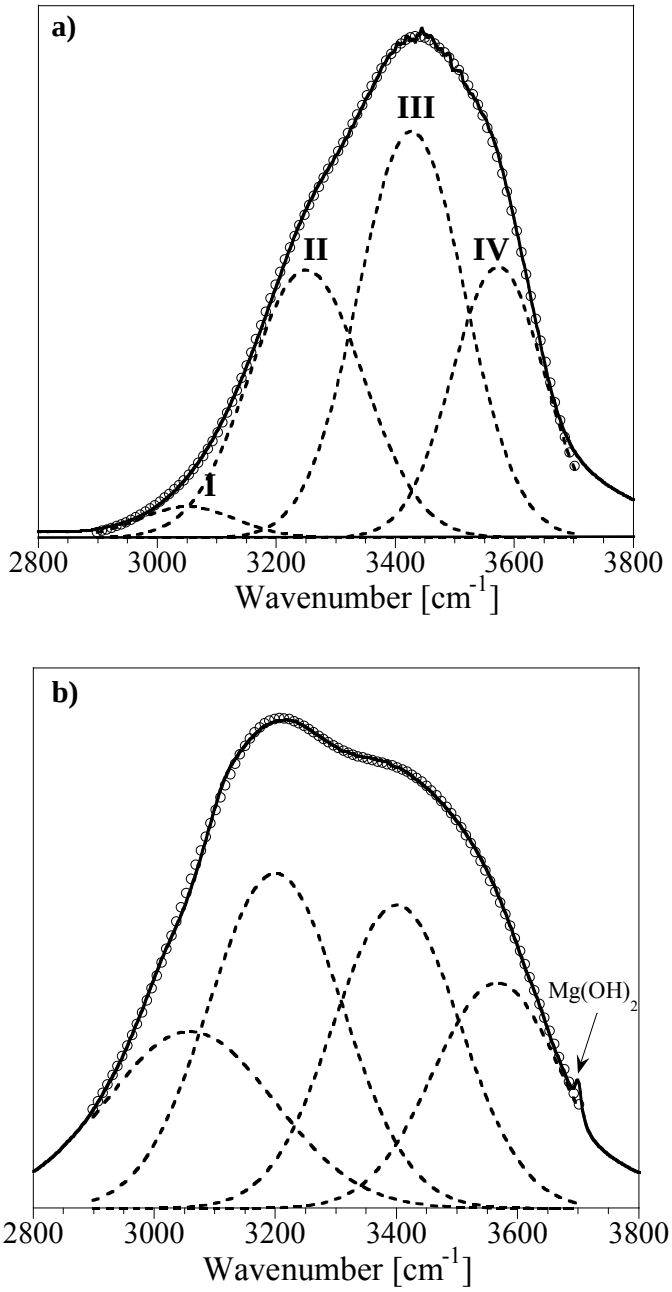

Fig. 6.6 FTIR O-H stretching spectra (continuous line) for (a) virgin zeolite 4A and (b) treated zeolite 4A, together with theoretical best fit (open circles) and the deconvolution components (dashed lines). The Gaussian deconvolution was done using Orgin 8.0. The subbands (I, II, III and IV) from low frequency to high are located at: in (a): (I) 3050.1 (percentage intensity by peak area, 2.9 %),(II) 3250.0 (30.0 %), (III) 3426.9 (42.5 %), (IV) 3572.7 (24.6 %); in (b), (I) 3059.7 (9.3 %), (II) 3200.0 (44.2 %), (III) 3417.8 (36.2 %), (IV) 3566.8 (10.2 %).

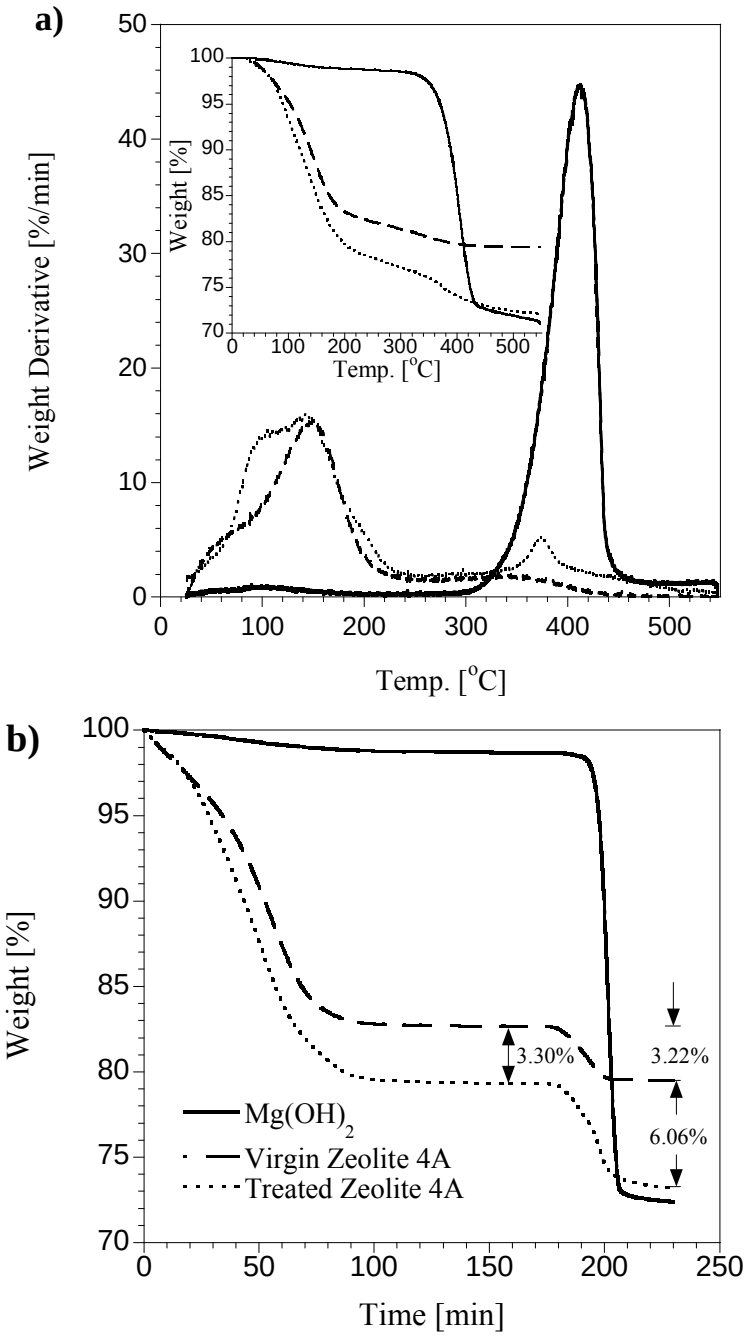

Fig. 6.7 TGA results for $Mg(OH)_2$ (solid line), virgin zeolite 4A (dashed line), and treated zeolite 4A (dotted line): (a) weight derivative and weight loss (inset) curves obtained using procedure (1); (b) weight loss curves obtained using procedure (2).

6-4 Deposition mechanism for $Mg(OH)_2$ on zeolite 4A surface

Many methods have been proposed to create nanostructures of $Mg(OH)_2$ on molecular sieves [15, 17, 30]. It has been shown that $Mg(OH)_2$ has a tendency to form hexagonal platelets when crystallized from aqueous solutions due to its layer brucite crystal structure [23, 24, 31, 32]. It has also been shown that the formation of rod-like $Mg(OH)_2$ from aqueous solutions requires the addition of a polymer dispersant template [31]. In addition, the formation of $Mg(OH)_2$ nanowhiskers on the surface of zeolite 4A requires a complicated halide / Grignard route or a solvothermal process [17]. Here, a simple, high yield, and controllable deposition – precipitation method is developed to grow $Mg(OH)_2$ nanopetals on the surface of zeolite 4A from an aqueous solution via the following reaction:

$$MgCl_2 + NH_4OH \rightarrow Mg(OH)_2 + NH_4Cl$$

Nanostructures of $Mg(OH)_2$ (Fig. 6.1c and d) were formed on the surface of zeolite 4A (Fig. 6.1a) with petals growing simultaneously on the surface of the zeolite. In this experiment, the starting pH of the aqueous suspension was ~ 11, which is lower than the isoelectric point of magnesium hydroxide in water (~ pH 12). This suggests that the $Mg(OH)_2$ is positively charged and that the ammonium cation is not easily adsorbed on the crystal facets due to its large size [24]. On the other hand, hydroxyl ions are adsorbed onto the basal plane of the crystallite and promote the edgewise growth of $Mg(OH)_2$. The presence of $Mg(OH)_2$ on the surface of the zeolite is indicated by the FTIR peak centered at 3700 cm^{-1} as shown in Fig. 6.6b.

The characteristics of $Mg(OH)_2$ / zeolite 4A nanocomposite were investigated using solid state NMR, ICP-OES, TGA, and FTIR. The peak at 0.8 ppm and the red shift in the FTIR frequency sub-bands signify that the Na^+ ions in the cavities of the zeolite 4A were partially substituted by Mg^{2+} ions during treatment. The substitution of Na^+ ions by Mg^{2+} ions was also supported by the ICP-OES analysis. The smaller Mg^{2+} ions were located on the edges of zeolite α cages, thus allowing more water molecules to access the zeolite cavities. This is also indicated by weight loss curves shown in the inset of Fig. 6.7a which shows that virgin zeolite 4A and treated zeolite 4A display different weight loss profiles at temperature above 400 °C. The DTG curve in Fig. 6.7a shows that nanopetals on the zeolite surface have a lower decomposition temperature and narrow decomposition temperature range which is indicative of uniform and nanosize $Mg(OH)_2$. Approximately 12 wt % $Mg(OH)_2$ nanopetals are formed on the surface of zeolite 4A. This value is within the range estimated from ICP-OES analysis (~2.75- 14.66 %), and further supports an ion exchange process during the precipitation of $Mg(OH)_2$.

From the proton NMR of the treated sample and virgin zeolite, the new peak at 7.3 ppm can be attributed to bridging OH groups in Brönsted acid sites (SiOHAl) perturbed by adsorbed $Mg(OH)_2$. This broad 7.3 ppm peak infers that there was an interaction between $Mg(OH)_2$ and bridging hydroxyl protons. Moreoever, ^{29}Si and ^{27}Al NMR spectra of the treated zeolite display a similar change in the chemical environment of both Si and Al sites in the presence of $Mg(OH)_2$ nanopetals. Taking these results into consideration, it can be concluded that $Mg(OH)_2$ is preferentially adsorbed onto the bridging hydroxyl protons (SiOHAl) on the zeolite 4A surface.

When magnesium chloride is dissolved in water, the Mg^{2+} ions become solvated by the surrounding water molecules according to [33-35]:

$$Mg^{2+} + 6H_2O \rightarrow [Mg(OH_2)_6]^{2+}$$

These solvated Mg^{2+} ions then undergo a hydrolysis reaction when ammonium hydroxide is added into the solution, forming a weakly basic $Mg(OH)_2$ which may react with the acidic zeolite surface hydroxyl groups.

$$[Mg(OH_2)_6]^{2+} + OH^- \rightarrow [Mg(OH)(OH_2)_5]^+ + H_2O$$

$$[Mg(OH)(OH_2)_5]^+ + OH^- \rightarrow Mg(OH)_2 + 5H_2O$$

In principle, the Brönsted acidity of the zeolite 4A surface hydroxyl groups increases in the order of AlOH < SiOH < SiOHAl, with bridging hydroxyl proton being the strongest acid [2-4, 36]. Therefore, the basic $Mg(OH)_2$ interacts with the bridging hydroxyl protons via an acid-base reaction. The acidic bridging hydroxyl group donates a proton to $Mg(OH)_2$ forming $MgOH^+$ and water molecules. The resulting $MgOH^+$ will then accept a lone pair of electrons from the deprotonated bridging hydroxyl which now acts as a Lewis base. The precipitated MgOH groups then undergo condensation with each other via oxolation, leading to the formation of a hydroxide network. In the oxolation reaction, a nucleophilic substitution takes place with Mg-OH as the nucleophile and OH^- or H_2O as leaving group. Since ammonium hydroxide is used as the precipitant, the first step of the oxolation reaction may be catalyzed by the base which enhances the nucleophilic attack [34]. In this case, the leaving group is the OH^- ions which would further propagate the growth of $Mg(OH)_2$ on the zeolite surface. The oxolation

mechanism is a slow process [34], therefore a longer synthesis time is more favorable for the growth of $Mg(OH)_2$ crystal on the zeolite surface as discussed in chapter 3.

The deposition mechanism of $Mg(OH)_2$ on the bridging hydroxyl group and the oxolation mechanism of the MgOH groups on the zeolite surface are depicted as follows:

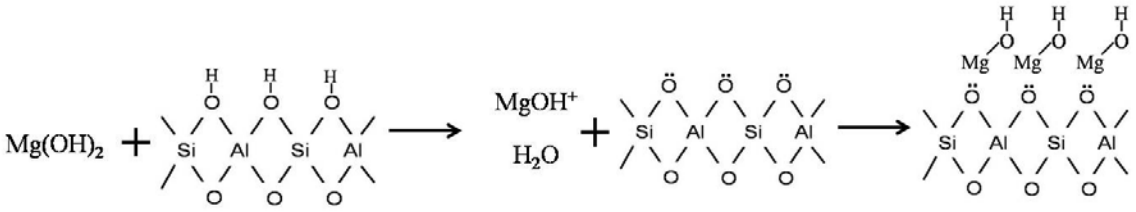

$$Mg - OH + OH^- \rightarrow Mg\text{-}O^- + H_2O$$

$$Mg - O^- + Mg - OH \rightarrow Mg\text{-}O\text{-}Mg + OH^-$$

As the acid-base reaction proceeds with time, more hydroxide ions in the solution are consumed thereby reducing the pH [37]. This decrease in the pH of the solution with time is shown in Fig. 6.8 where it can be seen that the pH of the solution decreases from ~pH 11 to ~pH 9.8 over 96 h. This proposed mechanism is supported by observations from methods (i), (ii), and (iii) at 48 h as shown in Fig. 6.4. As can be seen from Fig. 6.4a and c**,** $Mg(OH)_2$ nanopetals were deposited homogenously on the surface of the zeolite. In method (ii), zeolite 4A was dispersed into ammonium hydroxide solution prior to the addition of $MgCl_2$. This resulted in less formation and non-uniform distribution of $Mg(OH)_2$ on zeolite 4A (Fig. 6.4b) compared to the results obtained from methods (i) and (iii) (Fig. 6.4a and c). In method (ii), a majority of the bridging hydroxyl protons reacted with NH_4OH via an acid-base reaction, exposing deprotonated oxygen at the bridging hydroxyl sites. The deprotonated oxygen with a lone pair of electrons could act as a Lewis base. However, this would not favor interaction with the basic $Mg(OH)_2$ that is

formed upon titration of $MgCl_2$. Therefore, fewer $Mg(OH)_2$ nanopetals are formed on the zeolite surface. Figure 6.4a and c imply that the adsorption of $Mg(OH)_2$ on the zeolite surface is preceded by formation of $Mg(OH)_2$ in the solution via a hydrolysis reaction when $MgCl_2$ is contacted with NH_4OH. In comparison with the uniform and well-defined $Mg(OH)_2$ nanopetals created by method (i), the inhomogenous nanopetals created by method (iii) can be attributed to the rapid generation of $Mg(OH)_2$.

The use of pure aluminum oxide and silicon oxide as substrates results in no $Mg(OH)_2$ nanopetals on the surfaces. This is also confirmed by EDS spectra (Fig. 6.2). There is no Mg on the surfaces of the aluminum oxide and silicon oxide (Fig. 6.2b and c) while Mg is present on the treated surface of 4A (Fig. 6.2a). These results suggest that the deposition of $Mg(OH)_2$ originates from the Si-OH-Al group on the zeolite surface instead of silanol or alunimol groups.

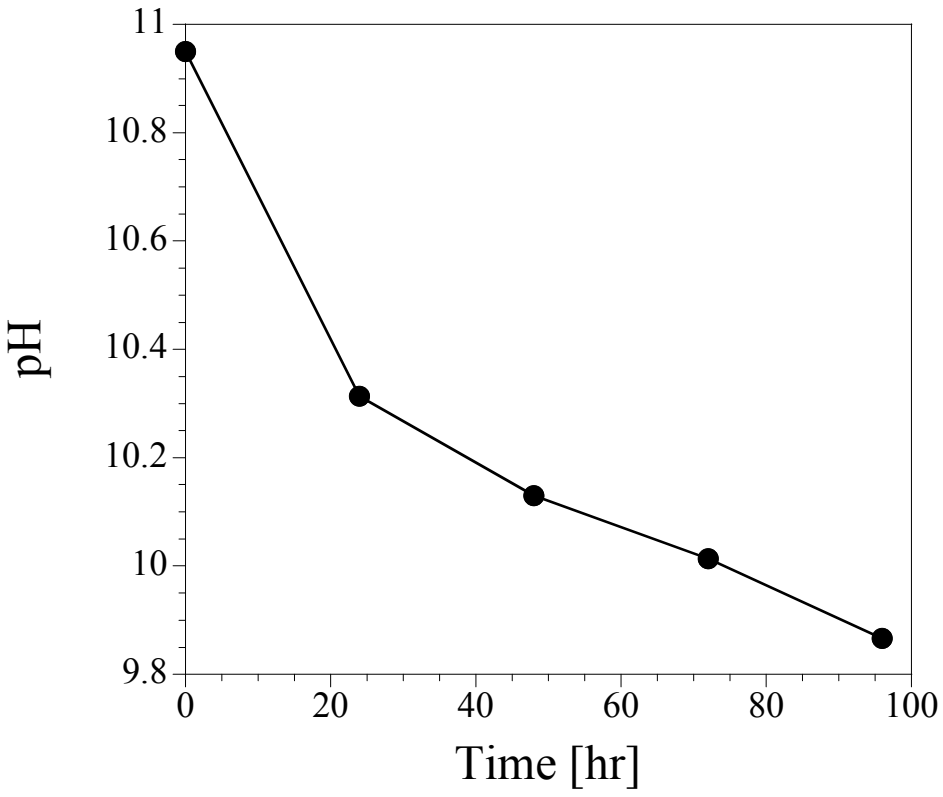

Fig. 6.8 pH of the solution as a function of time.

6-5 Conclusions

TGA and FTIR measurements revealed that the $Mg(OH)_2$ nanopetals deposited on zeolite 4A were composed of $Mg(OH)_2$ crystals and approximately 11.56 wt % of the nanocomposite consisted of $Mg(OH)_2$. It was shown that the growth of $Mg(OH)_2$ nanopetals can be controlled by manipulating the synthesis procedure. Solid-state ^{29}Si and ^{27}Al NMR spectra revealed that the precipitation-growth method caused no damage to the zeolite framework but converted parts of the tetrahedral Al into octahedral Al. The results of adsorption experiments, FTIR measurements, and solid state ^{1}H, ^{29}Si, and ^{27}Al NMR analyses indicate that $Mg(OH)_2$ adsorbed only onto bridging hydroxyl protons (SiOHAl) on the surface of zeolite 4A and not on silanol or aluminol groups. Finally, the deposition of $Mg(OH)_2$ nanostructures is thought to be the result of an acid-base interaction between $MgOH^+$ and bridging hydroxyl protons (SiOHAl).

6-6 References

1. Selim, H.M.E. and I.K. Iskandar, eds. *Fate and transport of heavy metals in the vadose zone*. 1999, Lewis Publishers: Boca Raton, Fla. 328 p.

2. Tsyganenko, A.A., E.N. Storozheva, O.V. Manoilova, T. Lesage, M. Daturi, and J.C. Lavalley, *Brønsted acidity of silica silanol groups induced by adsorption of acids.* Catalysis Letters, 2000. 70(3): p. 159-163.

3. Hunger, M., *Broensted Acid Sites in Zeolites Characterized by Multinuclear Solid-State NMR Spectroscopy.* Catalysis Reviews: Science and Engineering, 1997. 39(4): p. 345 - 393.

4. Daniell, W., U. Schubert, R. Glockler, A. Meyer, K. Noweck, and H. Knozinger, *Enhanced surface acidity in mixed alumina-silicas: a low-temperature FTIR study.* Applied Catalysis A: General, 2000. 196(2): p. 247-260.

5. Beta, I.A., B. Hunger, W. Bohlmann, and H. Jobic, *Dissociative adsorption of water in CaNaA zeolites studied by TG, DRIFTS and 1H and 27Al MAS NMR spectroscopy.* Microporous and Mesoporous Materials, 2005. 79(1-3): p. 69-78.

6. van Bokhoven, J.A., D.C. Koningsberger, P. Kunkeler, H. van Bekkum, and A.P.M. Kentgens, *Stepwise Dealumination of Zeolite Beta at Specific T-Sites Observed with ^{27}Al MAS and ^{27}Al MQ MAS NMR.* Journal of the American Chemical Society, 2000. 122(51): p. 12842-12847.

7. Eldewik, A., J.M. Hook, N.K. Singh, and R.F. Howe, *Multinuclear solid-state NMR study of cadmium- and lead-exchanged LTA zeolites.* Magnetic Resonance in Chemistry, 1999. 37: p. S63-S68.

8. Moran, K.L., P.D. Barker, J.E. Readman, P.P. Edwards, R. Dupree, and P.A. Anderson, *Si-29 and Al-27 MAS NMR spectra are affected by alkali metal cluster formation in zeolite LTA.* Chemical Communications, 2000(1): p. 55-56.

9. Vyalikh, A., F.R. Costa, U. Wagenknecht, G. Heinrich, D. Massiot, and U. Scheler, *From Layered Double Hydroxides to Layered Double Hydroxide-Based Nanocomposites-A Solid-State NMR Study.* Journal of Physical Chemistry C, 2009. 113(51): p. 21308-21313.

10. Sideris, P.J., U.G. Nielsen, Z. Gan, and C.P. Grey, *Mg/Al Ordering in Layered Double Hydroxides Revealed by Multinuclear NMR Spectroscopy.* Science, 2008. 321(5885): p. 113-117.

11. Bohlmann, W. and D. Michel, *H-1 MAS NMR studies of molecules adsorbed on activated zeolites.* Journal of Catalysis, 2001. 202(2): p. 421-426.

12. Chizallet, C., G. Costentin, H. Lauron-Pernot, M. Che, C. Bonhomme, J. Maquet, F. Delbecq, and P. Sautet, *Study of the structure of OH groups on MgO by 1D and 2D H-1 MAS NMR combined with DFT cluster calculations.* Journal of Physical Chemistry C, 2007. 111(49): p. 18279-18287.

13. Breck, D.W., W.G. Eversole, R.M. Milton, T.B. Reed, and T.L. Thomas, *Crystalline Zeolites. I. The Properties of a New Synthetic Zeolite, Type A.* Journal of the American Chemical Society, 1956. 78(23): p. 5963-5972.

14. Beck, L.W. and J.F. Haw, *Multinuclear NMR studies reveal a complex acid function for zeolite beta.* The Journal of Physical Chemistry, 2002. 99(4): p. 1076-1079.

15. Shu, S., S. Husain, and W.J. Koros, *Formation of nanostructured zeolite particle surfaces via a halide/Grignard route.* Chemistry of Materials, 2007. 19(16): p. 4000-4006.

16. Engelhardt, G., H.G. Jerschkewitz, U. Lohse, P. Sarv, A. Samoson, and E. Lippmaa, *500 MHz ^{1}H-MAS n.m.r. studies of dealuminated HZSM-5 zeolites.* Zeolites, 1987. 7(4): p. 289-292.

17. Shu, S., S. Husain, and W.J. Koros, *A general strategy for adhesion enhancement in polymeric composites by formation of nanostructured particle surfaces.* The Journal of Physical Chemistry C, 2007. 111(2): p. 652-657.

18. Crupi, V., D. Majolino, F. Longo, P. Migliardo, and V. Venuti, *FTIR/ATR study of water encapsulated in Na-A and Mg-exchanged A-zeolites.* Vibrational Spectroscopy, 2006. 42(2): p. 375-380.

19. Bourgeat-Lami, E., P. Massiani, F. Di Renzo, P. Espiau, F. Fajula, and T. Des Courieres, *Study of the state of aluminium in zeolite-b.* Applied Catalysis, 1991. 72(1): p. 139-152.

20. Omegna, A., J.A. van Bokhoven, and R. Prins, *Flexible aluminum coordination in alumino-silicates. Structure of zeolite H-USY and amorphous silica-alumina.* The Journal of Physical Chemistry B, 2003. 107(34): p. 8854-8860.

21. Wouters, B.H., T.H. Chen, and P.J. Grobet, *Reversible Tetrahedral-Octahedral Framework Aluminum Transformation in Zeolite Y.* Journal of the American Chemical Society, 1998. 120(44): p. 11419-11425.

22. Ding, Y., G. Zhang, H. Wu, B. Hai, L. Wang, and Y. Qian, *Nanoscale magnesium hydroxide and magnesium oxide powders: Control over size, shape, and structure via hydrothermal synthesis.* Chem. Mater., 2001. 13(2): p. 435-440.

23. Wang, D., C. Song, and Z. Hu, *Synthesis of mono-dispersed $Mg(OH)_2$ nanoflakelets.* Journal of Dispersion Science and Technology, 2008. 29(7): p. 1010 - 1012.

24. Henrist, C., J.P. Mathieu, C. Vogels, A. Rulmont, and R. Cloots, *Morphological study of magnesium hydroxide nanoparticles precipitated in dilute aqueous solution.* Journal of Crystal Growth, 2003. 249(1-2): p. 321-330.

25. Pourmortazavi, S.M., I. Kohsari, and S.S. Hajimirsadeghi, *Electrosynthesis and thermal characterization of basic copper carbonate nanoparticles.* Central European Journal of Chemistry, 2009. 7(1): p. 74-78.

26. Breck, D.W., *Zeolite molecular sieves: Structure, chemistry, and use.* . 1973, New York: John Wiley & Sons.

27. Crupi, V., F. Longo, D. Majolino, and V. Venuti, *T dependence of vibrational dynamics of water in ion-exchanged zeolites A: A detailed Fourier transform infrared attenuated total reflection study.* The Journal of Chemical Physics, 2005. 123(15): p. 154702.

28. Liu, H. and J.H. Yi, *Polystyrene/magnesium hydroxide nanocomposite particles prepared by surface-initiated in-situ polymerization.* Applied Surface Science, 2009. 255(11): p. 5714-5720.

29. Wu, X.F., G.S. Hu, B.B. Wang, and Y.F. Yang, *Synthesis and characterization of superfine magnesium hydroxide with monodispersity.* Journal of Crystal Growth, 2008. 310(2): p. 457-461.

30. Bae, T.H., J.Q. Liu, J.S. Lee, W.J. Koros, C.W. Jones, and S. Nair, *Facile high-yield solvothermal deposition of inorganic nanostructures on zeolite crystals for mixed matrix membrane fabrication.* Journal of the American Chemical Society, 2009. 131(41): p. 14662-14663.

31. Yan, H., J.M. Wu, X.C. Zhang, Y. Zhang, L.Q. Wei, X.G. Liu, and B.S. Xu, *Synthesis of magnesium hydroxide nanoneedles and short nanorods on polymer dispersant template.* Journal of Materials Research, 2007. 22(9): p. 2544-2549.

32. Jin, D.L., X.Y. Gu, X.J. Yu, G.S. Ding, H.L. Zhu, and K.H. Yao, *Hydrothermal synthesis and characterization of hexagonal $Mg(OH)_2$ nano-flake as a flame retardant.* Materials Chemistry and Physics, 2008. 112(3): p. 962-965.

33. Bach, S., M. Henry, N. Baffier, and J. Livage, *Sol-gel synthesis of manganese oxides.* Journal of Solid State Chemistry, 1990. 88(2): p. 325-333.

34. *Sol-gel : science and technology : proceedings of the Winter School on Glasses and Ceramics from Gels, Sao Carlos (SP), Brazil, 14-19 August 1989*, ed. M.A. Aegerter. 1989, Singapore ;: World Scientific.

35. Rayner-Canham, G., *Descriptive inorganic chemistry*. 3rd ed. / ed, ed. T. Overton. 2003, New York :: W.H. Freeman.

36. Ivanov, Y., V. Cheshkov, and M. Natova, *Polymer composite materials : interface phenomena & processes*. Solid mechanics and its applications ;, ed. V. Cheshkov and M. Natova. 2001, Dordrecht ;: Kluwer Academic Publishers.

37. Wark, M., W. Lutz, G. Schulz-Ekloff, and A. Dyer, *Quantitative monitoring of side products during high loading of zeolites by heavy metals via pH measurements.* Zeolites, 1993. 13(8): p. 658-662.

CHAPTER 7

CONCLUSIONS AND RECOMMENDATIONS

7-1 Conclusions

A facile deposition – precipitation method was developed for the deposition of magnesium hydroxide nanostructures on zeolite 4A starting an aqueous solution of magnesium chloride and ammonium hydroxide at ambient conditions. Lower temperature favors the formation of well-defined nanocomposite. The size and precipitation of $Mg(OH)_2$ nanostructures increased with increasing magnesium chloride concentration. The use of a strong base (NaOH) led to the formation of tiny $Mg(OH)_2$ particles, while synthesis driven with a weak base (NH_4OH) promoted the obtaining of petal- shaped nanostructures. Increasing the synthesis time facilitated the crystal growth of $Mg(OH)_2$ nanostructure and composition of $Mg(OH)_2$ in the $Mg(OH)_2$/ zeolite nanocomposite.

BET and TGA measurements indicate that the pores of the $Mg(OH)_2$ / zeolite nanocomposite were not plugged and the composition of the nanocomposite could be effectively controlled by varying the concentration of magnesium chloride/ ammonium hydroxide and synthesis time. The BET results suggested that the growth of $Mg(OH)_2$ occurred mainly on the external surface of zeolite 4A. It was found that the glass transition temperature, toughness, and strain-at-break properties of the Ultem® polymer films decreased with the addition of bare zeolites, but less with $Mg(OH)_2$ / zeolite 4A nanocomposites. This is in agreement with observation by Shu et al. [1] that the $Mg(OH)_2$ nanostructures was can result in enhanced adhesion between the zeolite and polymer matrix.

Adsorption isotherms were measured for the deposition of $Mg(OH)_2$ on zeolite 4A (magnesium hydroxide – zeolite system). It was demonstrated that 3 adsorption mechanisms (ion exchange, surface adsorption of Mg^{2+} ions, and surface precipitation of $Mg(OH)_2$) are involved in the deposition of $Mg(OH)_2$. Analysis of the magnesium hydroxide – zeolite system adsorption isotherms indicated four distinct regions of adsorption involving different adsorption mechanisms. Adsorption isotherms were also measured using virgin zeolite 4A and ion-exchanged zeolite 4A in magnesium chloride solution and it was determined that the predominant processes in the absence of ammonium hydroxide are ion exchange and surface adsorption of Mg^{2+} ions. Therefore, ammonium hydroxide plays a significant role in controlling the pH of the slurries and in inducing nucleation and precipitation of $Mg(OH)_2$ on zeolite surfaces.

The interactions between $Mg(OH)_2$ and zeolite 4A were characterized and determined mainly by solid state MAS NMR. Solid-state ^{29}Si and ^{27}Al NMR spectra revealed that the deposition - precipitation method caused no damage to the zeolite framework but converted parts of the tetrahedral Al into octahedral Al. The results of adsorption experiments conducted on silica and alumina, FTIR measurements, and solid state ^{1}H, ^{29}Si, and ^{27}Al NMR analyses indicate that $Mg(OH)_2$ adsorbed only onto bridging hydroxyl protons (SiOHAl) on the surface of zeolite 4A and not on silanol or aluminol groups. Finally, the deposition of $Mg(OH)_2$ nanostructures is thought to be the result of an acid-base interaction between $MgOH^+$ and bridging hydroxyl protons (SiOHAl). A mechanism of $Mg(OH)_2$ deposition on the bridging hydroxyl proton of zeolite 4A was postulated based on the studies above.

7-2 Recommendations

7-2-1 Applicability of the deposition – precipitation method for other basic metal oxides

The efficacy of the fabrication procedure was not investigated for other basic metal oxides. A considerable number of metal oxides and zeolites combinations are possible for a variety of applications. Transition metal oxides, such as Co, Ni, Ag, Cu, Fe, and Zn have shown potential properties in a variety of applications such as electrochemical capacitor [2], catalysts [3-5], antibacterial agents [6], Li ion batteries [7], resonators and piezoelectric sensors [8, 9]. The hydroxides of these transition metals have very low solubility and can be easily precipitated under mild conditions. Moreover, these metal hydroxides can also be easily converted to corresponding oxides at relatively low calcinations temperature. Therefore, it may be of considerable value to investigate the relationship between the basicity of the metal oxides and acidity of the zeolites and establish guidelines for the deposition of basic metal oxides on zeolite surfaces.

7-2-2 Effects of the local environment on the formation of metal oxide nanostructures on zeolite surfaces

Metal oxides supported on zeolites have attracted considerable attention in a variety of industrial applications. The performance of these nanocomposites is dependent on the positioning, coordination, size and morphology of the metal oxides as well as the structure of zeolites. Therefore, further efforts should be pursued in understanding how the local environment on zeolite surfaces such as surface charges, localized concentration

gradients, and density of surface functional groups affect the positioning, binding, and crystallization of metal oxides in zeolites.

7-2-3 In-depth characterization of $Mg(OH)_2$ / zeolite composite

In this study, the $Mg(OH)_2$ / zeolite composites were extensively characterized using microscopy and spectroscopy techniques. Further analysis by X-ray photoelectron spectroscopy (XPS) and extended X-ray absorption fine structure (EXAFS) may provide a more comprehensive understanding of the surface chemistry of the composite. XPS may be used to determine the elemental composition and electronic state of each element in the surface, further verifying the interaction between $Mg(OH)_2$ and zeolite surface. EXAFS would provide more information about the distances between central and neighboring atoms, the number of neighboring atoms, the nature of neighboring atoms, and changes in central-atom coordination, thereby providing more information on the interaction between $Mg(OH)_2$ and zeolite and structural changes of the zeolite.

7-2-4 Prevention of $Mg(OH)_2$ / zeolite composite agglomeration

Agglomeration of bare zeolite and zeolite / $Mg(OH)_2$ composites was often encountered when the nanocomposites were dispersed in polymer membranes. Therefore, a better method should be developed to disperse the zeolite particles more efficiently in the polymer. Agglomeration may be reduced by treating the zeolite particles with phosphonic acid. It has been shown that aggregation of barium titanate nanoparticles was reduced when the surface of these particles was modified by phosphonic acid [10].

7-2-5 In-depth investigation of the effects of magnesium hydroxide surface area on the permeability and selectivity of polymer composite

It has been shown that the glass transition temperature of the Ultem® polymer composite decreased with the introduction of bare zeolite and increased as the surface of zeolite was modified with magnesium hydroxide. Experiments have been carried out to test the efficacy of the Ultem® polymer composite in gas separation [11, 12]. Further efforts should be done to systematically examine how the polymer mobility is affected by the magnesium hydroxide total surface area, which in turn may influence the permeability or selectivity of the polymer composite. This can be done by dispersing a fixed amount of zeolite deposited with different amounts of magnesium hydroxide into Ultem® polymer and test the permeability and selectivity of the resulting Ultem® polymer composite.

7-3 References

1. Shu, S., *Engineering the performance of mixed matrix membranes for gas separations*. 2007, Georgia Institute of Technology: United States -- Georgia. p. 251.

2. Cao, L., F. Xu, Y.Y. Liang, and H.L. Li, *Preparation of the novel nanocomposite $Co(OH)_2$/ ultra-stable Y zeolite and its application as a supercapacitor with high energy density.* Advanced Materials, 2004. **16**(20): p. 1853-+.

3. Kinger, G., A. Lugstein, R. Swagera, M. Ebel, A. Jentys, and H. Vinek, *Comparison of impregnation, liquid- and solid-state ion exchange procedures for the incorporation of nickel in HMFI, HMOR and HBEA: Activity and selectivity in n-nonane hydroconversion.* Microporous and Mesoporous Materials, 2000. **39**(1-2): p. 307-317.

4. Gurbani, A., J.L. Ayastuy, M.P. Gonzalez-Marcos, J.E. Herrero, J.M. Guil, and M.A. Gutierrrez-Ortiz, *Comparative study of CuO-CeO_2 catalysts prepared by wet impregnation and deposition-precipitation.* International Journal of Hydrogen Energy, 2009. **34**(1): p. 547-553.

5. Ismagilov, Z.R., S.A. Yashnik, V.F. Anufrienko, T.V. Larina, N.T. Vasenin, N.N. Bulgakov, S.V. Vosel, and L.T. Tsykoza, *Linear nanoscale clusters of CuO in Cu-ZSM-5 catalysts.* Applied Surface Science, 2004. **226**(1-3): p. 88-93.

6. Dai, J.M., W.S. Hou, L.Q. Wei, H.S. Jia, X.G. Liu, and B.S. Xu, *Study on the color change resistant property of silver and zinc-loading zeolite 4A antibacterial agent.* Journal of Inorganic Materials, 2008. **23**(5): p. 1011-1015.

7. Manthiram, A. and J. Kim, *Low temperature synthesis of insertion oxides for lithium batteries.* Chemistry of Materials, 1998. **10**(10): p. 2895-2909.

8. Gao, P.X. and Z.L. Wang, *Nanoarchitectures of semiconducting and piezoelectric zinc oxide.* Journal of Applied Physics, 2005. **97**(4).

9. Gao, P.X., Y. Ding, W.J. Mai, W.L. Hughes, C.S. Lao, and Z.L. Wang, *Conversion of zinc oxide nanobelts into superlattice-structured nanohelices.* Science, 2005. **309**(5741): p. 1700-1704.

10. Kim, P., S. Jones, P. Hotchkiss, J. Haddock, B. Kippelen, S. Marder, and J. Perry, *Phosphonic acid-modified barium titanate polymer nanocomposites with high permittivity and dielectric strength.* Advanced Materials, 2007. **19**(7): p. 1001-1005.

11. Bae, T.H., J.Q. Liu, J.S. Lee, W.J. Koros, C.W. Jones, and S. Nair, *Facile high-yield solvothermal deposition of inorganic nanostructures on zeolite crystals for mixed matrix membrane fabrication.* Journal of the American Chemical Society, 2009. **131**(41): p. 14662-14663.

12. Shu, S., S. Husain, and W.J. Koros, *A general strategy for adhesion enhancement in polymeric composites by formation of nanostructured particle surfaces.* The Journal of Physical Chemistry C, 2007. **111**(2): p. 652-657.